On Mixed Wind-Sea/Swell Conditions in the Open Ocean

-

Model and Radar-Observations

Hovedfagsoppgave i fysisk oseanografi

Ole Johan Aarnes
Bergen 2005

Geofysisk Institutt
Universitetet i Bergen

Acknowledgement

I would like to direct my thanks to Knut Barthel, my supervisor for this thesis, for always being accessible and taking time for discussion. His knowledge and easy being has made the process pleasant throughout the whole period.

My exterior supervisor has been Anne Karin Magnusson from the Meteorological Institute of Bergen. Thanks to Anne Karin I got the chance to study waves, which have been a big interest of mine for quite some time. Thanks for giving me the opportunity to work at the Meteorological Institute and participate at the 2004 WISE-meeting. Hopefully our collaboration does not end with this work.

At last, I would like to thank all my fellow students at the Geophysical Institute of Bergen, especially the people at ODD, for making this work so much more enjoyable. And, by the way, we need a new coffee maker.

Ole Johan Aarnes
Bergen - April 2005

Contents

Chapter 1

Introduction

Wind generated surface waves are without a doubt the most striking phenomenon found at the ocean surface. They play a significant part both in modern society and climate variability, affecting the likes of offshore and shipping industry, and more importantly the heat and gas exchange at the air-sea interface. Ongoing scientific work continue to better our understanding of ocean wave physics, which are put to use in numerical models. But as our level of knowledge improves, a higher demand for reliable measuring tools and optimized numerical models are required if further progress are to be expected in the future.

In this thesis focus will be made on all three sides of the aspect, wave physics, observation/measurement and modelling. The measurements have been obtained by a remote sensing wave radar developed and manufactured by MIROS A/S, while corresponding model data are deduced using a third generation wave model, WAM, run operationally at the Meteorological Institute of Bergen, Norway(met.no). Both methods produce comparable 2D directional frequency spectra. Since neither of the two are flawless in operation, but have different advantages, they may be used to address shortcomings in the other. In addition, the two different approaches may be used in hypothesis testing. While mechanisms not jet fully understood are unaccounted for in the WAM-model, they may affect the measurements and in that way support/reject developing theories.

The terminology used to describe wind generated surface waves often separate the phenomenon wind-sea and swell. When wind blows across the ocean surface waves are generated through friction between the atmosphere and ocean. As long as the velocity of the wind is higher than the phase velocity of the waves, friction is maintained, causing waves to grow. A growing wave system is what we refer to as a wind-sea. However, if the wind subside, change direction or the waves evolve to the point of having the same velocity as the wind, these waves are no longer subjected to energy transference from the atmosphere. Such freely propagating wave systems are known as swells. In the open ocean wave conditions are most often influenced by swell activity. The small effect of dissipation allows swells to propagate over thousands of kilometers, giving rise to combined swell and wind-sea systems. Pure wind-seas are more commonly experienced at coast-near locations.

The analysis of this thesis is based on two severe wave events from February 2000 and December 2003 taking place in the North Sea and Norwegian Sea. Both time series are dominated by combined swell/wind-sea conditions, which may have certain implications in wave radar observations and wave modelling. Some of the problems encountered will be presented and discussed in the following. In addition, a general comparison of the WAM-model and MIROS radar is carried through.

The classical works of Miles (1957) and Phillips (1957) set the framework for our knowledge on generation of wind waves. Since then several improvements have been made in the struggle to find an optimized parametrization of the momentum transference at the air-sea boundary. The problem comes down to finding those mechanisms affecting the stress, τ, between the atmosphere and the ocean, represented by

$$\tau = \rho u_*^2 = -\rho_a < \mathbf{u}' w' > \tag{1.1}$$

where ρ_a is the air density and $\mathbf{u}'$ and w' are the horizontal and vertical turbulent velocity fluctuations respectively. u_* is known as the friction velocity. The time averaging in eq. 1.1 is typically 20 min. Often the drag coefficient, C_D, is used to relate the wind speed to the surface stress, which is expressed by

$$\tau = \rho C_D u^2(z) \tag{1.2}$$

A lot of effort have been laid down to find an universal relation expressing the drag coefficient, using readily measurable quantities such as wind speed and atmospheric stability. However, the large amount of scatter found in the experimental data indicate that other mechanisms need to be taken into consideration.

Several studies have shown the drag coefficient to be dependant on the wave age (e.g. Donelan et al. (1993); Smith (1980)), which is expressed by c_p/u_*, where c_p is the phase speed of the wave components carrying the most amount of energy. The wave age represents a wind-sea's degree of development. Whereas a young sea is defined as wave ages < 10, an old sea is defined by wave ages > 25. These field studies have shown that the drag coefficient is increasing for younger waves. The WAM-model uses a wave age dependent wave growth which have given high quality results. However, in the open ocean most wave systems are close to full development, making it hard to discern wave age effects (Drennan et al. 1999).

Focus has been directed towards how the interaction of swell may alter the drag coefficient. Kudryavtsev and Makin (2004) presented in their work a model which proposed a significant increase of the drag coefficient in conditions of swell opposing weak winds, compared to situations without swell. This effect was also debated in the works of Donelan et al. (1997) and Drennan et al. (1999), which made similar findings. Dobsen et al. (1994) made comparisons of the drag coefficient obtained in pure wind-seas and in the presence of swell, but did not find the same effects. Now, if counter-swells are stimulating a larger drag coefficient, this would further increase the growth rate of wind-seas. This effect is not accounted for in the WAM-model. Thereby, comparing the WAM-model with corresponding observations should give a less evolved simulated wind-sea in the presence of opposing swell.

The oblique looking MIROS-radar is a remote sensing device measuring the directional frequency spectrum with a 30 degree directional resolution and 0.0078Hz resolution in frequency. The physical shape of the radar is constructed to scan 180 degrees of open ocean. Highly developed signal analysis enables the radar to measure both approaching and receding waves. However, the signal analysis is based on the condition that only one out of two directional-frequency bins of 180 degrees ambiguity can be represented (Grønlie 1999). How much is the quality of the 2D spectrum reduced in situations where two colliding wave systems are present? And in this context, is the MIROS-radar sensitive to its heading?

In operational application the model is forced by both analyzed and prognostic 10m wind fields obtained by an independent atmospheric model. Since the analyzed wind fields are a combination of first-guess data and observations, the wave model is expected to perform better when forced by these winds compared to prognostic winds. However, often the 12-24 hour wave-forecasts are of just as high quality, or even better, as when forced by analyzed winds (Komen et al. 1996). This statement will be tested comparing the most commonly used wave parameters, significant wave height, H_s, and the peak period, T_p.

Several institutions around the world are currently running the WAM-model operationally. Since the model simulations require large amounts of computer power, most users restrict the modelling to geographical limited areas. As the model allows for some degrees of freedom, the boundary conditions can be chosen by the user, but are often set to zero. This means all energy generated outside the boundaries are lost, which may give significant misrepresentations when powerful distant swells produced outside the boundaries propagate into the modelled area.

The program of this paper is therefore as follows. Chapter 2 will give an introduction to fundamental wave theory followed by a presentation of the MIROS-radar and the WAM-model. Chapter 5 takes a closer look at the drag coefficient at the air-sea interface. Chapter 6 gives a presentation of the data and methods used in the analysis of chapter 7. And finally, chapter 8 offers final conclusions and future thoughts.

Chapter 2

Fundamental wave-theory

2.1 Assumptions on sea water and wave motion

In all its simplicity ocean surface waves may be summarized as the interplay of three different forces. First of all, there must exist some kind of *generating force*, e.g. wind, capable of perturbing the surface. Once the surface no longer is flat, a *restoring force* striving to bring back the surface to its equilibrium state is needed. In case of wind generated waves, this is the sum of gravity/buoyancy and the surface tension between water particles, their individual importance depending on the spatial scale of motion, i.e. the wavelength. Finally, the *inertia* of the system makes the surface overshoot its equilibrium state. The interplay between the restoring force and inertia maintains the oscillating motion characterizing a wave. With no other exterior forces acting on a wave, this oscillating motion would go on infinitely. However, as there are several additional factors affecting ocean surface waves, this is not the case.

In order to give an exact mathematical description of the phenomenon, some physical and chemical assumptions concerning sea water are often being made (WMO 1998):

- water is an incompressible fluid

$$\frac{1}{\rho_w}\frac{d\rho_w}{dt} = 0 \tag{2.1}$$

- water is an inviscid fluid

$$\mu_w = 0 \tag{2.2}$$

- motion is irrotational

$$\nabla \times \mathbf{u} = 0 \tag{2.3}$$

, where ρ_w is the water density, μ_w is the water viscosity and $\mathbf{u}$ is water particle velocity in the horizontal.

2.2 Wave definitions and basic relations

A wave is best described using a few simple parameters illustrated in fig. 2.1:

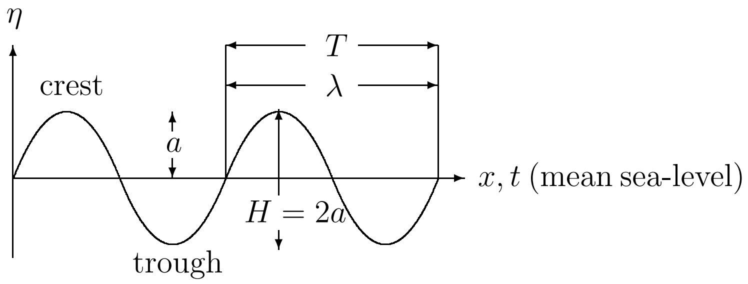

Figure 2.1: *Basic parameters used to describe a wave.*

- The wave *crest* is the highest part of the wave above mean sea-level
- The wave *trough* is the lowest part under mean sea-level
- The *wavelength*, λ[m], is the horizontal distance between two successive crests, or troughs
- The wave *period*, T[s], is the time interval between the passage of two successive crests at a fixed point
- The *frequency*, f[Hz], is the number of crests passing a fixed point per second
- The wave *amplitude*, a[m], is the maximum displacement from the mean sea-level
- The wave *height*, H[m], is the difference in vertical displacement between a crest and the adjacent trough
- The *phase speed*, c[m/s], or rate of propagation, is the speed the crest advances in space
- The *steepness* is given by the ratio of wave height to wavelength H/λ

The most basic mathematical representation of an ocean wave is given by the sine-curve, illustrated in fig. 2.1:

$$\eta(x,t) = a\sin(kx - \omega t) \tag{2.4}$$

, where $k = 2\pi/\lambda$ is the *wave number* and $\omega = 2\pi/T$ the *angular frequency.* A sinusoid is a periodic progressive wave, with equal shape above and below the mean sea-level. However, this shape is never observed at the ocean surface, where the crests are shorter and sharper, and the troughs longer and more shallow. Still, the equation gives a fair representation in ocean wave physics. Notice that eq. 2.4 contains both a temporal and a spacial coordinate able to describe the surface displacement at a fixed position, $x = const$, varying in time and at a certain time, $t = const$, varying in space. Like all truly periodic waves, eq. 2.4 yield the relation:

$$\lambda = cT = c/f \tag{2.5}$$

The ocean surface consists of a range of wave components, each having its own characteristics. The functional variation of angular frequency/phase speed with the wave number is expressed by the important *dispersion relation*

$$\omega^2 = gk \tanh kh \tag{2.6}$$

$$\Downarrow$$

$$c = \sqrt{\frac{g}{k} \tanh kh} \tag{2.7}$$

, where g is the gravity and h the water depth. This relation is deduced from the equation of motion assuming linearity and eq. 2.1-2.3.

Fig. 2.2 illustrates how the phase speed vary with wavelength, eq. 2.7. In this context, the term *deep* and *shallow* water are meant as relative measures depending on the ratio wavelength to depth. One often characterizes deep water as the depth where $h > \lambda/4$ and shallow water where the depth is $h < \lambda/25$, in between is the so called transitional depth. Based on fig. 2.2, the phase speed, eq. 2.7, reduces to

$$c = \sqrt{\frac{g}{k}} = \sqrt{\frac{g\lambda}{2\pi}} \tag{2.8}$$

in deep water and

$$c = \sqrt{gh} \tag{2.9}$$

in shallow water. This implies that all wavelengths fulfilling $h < \lambda/25$ propagate with a constant speed only varying with depth. Waves in this range are *non-dispersive* as they are not a functions of k (WMO 1998).

2.3 Orbital motion

When studying the movement of a floating object exposed to wave motion, it is apparent that only the energy follows the wave, not the water particles. A buoy will move up and down and back and fourth in an orbital motion in the direction of the wave. In deep water the water particles have almost the same displacement in the horizontal as in the vertical plane, making close to perfect circles. However, when waves

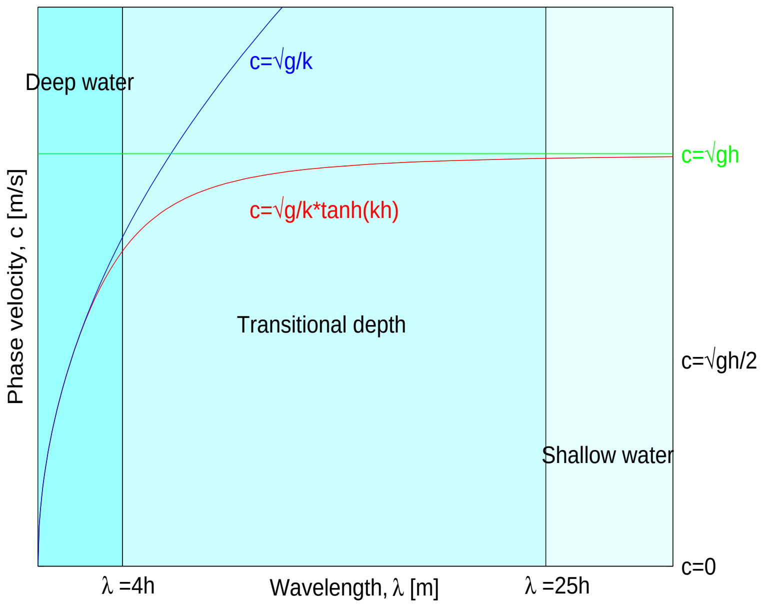

Figure 2.2: *The phase speed of gravity waves according to the dispersion relation for increasing wavelengths, λ, given at a constant depth. Deep water, transitional depth and shallow water are defined by the wavelength-depth-ratio.*

move into shallow water the motion becomes elliptic. In both cases the orbits decrease exponentially with depth, only affecting the top layer of the water column.

The orbital path of a water particle covers a circumference of πH during one period, which equals a velocity of $\pi H/T$. This corresponds to the maximum velocity in the vertical as well as the horizontal plane. Compared to the phase speed, see eq. 2.5, the particle velocity is small as λ in deep water most often is substantial in comparison to πH.

As mentioned above, the orbital motion reduces with depth, meaning the particles move slower in the horizontal plan with depth. This creates a slight forward movement going in the direction of the wave, known as the *Stokes drift*. The steeper the waves the stronger the wave-induced current. This is observed at its most extreme in the surf zone where the Stokes drift exceeds the phase speed, causing the wave to break.

2.4 Superposition, Wave groups and Group velocity

The ocean surface is never represented by only one wave component with the same wavelength, amplitude and direction. Its chaotic pattern is the sum of numerous components. A simplified example is illustrated in fig. 2.3, where two separate wave components with the same amplitude and direction, but different wavelengths interact and change the profile of the surface. Some places the waves are in phase and add up, other places they are out of face and cancel each other out. This is known as the *superposition principal*. Enough components interacting will create that irregular pattern we so often observe at the ocean surface.

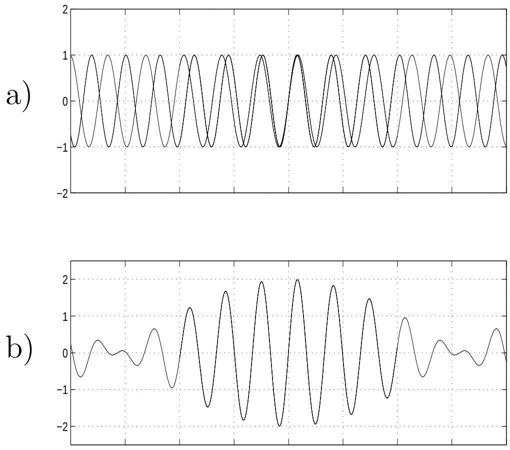

Figure 2.3: *The superposition-principal: a)Two separate wave components with the same amplitude, but different wavelengths. b)The sum of the two interacting components.*

At times the ocean surface may appear somewhat orderly, much like a sinusoid. This is most pronounced in pure swell conditions, as these types of wave systems are characterized by a smoother 'look'. When a swell is allowed to propagate undisturbed over a vast distance of open ocean the different wave components disperse according to eq. 2.7.

In that way the longer wave components will separate from the shorter ones. Even though the number of components at a fixed point may be reduced, the wave system still consists of a range of components. Because waves tend to group together, illustrated in fig. 2.3b), the surface appears more smooth. Despite each wave component propagating at its own phase speed, the group as a coherent unit moves at the same speed, the *group velocity*, expressed by

$$c_g = \frac{d\omega}{dk} = \frac{c}{2}(1 + \frac{2kh}{\sinh 2kh}) \tag{2.10}$$

In deep water, $h \gg k$, this reduces to

$$c_g = \frac{c}{2} \tag{2.11}$$

and it can be shown that $c_g = c$ in shallow water,$h \ll k$. Eq. 2.11 will become more evident in the next section.

2.5 Energy in waves

As a bearer of energy, ocean surface waves separate between kinetic energy, related to the particle motion, and potential energy, related to the displacement of the surface. The total wave energy is equally divided between the two, which will be proven in the following.

From general physics we know the potential energy as $E_p = mgh_c$, m being mass, g the gravity and h_c the displacement of the center of gravity. Now, considering a wave where the mass of an unit water column above mean sea-level is $m = \rho_w \eta$ and the center of gravity is $h_c = \eta/2$, the potential energy of one wave length equals

$$E_p = \int_0^\lambda \frac{\rho_w g}{2} \eta^2 dx \tag{2.12}$$

and the average potential energy per unit horizontal area $[Jm^{-2}]$ is given by

$$\overline{E_p} = \frac{\rho_w g}{2\lambda} \int_0^\lambda \eta^2 dx \tag{2.13}$$

When the surface displacement is represented by the sinusoid, eq. 2.4, we obtain

$$\overline{E_p} = \frac{\rho_w g a^2}{4} \tag{2.14}$$

Similarly, we often find the kinetic energy equation expressed by

$$E_k = \frac{1}{2} m v^2 \tag{2.15}$$

where v is the velocity of the moving mass, m. To derive the total kinetic energy of a wave, an integration over the whole water column is necessary. In 2 dimensions this yields

$$\overline{E_k} = \frac{1}{2} \rho_w \int_{-d}^{\eta} (\overline{u^2} + \overline{w^2}) dz \tag{2.16}$$

, where the over-bar represents an average of the velocity component in the x and z direction. Using the fact that the particle motion is represented by

$$\mathbf{v} \sim \eta e^{kz} \tag{2.17}$$

in deep water, for a varying depth z, eq. 2.16 reduces to eq. 2.14, proving that there are equal amounts of kinetic and potential energy in a propagating wave. All in all the total amount of energy in a wave per unit water column is given by;

$$E_{tot} = \overline{E_p} + \overline{E_k} = \frac{\rho_w g a^2}{2} \tag{2.18}$$

When expressed by the wave height this may be written

$$E_{tot} = \frac{1}{8} \rho_w g H^2 \tag{2.19}$$

Based on the discussion above, it is clear that the total amount of energy can not follow the phase velocity of a wave, as only half the energy is related to this velocity. As stated in eq. 2.11 the energy travels with half the phase velocity which makes sense considering the substantial difference in phase and orbital velocity. Half the energy propagates with the phase velocity and the other half practically stands still. Combined, the energy travels with half the phase velocity.

2.6 The wave spectrum

Theoretically it should be feasible to calculate the total amount of wave energy contained by the ocean surface based on the knowledge of eq. 2.18. However, as the sea surface is the sum of numerous wave components, the problem becomes how to separate each wave component from the other in a system controlled by stochastic processes. And, separating the components would only be an approximation as the ocean surface is represented by a continuum of wave components and not discrete values. Still, in everyday practice we operate with discrete components to simplify the calculations. Therefore, the wave condition is described as a statistical quantity.

A wave record of the surface elevation can by means of harmonic or Fourier analysis be decomposed into a number of sinusoids, each component having its own frequency, amplitude and phase

$$\eta(t) = \eta_0 + \sum_{j=1}^{N} a_j \sin(j\omega_0 t + \phi_j) \tag{2.20}$$

The higher the frequency, the more insignificant the energy contained by the wave component becomes, meaning there is a reasonable limit to n. It should be acknowledged that each spectral component j of eq. 2.20 represents a frequency interval and not only the frequency itself. Depending on the resolution, a spectral component with frequency 0.1Hz may e.g. represent the frequency interval 0.095-0.105Hz.

$\eta(t)$	surface elevation at time t
η_0	mean surface level
j	number of wave component
ω_0	angular frequency of the longest wave component fitted to the record
N	total number of components
ϕ_j	phase angel of the jth component
a_j	amplitude of the jth component;

Table 2.1: *Notation used in eq. 2.20*

Once a time series has been decomposed into a range of sinusoids, eq. 2.20, the squared amplitudes of each spectral(wave) component may be plotted against its frequency to obtain the *variance spectrum*, $S(f)$. However, more often the *variance density spectrum*, $E(f)$, is being used, which represents the squared amplitude of the spectral component divided by the width of the frequency interval it represents. Synonymously, the variance density spectrum is known as the *energy density spectrum*, even though the energy density is given by the variance density times $\rho_w g$. A common notion is simply *the wave spectrum*. To add to confusion, the wave spectrum often apply to both the squared amplitude, a^2, and half its value, $a^2/2$. In the following the latter will be preferred.

The wave spectrum is obtained using different measuring techniques or numerical models. Depending on the apparatus or model, the spectrum is either given in one dimension(1D), *the frequency spectrum*, or in two dimensions(2D), *the directional frequency spectrum*. The frequency spectrum represents the total sea state, while the directional frequency spectrum represents one spectrum per directional sector.

2.6.1 Moments and parameters

The wave spectrum is a statistical distribution, meaning a lot of wave parameters can be deduced in the same way as any other statistical parameter. Most used quantity is different orders, n, of moments, expressed by;

$$m_n = \int_0^\infty f^n E(f) df \tag{2.21}$$

where $E(f)$ denotes the variance density per frequency, f. As noted above, in practice $E(f)$ is never expressed as a continuum, but rather as discrete values. When eq. 2.21 is adjusted to finite form it can be written;

$$m_n = \sum_{j=0}^{N} f_j^n \frac{a_j^2}{2} \tag{2.22}$$

From eq. 2.22 the moment of zeroth order, m_0, can be found. This represents the total variance obtained by the sum of the variances of each individual spectral component;

$$m_0 = \sigma_\eta^2 = \sum_{j=0}^{N} \frac{a_j^2}{2} \tag{2.23}$$

Now, if we consider m_0 to represent only one sinusoidal wave, $m_0 = a^2/2$, it can be shown that the total wave energy at the ocean surface is given by $E_{tot} = \rho_w g m_0$ deduced from eq. 2.18.

By rewriting eq. 2.19 we obtain;

$$H_{rms} = \sqrt{\frac{8E_{tot}}{\rho_w g}} = \sqrt{8m_0} \tag{2.24}$$

In common practice the significant wave height, H_s, is a more preferable parameter than the root-mean-square wave height. Empirical studies have found a $\sqrt{2}$-relation between these two parameters, yielding the very important expression

$$H_{m_0} = 4\sqrt{m_0} \tag{2.25}$$

In other words, by taking the square-root of the area under the variance density curve multiplied by 4, the significant wave height is deduced, which corresponds to the average height of $\frac{1}{3}$rd of the highest waves estimated traditionally by means of visual observation.

Finding parameters representing different wave periods are a more complicated matter. The ocean surface is often represented by different systems, combinations of swell and wind sea, giving rise to bimodal and multi-modal wave spectra. In everyday practice the peak period, T_p, is the most commonly used parameter. It represents the period or wave component carrying the most amount of energy. f_p, is the corresponding peak frequency, related by $T_p = f_p^{-1}$. In addition, the mean period, $T_{m_{01}}$, and mean down-crossing period, $T_{m_{02}}$, is commonly used, given by

$$T_{m_{01}} = \frac{m_0}{m_1} \qquad\qquad T_{m_{02}} = \sqrt{\frac{m_0}{m_2}} \tag{2.26}$$

2.6.2 Models

In general, a wave spectrum representing a wind-sea has certain coarse features that stay more or less the same. This self-similar characteristic of ocean waves has given rise to different spectrum models, with the purpose of representing the wave spectrum just by knowing a few readily measurable quantities. Historically two models have been of significant importance, the Pierson-Moskowitz-spectrum(PM) (Pierson and Moskowitz 1964) and the Jonswap-spectrum (Hasselmann et al. 1973).

Pierson and Moskowitz (1964) defined a model spectrum for a fully developed wind-sea based on observations and theoretical studies. They considered a constant wind blowing over the surface without being fetch or duration limited, letting the spectrum reach its equilibrium state, that is, where wind input equals dissipation. The variance density spectrum is expressed by

$$E(\omega) = \alpha g^2 \omega^{-5} exp\left[-0.74\left(\frac{g}{\omega U_{19.5}}\right)^4\right] \tag{2.27}$$

where $\alpha = 0.0081$ is a dimensionless parameter and $U_{19.5}$ is the wind speed at 19.5m and the only required unknown. The experimental spectrum developed by Pierson and Moskowitz (1964) yield the relation

$$\frac{U\omega_p}{g} = const = 0.879 \tag{2.28}$$

which leads to a 'simplified' version of eq. 2.27;

$$E(\omega) = \alpha g^2 \omega^{-5} exp\left[-\frac{5}{4}\left(\frac{\omega}{\omega_p}\right)^{-4}\right] \tag{2.29}$$

The PM-spectrum has one obvious shortcoming; it does not model the wave condition in situations where fetch or duration are limiting factors, which often is the case. Observations made by Hasselmann et al. (1973) during the Joint North Sea Wave Project led to the JONSWAP-spectrum. The model immediately got recognized and has been used intensively in ocean surface wave literature.

The JONSWAP-spectrum is an extended version of the PM-spectrum given by

$$E(\omega) = \alpha g^2 \omega^{-5} exp\left[-\frac{5}{4}\left(\frac{\omega}{\omega_p}\right)^{-4}\right]\gamma^{\delta}, \tag{2.30}$$

$$\delta = exp\left[-\frac{(\omega - \omega_{p)}^2}{2\sigma_0^2\omega_p^2}\right] \tag{2.31}$$

where $\sigma_0 = \sigma_0^{'}$ for $\omega < \omega_p$ and $\sigma_0 = \sigma_0^{"}$ for $\omega > \omega_p$. γ is known as the peak enhancement factor and is what separates the JONSWAP-spectrum from the PM-spectrum, giving the spectrum a more enhanced peak which is typical for a growing sea. σ_0 adjusts the width of the peak region.

The mean JONSWAP spectrum yields; $\gamma = 3.3$, $\sigma_0^{'} = 0.07$, $\sigma_0^{"} = 0.09$, while α and ω_p are expressed by the following;

$$\alpha = 0.076\left(\frac{gX}{U^2}\right)^{-0.22} \qquad \omega_p = 7\pi\left(\frac{g}{U}\right)\left(\frac{gX}{U^2}\right)^{-0.33} \tag{2.32}$$

Fig. 2.4 illustrates the evolving Jonswap-spectrum for a 20m/s constant wind speed varying with fetch. Notice how the components of highest frequencies and shortest wavelengths are generated first. As the wind perseveres, the peak frequency moves towards lower frequencies. This *downshift* of the spectrum continues as long as the wind speed is stronger than the phase speed of the propagating waves, given by eq. 2.7.

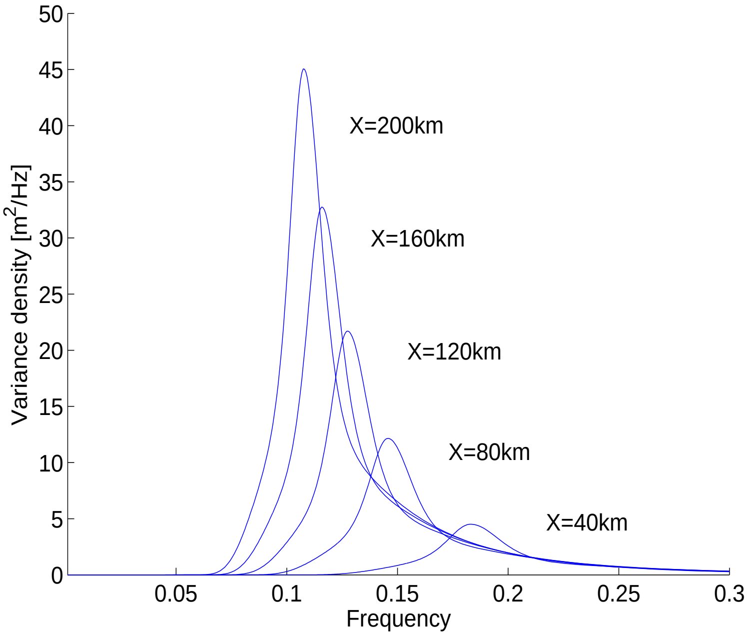

Figure 2.4: *A developing Jonswap-spectrum for a 20m/s constant wind speed, varying with fetch(X) given in kilometers.*

Chapter 3

Remote wave sensing

3.1 Remote sensing fundamentals

Most remote sensing methods with the aim of measuring surface waves are using active microwave sensors transmitting electromagnetic energy. Highly sophisticated signal analysis has made it possible to obtain information on the wave condition at the ocean surface by studying the reflected signal. In order to operate properly these systems are designed to depend on a few fundamental principals which will be introduced in the following sections.

3.1.1 Bragg scattering

Lets first consider an arbitrary transmitter of electromagnetic waves sending out energy spreading at an angel α towards the surface, see fig. 3.1. If the surface is perfectly level only a small area perpendicular to the surface will reflect the signal back, illustrated in fig. 3.1a). As soon as the surface is perturbed by waves, the backscatter increases in strength by the growing number of perpendicular facets, see fig. 3.1b) and c).

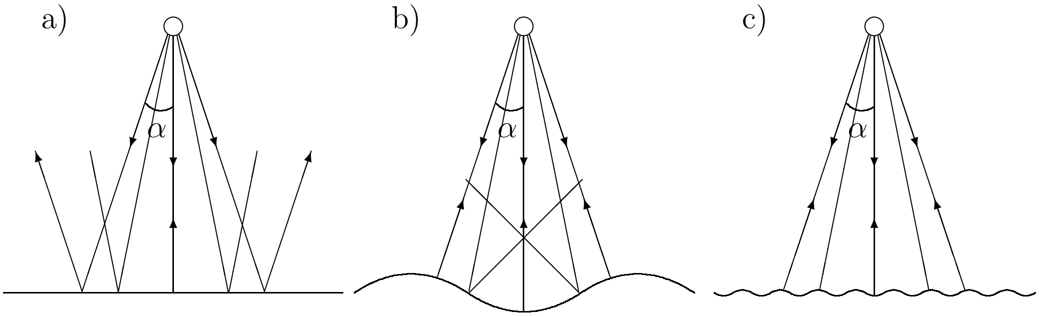

Figure 3.1: *Reflection characteristics for different surfaces, where α corresponds to the spreading angel of the transmitted signal.*

Now, consider a narrow beam of electromagnetic waves being transmitted at a grazing angel, θ, see fig. 3.2. Unlike fig. 3.1, here α is thought to be zero, focusing all the energy in one direction. Be aware that the evenly spaced rays of fig. 3.2 are all representing the narrow incoming beam. If the signal hits a rough surface perturbed by different wavelengths coming from different directions, the signal will be reflected in a variety of directions. Only those waves going directly toward or away from the source will give a significant echo. In this way, backscatter from waves going in other directions can be ignored. The strongest echo is obtained when the electromagnetic waves are scaled to the surface waves satisfying the *Bragg resonance condition*, expressed by

$$\lambda_s = \frac{\lambda_r}{2\cos\theta} \tag{3.1}$$

where:

λ_s	surface wavelength
λ_r	radar wavelength
θ	incidence angel

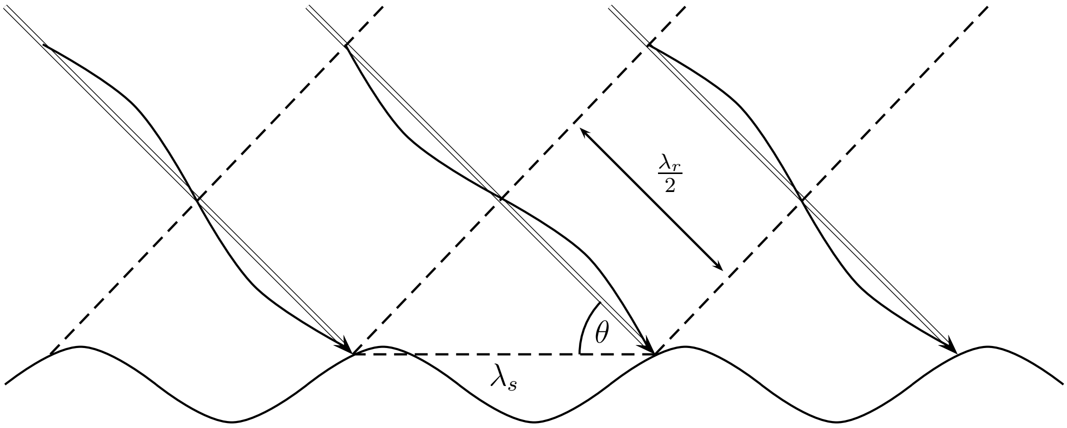

Figure 3.2: *Example where the Bragg scattering condition is satisfied using a sinusoidal wave, where the surface wavelength and wavelength of the signal is given by λ_s and λ_r respectively. θ is the incoming angel of the signal.*

This condition is met when the backscatter from one crest has exactly an integer number of wavelengths shorter or longer path then the backscatter from the next crest, see fig. 3.2. Other wavelengths will not offer the same coherent scatter as wavelengths satisfying eq. 3.1, and can therefore be filtered out(Shearman 1983).

3.1.2 Doppler effect

The Doppler effect is the frequency modulation we experience on an everyday basis. Take for instance the sound of a passing car that seems to send out a higher frequency sound when approaching than when driving away. This effect is caused by the relative movement between the sound-source and the receiver. The doppler effect is in fact observed in all cases of wave motion, with the exception of light that needs special consideration.

Lets first consider a stationary source sending out sound with a frequency f and a wavelength $\lambda = c/f$, c being the phase velocity of the sound relative to the air, and a receiver moving away from the source with a velocity v_r. The receiver experiences the speed of the sound to be less than c because it travels in the same direction as the sound. The relative velocity between the sound and the receiver is given by $c' = c - v_r$, meaning the frequency of the sound appears to the receiver to be

$$f_r = \frac{c'}{\lambda} = f\frac{c'}{c} = f\left(\frac{c - v_r}{c}\right) \tag{3.2}$$

In the opposite case, where the receiver is approaching the source, the sound has a higher relative speed than c and the frequency measured by the receiver will be given by the same expression as eq. 3.2 with the opposite sign.

Now, consider the sound source moving at a velocity v_s and the receiver being stationary. The phase speed of the sound is still c relative to the air, but the wavelength of the emitted signal vary. The wavelength depends on how far the source travels during one period relative to the foregoing maxima. This means the wavelength of the sound is shorter in the direction the source is moving $\lambda' = (c - v_s)/f$, and longer in the opposite direction $\lambda' = (c + v_s)/f$. The frequency measured at the receiver is now given by

$$f_r = \frac{c}{\lambda'} = f\left(\frac{c}{c \pm v_s}\right) \tag{3.3}$$

When sound is emitted by a stationary source and reflected back by a receding object eq. 3.2 and 3.3 may be combined to find the new frequency of the echo, given by

$$f_s = f\left(\frac{c - v_r}{c + v_r}\right) \tag{3.4}$$

For an approaching object the new frequency is also expressed by eq. 3.4, but with opposite signs. Now, if the frequency of the emitted and reflected signal and the phase speed is known eq. 3.4 may be solved on behalf of v_r to calculate the speed of the moving object. What we know as the *Doppler shift* is the difference in frequency in the transmitted and received echo, $\triangle f = f_d = f_r - f_s$. If $v_r \ll c$ the Doppler shift can be shown to be

$$f_d = \frac{2vf}{c} = \frac{2v}{\lambda} \tag{3.5}$$

3.1.3 Wave-wave interaction

The interaction between small-scale capillary waves and the much larger underlaying gravity waves is often referred to as the *two scale model.* The gravity waves affect the physical shape of the capillary waves in several ways (WMO 1998):

- ”Straining”, stretching and compressing the ripples caused by the orbital motion of waves
- Tilting the surface and changing θ in eq. 3.2
- Hydrodynamic interaction, most effectively found on the leading edge of the wave where the wind stress is at its strongest

In this way the echo is both amplitude and frequency modulated by the indirect interaction with gravity waves. Remote sensing is about detecting variations in the reflected signal caused by theses effects.

3.2 MIROS-radar

3.2.1 Features

The MIROS-module is a specially designed radar capable of measuring the directional frequency spectrum and currents at the ocean surface. It can be either platform mounted or installed on floating structures. In all its simplicity the entire system consists of an antenna with a microwave transmitter and receiver and a processing unit, illustrated in fig. 3.3. The physical shape of the antenna is constructed to radiate a 180 degrees sector of open ocean. This is sufficient to obtain a complete representation of the total wave condition, as the radar measures both approaching and receding waves. The free sight sector is resolved into another six sectors giving a 30 degrees resolution, see fig. 3.3 and 3.4.

The MIROS antenna is oblique looking, transmitting electromagnetic waves at a grazing angel $\theta = 10°$, almost pointing horizontally, or parallel with the surface, see fig. 3.4. E.g. when installed at a height of 70m, waves 400m away are being measured. The periodic pulses are transmitted at a 2Hz rate. It operates in C-band, which means the electromagnetic waves have a frequency of 5.8GHz with a corresponding wavelength of 5.17cm (Grønlie 1996).

3.2.2 Operation

The low grazing angel of the radar-signal sees to that no direct specular echo is retrieved from the gravity waves themselves. Instead, the radar uses the two scale model relying on the small-scale capillary waves riding on top of the much larger gravity waves.

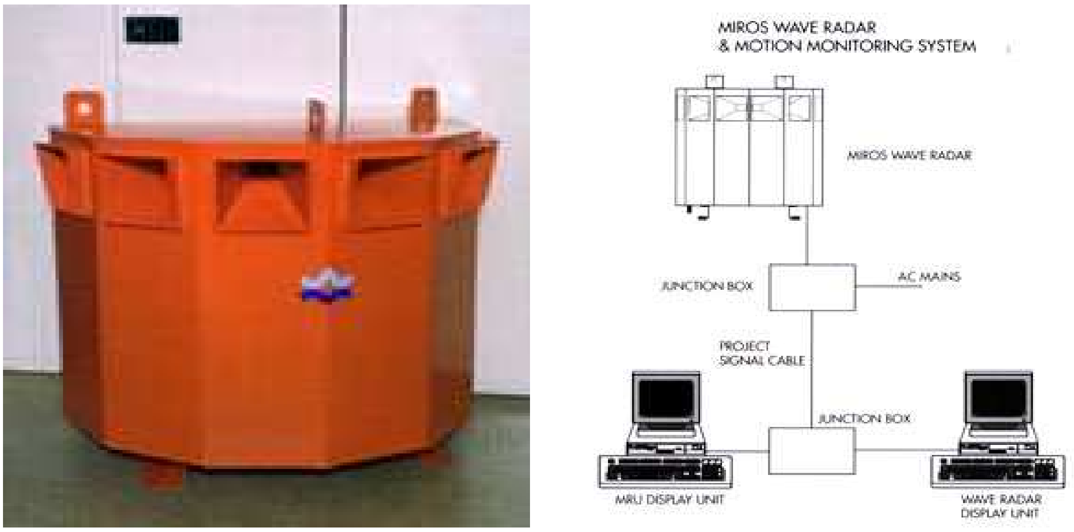

Figure 3.3: *The MIROS-radar(left) and the corresponding assembly(right) consisting of a transmitter/reciver-antenna, a processing-unit and a display-unit.*

According to the Bragg resonance condition, see eq. 3.1, the radar obtains the strongest echo from capillary waves with a wavelength of about 2.6cm. The echo is range-gated, meaning other echoes from outside the footprint is excluded. The footprint is defined in azimuth by the physical shape of the radar and in the radial by the length of the pulse in time. With a 2Hz rate the radial depth of the footprint is small compared to the gravity waves of interest. The radar illuminates two closely positioned footprints, see fig. 3.4, to solve the 180 degrees ambiguity problem, commented in the next section.

The radar is working in a pulse doppler mode. Coherent pulses of electromagnetic waves are sent toward the surface and the doppler shift in the echo is measured. The instantaneous doppler shift, see eq. 3.5, is an indirect measure of the average water particle velocity taken at the footprint. The low phase speed of the capillary waves

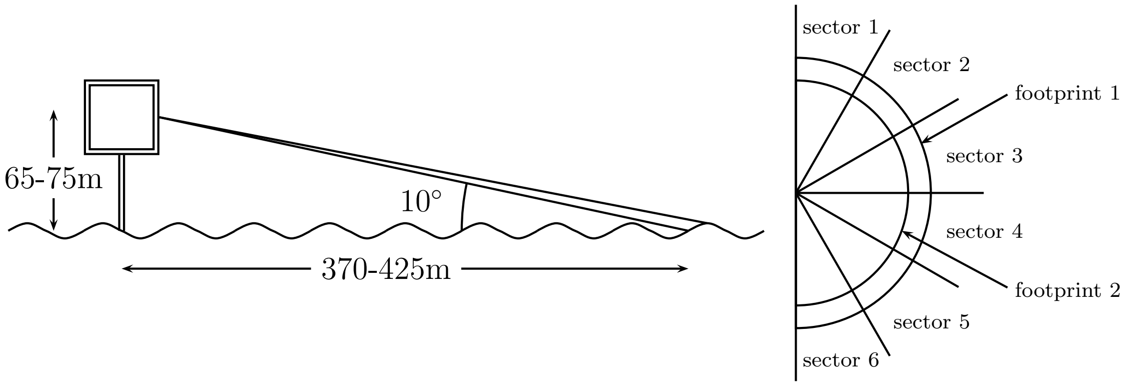

Figure 3.4: *The MIROS-radar is installed at a height of 65-75m. The surface is illuminated at two footprints at a grazing angle of* 10°*, covering 6 sectors of* 30°*.*

means they are proportional to the particle velocity at the surface. As described in chapter 2, the sea surface is the sum of a great number of wave components. The particle velocity will be, to the first order, the vector sum of the orbital motion of all wave components present, in addition to any underlaying currents.

3.2.3 Signal processing

The process of transforming the doppler shift into a directional frequency spectra is a complicated matter. Only a rough description will be made in the following.

The 'raw' velocity information is a 128 seconds time series of 258 samples (2Hz). The series is divided into smaller intervals of time T. These intervals are Fourier transformed and the mean frequency, the Doppler frequency, is retrieved. The new time series of Doppler frequencies is then frequency to voltage converted by multiplying with a constant, and then Fourier transformed once more to obtain the complex amplitude spectra. This procedure is done for both footprints. Next, the cross spectrum of the two amplitude spectra is calculated, which provides an explicit expressions for the average water particle velocity spectrum for both receding and approaching waves (Grønlie 1999).

Through linear wave theory, MIROS has developed a transfer function(confidential). By multiplying the velocity spectra with the this function the desirable directional frequency spectrum is deduced. In the following a basic understanding of the transfer function is presented.

3.2.4 Transfer function

Lets consider a surface only perturbed by a single sinusoid with the angular frequency, Ω. In the line of sight, the particle velocity of the surface can be expressed by

$$v(t) = \Omega \frac{H}{2} \sin(\Omega t + \phi) \tag{3.6}$$

Based on eq. 3.5, the doppler shift is given as

$$f_d(t) = \frac{H\Omega}{\lambda_0} \sin(\Omega t + \phi) \tag{3.7}$$

with an frequency to voltage converter, β, the new time series is expressed by

$$s(t) = \beta \frac{H\Omega}{\lambda_0} \sin(\Omega t + \phi) \tag{3.8}$$

The amplitude spectrum of eq. 3.8 will only be a single line at $\omega = \Omega$. When integrating over all frequencies, in this case only a single frequency, the power in 3.8 is obtained

$$P = \frac{1}{2} \left(\frac{\beta H \Omega}{\lambda_0} \right)^2 \tag{3.9}$$

Solving eq. 3.9 with respect to the squared wave-height gives

$$H^2 = P_{\omega=\Omega} 2 \left(\frac{\lambda_0}{\beta \Omega} \right)^2 \tag{3.10}$$

From eq. 3.10 the transfer function may be defined by

$$TF(\omega) = 2 \left(\frac{\lambda_0}{\beta \omega} \right)^2 \tag{3.11}$$

considering the surface to be perturbed by a number of wave components of frequencies, ω. This portraits the basic idea of the relation between the Doppler spectrum and the wave-height(Grønlie 1999).

3.2.5 Output data

The MIROS output data are presented using two different formats, DF005 and DF038. Both formats comprehend the complete directional frequency spectrum. For DF005, the spectrum covers a total of 180 degrees, but is representing approaching and receding waves by posting positive or negative values for each directional-frequency bin. In addition, the DF005 contains several parameters calculated by the MIROS signal processing unit.

The 2D spectrum has a frequency resolution of 0.0078125Hz, see fig. 3.5. DF005 spans the interval 0-0.3125Hz and DF038 0.0313-0.3125Hz, see fig. 3.5. The directional resolution is either 10 or 30 degrees and the data are posted every 15 or 20 minutes.

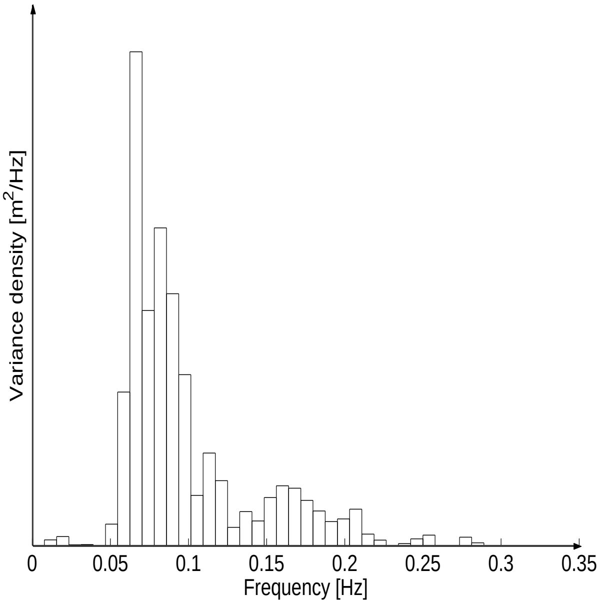

Figure 3.5: *Frequency resolution used by the Miros-radar, DF005 -and DF038 format*

Chapter 4

Wave modelling

4.1 The wave energy balance equation

In wave modelling theoretical and observational knowledge on ocean surface waves are combined and expressed highly mathematical. The purpose of the model is to be a practical tool able to simulate the wave condition just by knowing a few easy measurable quantities. Since wind is the primary force driving waves, most models only require surface winds to operate. However, as wave models become increasingly perfected more input parameters may be necessary to maintain progress, e.g. air-sea temperature.

The wave spectrum is the most common way of describing the wave condition at a ceratin location. In modelling its evolution in time and space is often calculated using the wave energy balance equation, expressed by

$$\frac{\partial E}{\partial t} + \nabla \cdot (c_g E) = S_{in} + S_{nl} + S_{ds} \tag{4.1}$$

Eq. 4.1 is only valid in deep water. Other mechanisms also affecting the wave spectrum, like shoaling effects and currents, are not considered here.

The left hand side of eq. 4.1 constitute a local term and an advective term moving at the group velocity, c_g. The evolution of the spectrum is depending on three source functions, wind input(S_{in}), nonlinear interaction(S_{nl}) and dissipation(S_{ds}). There are continuous work being done to optimize the source function parameterizations. However, today still a lot of physical aspects concerning ocean waves are not fully understood. Empirical studies have only given us parts of the picture. In the following section the source functions are briefly discussed, with primarily focus on their influence on the wave spectrum.

4.1.1 Wind input

On short timescales wind is the only significant source of energy input to the ocean surface apart from landslides and earthquakes below the surface. The transfer of momentum between the atmosphere and ocean is a function of stress between the two media. This process is seemingly affected by several mechanisms and will be presented more in depth in chapter 5.

Quite a few studies on wind wave growth have been presented over the years, where the works by Phillips (1957);Miles (1957) stick out as the milestones. Even though the theory proposed by Miles (1957) is generally thought to give an underestimated wave growth, it still constitutes a foundation for most studies on this topic today. Several scientists have developed modified versions of Miles' theory. However, these will not be presented here. Instead a coarse description of how the wind input, S_{in}, affects the appearance of the wave spectrum is given.

Fig. 4.1 illustrates how the three source terms vary with frequency in two duration limited cases, after 3 and 96 hours respectively (Komen et al. 1996). The wind input source function is represented by connected open circles and is as expected always positive. The peak of the source term corresponds to the peak of the wave spectrum, not shown in fig. 4.1, and is similar to its overall shape, besides being less energetic. Notice how the wind input decreases with wave age, being almost divided in half comparing 3 and 96 hours duration.

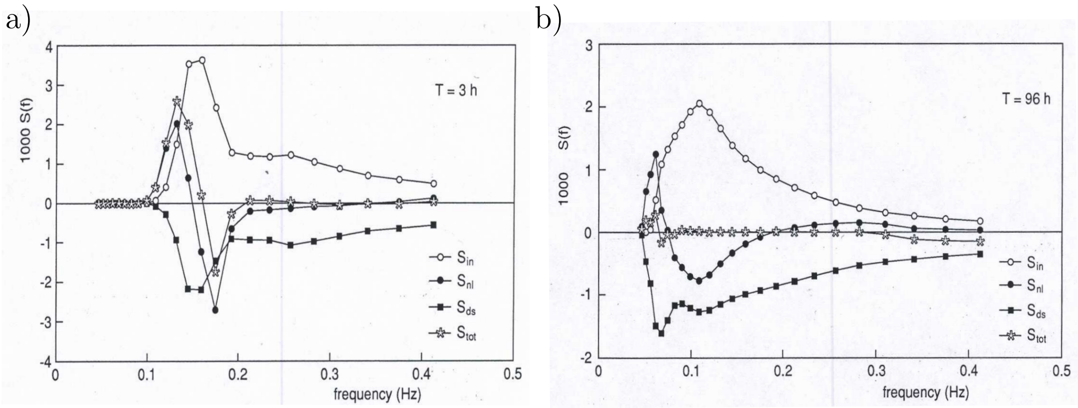

Figure 4.1: *Simulated source functions S_{in}, S_{ds} and S_{nl} for two duration limited cases obtained by the WAM-model. a) 3 hours and b) 96 hours. Figures are taken from Komen et al.(1996)*

4.1.2 Nonlinear interaction

The evolution of wind generated waves can to a certain degree of accuracy be expressed by linear theory which is possible because waves on average are not very steep. Once the steepness of the wave field increases, as is the case for wind-sea, the nonlinear processes grow more important to the evolution of the wave spectrum. The effect of nonlinear interaction is transference of energy between wave components of different frequencies. This redistribution of energy occur when interacting wave components are in resonance. The process is conservative, not affecting the total amount of energy of the wave spectrum.

The S_{nl} is perhaps the most debated source function in the energy balance equation. The pioneering work by Hasselmann (1962) established a theoretical framework for the problem. His four-wave interaction model is a very complex and time consuming integral not to be discussed here.

The nonlinear term is characterized by a three lobe structure of opposite signs. In general, energy is being transported from frequencies around the peak of the spectrum towards higher and lower frequencies of the spectrum, with the majority going towards the latter. The nonlinear term is represented by connected black dots in fig. 4.1. For young seas, see fig. 4.1a), the positive lobe at low frequencies are centered slightly to the left of the peak frequency. This creates the *downshift* of the spectrum observed in developing seas. In the case of old seas the same positive lobe is centered closer to the peak frequency, giving a much weaker downshift. The positive lobe at the higher frequencies is smaller, but has a stronger directional distribution, giving rise to a broadening of the spectrum.

4.1.3 Dissipation

Dissipation is the least understood aspect of wind generated waves. Loss of energy in the wave field can be due to several mechanisms, like the interaction of waves with the bottom in terms of friction and wave breaking (shoaling), internal processes by viscosity and in the surface by white capping. Here, the emphasize will be on deep water where bottom interaction is negligible. The drain of energy by viscose processes are well known, but only important for wave lengths in the capillary region. The main energy loss in deep water is due to wave breaking, also known as white capping. White capping is a strong nonlinear process hard to formulate mathematically. It is highly irregular, where the actual threshold for breaking is not well understood(Massel 1996). As with the two prior source functions, only the main effect of dissipation by white capping will be presented.

Not surprisingly, also this mechanism changes with wave age. Fig. 4.1a) illustrates how the dissipation source function is more or less the mirror of the wind input after 3 hours, only slightly weaker. For an old sea, fig. 4.1b), the effect is reduced, however not as much as the wind input. Because the sea state is getting closer to its saturated state, the wind input and dissipation is almost in balance.

The sum of the three source functions are illustrated by connected stars in fig. 4.1. Notice the change in magnitude of the two functions. This is a logical behavior considering the difference in wind speed and phase speed of the dominating wave components are getting smaller with wave age.

4.2 A historical perspective on wave modelling

The need for reliable wave prediction models have become increasingly important in modern society. It is essential that the likes of oil and shipping industry receive accurate wave forecasts to operate in a safe and efficient manner. More than half a century ago the first numerical wave model was established by Gelci et al. (1957). Since then numerical modelling has come a long way. Not only do we understand the physical aspects of ocean surface waves better, now we have computer power able to calculate vast quantities of mathematical equations in a short matter of time. Still all numerical wave prediction models are based on the strive to solve the wave energy balance equation with its corresponding source terms. In the lights of this we have seen the rise of a first, second and today's third generation models.

What mainly separates the three generations of wave models are the different ways the source functions are parameterized. Especially the nonlinear term has been a huge topic of discussion. At the time Gelci et al. (1957) developed their first model the physical understanding of wind generated waves was vague, and reflected in the quality of the model. However, around the same time the important works of Phillips (1957), Miles (1957) and Hasselmann (1962) were published. These studies set the framework for future wave modelling. As a consequence, a number of new models saw the daylight in the 60s and 70s (Massel 1996).

In general, the first generation wave models did not consider any energy transference between wave components. Nonlinearities were simply ignored, $S_{nl} = 0$, or modelled in a way that had little effect on the total energy balance. Atmospheric input by wind, S_{in}, was expressed linearly and generally overestimating the energy transference. Dissipation was modelled by establishing a limiting form of the wave spectrum where the waves suddenly stopped growing. A f^{-5} saturation range was prescribed by Phillips (1958).

After extensive field and laboratory work during the 70s doubt spread about the quality of the first generation wave models. Scientists grew aware of the neglected effect of nonlinearities, as the forward face of the simulated spectrum simply grew to slow in developing seas. An attempt was also made to simulate the observed *overshoot* phenomenon of the wave spectra. In the light of this new understanding a new type of models were established. In general, we distinguish between three types of second generation models, the *discrete spectral models*(DS), the *parametric models*(P) and the combined *hybrid models*(H).

In the DS-models the wave spectrum is represented by discrete directional-frequency bins at times $t_0 + n\Delta t$ at each grid point. The energy balance equation is then solved numerically within the model area. The SWAMP-group (1985) reviewed three different types of DS-models in which all use a linear wind input function in accordance to the measurements of Snyder et al. (1981). They are limited in their growth by some form of saturation spectrum depending on the stage of development. In most models the

JONSWAP and PM spectra are used. What mainly separates these models are the way the nonlinear source function is treated. One way of solving this problem is by involving the S_{nl} implicitly in the S_{in} and S_{dis}, or by giving a coarse parametrization of the nonlinear term. The main drawback of the DS-model is the amount of calculations needed for its execution, which is drastically reduced in the P-models.

The P-models are based on the idea that as long as the nonlinear term is recognized as a controlling process, there are no need to express the other source functions in any more detail. Since the models at the time did not calculate the nonlinear source function exactly, the S_{in} and S_{dis} did not need to be expressed more precisely. Hasselmann et al. (1976) developed the first P-model. Unlike the DS-model, the wave condition and its evolution was characterized using only a few parameters. Unfortunately, the P-models only apply to developing waves and is not valid for waves outside the generating area. In other words, swell must get special attention. This is solved by combining a DS-model with a P-model, recognized as a H-model. The P-model controls the developing sea and the DS-model simulates the swell.

4.3 A third generation wave model: WAM(cycle-4)

The SWAMP-group (1985) concluded that all second generation models suffered from limitations in the nonlinear source function parametrization. Generally they performed satisfactory in fetch and duration limited cases, but showed weaknesses in extreme events with strongly varying wind fields, e.g. hurricanes, where accurate wave prediction is of special importance. By the mid-1980s numerical improvements (Hasselmann and Hasselmann (1985); Snyder et al. (1993)) made it possible to calculate the Boltzmann-type integral, the nonlinear source function, explicitly. This set the framework for the WAM(WAve-Model)-model which is described in great detail in Komen et al. (1996). In the following a brief introduction of the kinematics, source function parameterizations and numerical schemes used in the model are presented.

4.3.1 Kinematics and parametrization in the energy balance equation

The WAM-model is of the DS-type and was first implemented in 1988. It calculates the action density spectrum instead of using the variance density spectrum, defined by

$$N(f,\theta) = \frac{E(f,\theta)}{f} \tag{4.2}$$

Depending on the model area, suitable grid coordinates are chosen. In the case of a global model, the 2D spectrum is a function of angular frequency, propagation direction, latitude, longitude and time, $N(\omega, \Theta, \phi, \lambda, t)$. The energy balance equation is expressed as follows

$$\frac{\partial N}{\partial t} + (cos\phi)^{-1}\frac{\partial}{\partial \phi}(\dot{\phi}cos\phi N) + \frac{\partial}{\partial \lambda}(\dot{\lambda}N) + \frac{\partial}{\partial \omega}(\dot{\omega}N) + \frac{\partial}{\partial \theta}(\dot{\theta}N) = S \tag{4.3}$$

in which

$$\dot{\phi} = \frac{d\phi}{dt} = (c_g cos\theta + \mathbf{U}|_{north})R^{-1} \tag{4.4}$$

$$\dot{\lambda} = \frac{d\lambda}{dt} = (c_g sin\theta + \mathbf{U}|_{east})(Rcos\phi)^{-1} \tag{4.5}$$

$$\dot{\theta} = \frac{d\theta}{dt} = c_g sin\theta tan\phi R^{-1} + \dot{\theta}_D \tag{4.6}$$

$$\dot{\omega} = \frac{\partial \Omega}{\partial t} \tag{4.7}$$

and

$$\dot{\theta}_D = \left(sin\theta \frac{\partial}{\partial \phi}\Omega - \frac{cos\theta}{cos\phi}\frac{\partial}{\partial \lambda}\Omega \right)(kR)^{-1} \tag{4.8}$$

where c_g is the group velocity, R the radius of the earth, $\Omega = \sigma + \mathbf{k} \cdot \mathbf{U}$ the dispersion relation accounting for any mean currents and S the sum of the source functions;

$$S = S_{in} + S_{nl} + S_{dis} + S_{bot} \tag{4.9}$$

Today the physical knowledge on S_{in} and S_{nl} are both of such complexity, that both terms need considerably computer power to be exactly calculated. It is therefore necessary to parameterize these two source functions into more time efficient expressions.

The wind input term is based on the theory proposed by Miles (1957). By always assuming a logarithmic wind profile, he concluded the growth rate of wind generated waves only to depend on two parameters

$$x = \frac{u_*}{c}cos(\theta - \phi) \quad \text{and} \quad \Omega_m = \kappa^2 \frac{gz_0}{u_*^2} \tag{4.10}$$

where $\kappa = 0.4$ is the von Kármán constant, c the phase speed of the waves, θ the direction in which the waves propagate and ϕ the wind direction. Ω_m is known as the profile parameter. These two parameters depends on the roughness of the airflow above the surface and is therefore dependent on the sea state. The WAM-model uses a growth rate, γ, defined by Janssen (1991) expressed as

$$\frac{\gamma}{\omega} = \epsilon \beta x^2 \tag{4.11}$$

Here, ϵ is the air-water density ratio, $\rho_a(0)/\rho_w(0)$ and β the so-called Miles parameter, which is defined by

$$\beta = \frac{\beta_m}{\kappa c}\mu ln^4(\mu), \quad \mu \leq 1 \tag{4.12}$$

where β_m is a constant and μ defined by

$$\mu = \left(\frac{u_*}{\kappa c}\right)^2 \Omega_m exp\left(\frac{\kappa}{x}\right) \tag{4.13}$$

The input source term of the WAM-model is given by

$$S_{in} = \gamma N \tag{4.14}$$

where N is the action density spectrum.

Eq. 4.10-4.14 are dependent on the stress of air flow over the surface which again depends on the sea state. Janssen (1991) considered the momentum balance of air and found the kinematic stress to be expressed as

$$\tau = u_*^2 = \left(\kappa \frac{U(z_{obs})}{ln\,(z_{obs}/z_0)}\right)^2 \tag{4.15}$$

where u_* is the friction velocity, z_{obs} is the mean height above the waves and the roughness length is defined by

$$z_0 = \frac{\hat{\alpha}\tau}{g\sqrt{1-y}}, \quad y = \frac{\tau_w}{\tau} \tag{4.16}$$

τ_w is the stress induced by the surface waves and is defined by

$$\tau_w = \epsilon^{-1} g \int d\omega d\theta\, \gamma N \mathbf{k} \tag{4.17}$$

Whenever the wave induced stress becomes of the order of the total stress the roughness length gets enhanced and the momentum transfer from air to sea is more efficient.

Finally we are left with two unknown constants, β_m and $\hat{\alpha}$, which have both been estimated by comparing observational and numerical results to find the best fit. They are found to be $\beta_m = 1.2$ and $\hat{\alpha} = 0.01$.

The dissipation term of the WAM-model has a less complicated form than the input and nonlinear term. This is basically because dissipation by whitecapping is a highly nonlinear term not well understood. The term is given by

$$S_{dis} = -C_{dis}\,\bar{\omega}\,(\bar{k}^2\, m_0)^2 \left[\frac{(1-\delta)k}{\bar{k}} + \delta\left(\frac{k}{\bar{k}}\right)^2\right] N \tag{4.18}$$

Here $\bar{\omega}$ and $\bar{k}$ are the mean angular frequency and mean wave number respectively. In practice, the constants are set to $C_{dis} = 4.5$ and $\delta = 0.5$. It should also be mentioned that the dissipation term by bottom friction is expressed as

$$S_{bot} = -C_{bot} \frac{k}{sinh(2kh)} N \tag{4.19}$$

where $C_{bot} = 0.038/g$ and h is the depth.

The Boltzmann-type integral is a highly time consuming expression to calculate exactly. In the WAM-model the integral is parameterized using the DIA(discrete interaction approximation) (Hasselmann and Hasselmann (1985); Hasselmann et al. (1985)). Without going to much into detail, this approach applies the same integration method used to integrate the exact source term, but instead of integrating over the five-dimensional interaction phase space, the integration is taken over a two dimensional continuum and two discrete interactions. The reader is referred to Hasselmann and Hasselmann (1985) for an in depth presentation.

4.3.2 Numerical schemes

Fig. 4.2 illustrates the most commonly used frequency resolution of the WAM-model, with a minimum frequency $f_{min} = 0.042$ and a maximum frequency $f_{max} = 0.42$. In between, the discrete frequency centers are represented by $f_i = (1.1)^{i-1} f_{min}$. This offers a total of 25 frequency bands, $i = 25$, where each individual interval is defined by $\Delta f = 0.1f$. The frequency bands are represented in 24 directional sectors, offering a 15° resolution.

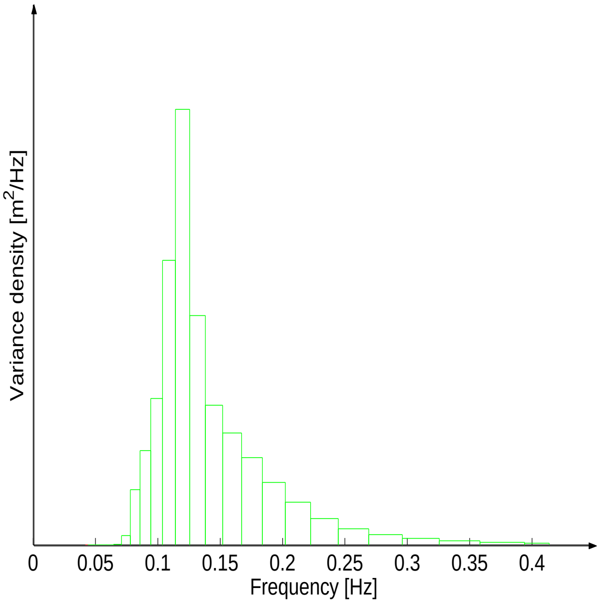

Figure 4.2: *Frequency resolution used in the WAM-model*

In the WAM-model, the wave spectrum distinguishes between a prognostic part, f_{min} to f_{hf}, and a diagnostic part. The diagnostic part is represented by an predetermined f^{-5} tail and has the same directional distribution as the last frequency band of the prognostic region. The tail is expressed given by;

$$E(f,\theta) = E(f_{hf},\theta) \left(\frac{\bar{f}}{f_{hf}} \right)^{-5} \quad \text{for} \quad f > f_{hf} \tag{4.20}$$

, where the high-frequency limit is defined by

$$f_{hf} = \min\{f_{max}, \max(2.5\bar{f}, 4f_{PM})\} \tag{4.21}$$

With the high frequency limit the spectrum is scaled for young waves by the mean frequency $\bar{f}$ and for more developed wind-seas by the Pierson-Moskowitz-frequency $f_{PM} = 4.57 \cdot 10^{-3}$ (Massel 1996). The diagnostic tail is mainly needed to compute the nonlinear transfer and the dissipation of the prognostic region. While the diagnostic part of the wave spectrum is predetermined, the prognostic part has to be calculated numerically by solving the energy balance equation.

Source functions

The WAM-model uses an implicit second order scheme to simulate the evolution of the source terms. The advantage of this scheme is found in its ability to use an integration time-step that is greater than the dynamical adjustment time of the highest frequencies still treated prognostically in the model.

The implicit second order, centered difference equation is expressed by

$$E_{n+1} = E_n + \frac{\Delta t}{2}(S_{n+1} + S_n) \tag{4.22}$$

where Δt is the time step and n refers to the time level. If the source functions had been linear eq. 4.22 could have been solved directly. Since this is not the case a Taylor expansion is introduced

$$S_{n+1} = S_n + \frac{\partial S_n}{\partial E}\Delta E + ... \tag{4.23}$$

S_{n+1} is then expressed numerically by a discrete matrix, M_n, and divided into a diagonal,Λ_n, and non-diagonal matrix, N_n

$$\frac{\partial S_n}{\partial E} = M_n = \Lambda_n + N_n \tag{4.24}$$

By substituting eq. 4.23-4.24 into 4.22, and considering that the source terms may depend on the friction velocity u^*, it can be showed that the change of the wave spectrum, $\Delta E = E_{n+1} - E_n$, is given by

$$\Delta E = \frac{\Delta t}{2}\left(S_n(u_*^n) + S_n(u_*^{n+1})\right)\left[1 - \frac{\Delta t}{2}\Lambda_n(u_*^{n+1})\right]^{-1} \tag{4.25}$$

Computations show that the non-diagonal contribution is insignificant and is therefore not taken into account.

Advection and refraction

The advection term of the energy balance equation is expressed in flux form and its evolution is solved using a first order up-winding scheme. This scheme is chosen because it is easy to implement, requiring less computer time and memory. And, the results have been satisfactory.

Here, only an one dimensional case is illustrated, simply because the analogy to more dimensions is straight forward. Lets consider the advection equation given by;

$$\frac{\partial}{\partial t}E = -\frac{\partial}{\partial x}\Phi, \tag{4.26}$$

where $\Phi = c_g E$, then the rate of change of the spectrum in the jth grid point is given by;

$$\Delta E_j = -\frac{\Delta t}{\Delta x}(\Phi_{j+1/2} - \Phi_{j-1/2}). \tag{4.27}$$

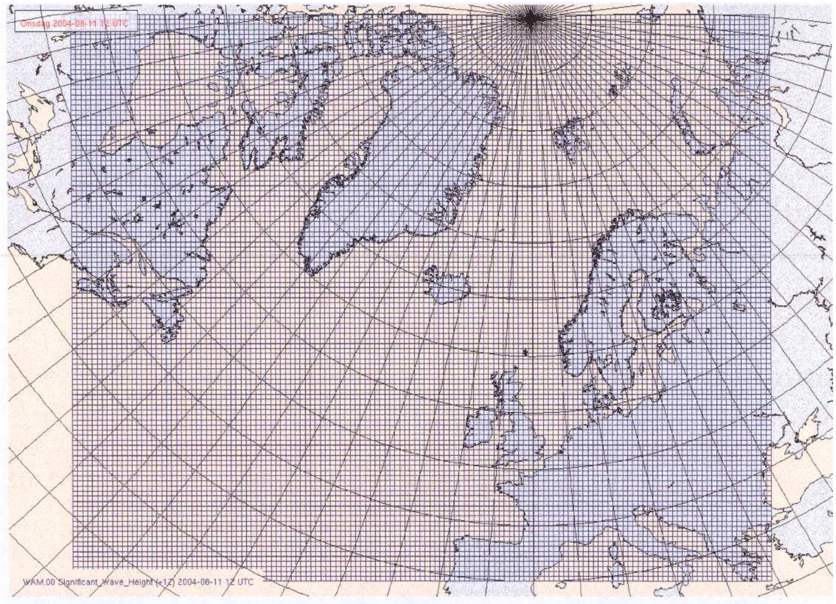

Figure 4.3: *The area of which the WAM-model is run operationally at met.no. The grid spacing is given at 50km.*

Here the Δx is the grid spacing and;

$$\Phi_{j\pm1/2} = \frac{1}{2}[v_j + |v_j|]E_j + \frac{1}{2}[vj - |v_j|]E_{j+1} \tag{4.28}$$

where $v_j = 0.5(c_{g,j} + c_{g,j\pm1})$ is the mean group velocity. This concludes the numerical schemes used in the WAM-model.

4.3.3 The WAM-model run at met.no

Set-up/Grid and boundary conditions

At the Meteorological Institute of Bergen(met.no) the WAM-model is run operationally. The modelled area, see fig. 4.3, has a grid spacing of $\Delta x = 50$km and closed boundaries set to zero. Energy generated outside the boundaries, advected across, are not simulated.

Input/Output

The WAM-model is, as mentioned, only dependent of 10m winds covering the modelled area. At met.no these wind fields are obtained from the atmospheric model HIRLAM-20, introduced in the next section, forcing the wave model every three hours. Integration time step is $\Delta t = 15$min. Wind fields for each time step are calculated using linear interpolation in between every three hours the HIRLAM-20 simulates new wind fields.

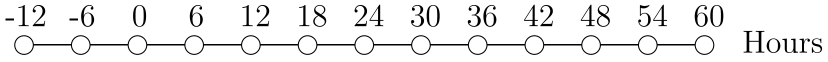

Figure 4.4: *At met.no the WAM-model offers output data at the following hours. -12h to 0h are based on analyzed winds, while the rest are based on prognosis.*

The software package of the WAM-model is made flexible so the user may choose the composition of the output data, which also apply to the time intervals the simulations are posted. At met.no two types of output formats have been used in general. Type 1 offers the full 2D directional frequency spectrum and the parameters; H_s, T_p, TH_p(peak direction), T_{m0-1} and T_{m02} for the chosen position. In addition, the locally simulated wind is presented. Operationally, type 1 is posted every six hours. Each output give data representing present time (0 hours) and hindcasts for -12 and -6 hours, see fig. 4.4. These data, including 0 hours, are based on analyzed HIRLAM wind fields. Prognosis are given up until 60 hour in advance, illustrated in fig. 4.4.

The type 2 format only offers parametric values; Hm0, Tp, Tm02 and THp representing the total sea, wind-sea and swell, in addition to wind. This type of data are posted every three hours.

HIRLAM

The latest version of the atmospheric model HIRLAM, version 5.2.3, was implemented March the 20th 2003 at met.no. There are currently three different model set-ups, HIRLAM-5, HIRLAM-10 and HIRLAM-20, in use at the institute, differing in horizontal resolution, grid spacing, and area coverage. The model forcing the WAM-model, HIRLAM-20, has the sparsest resolution with an 0.2° grid spacing and 468x378x40 grid points. The boundary conditions are relaxed to ECMWF-data with an 0.5° spacing, forcing the model every 3hours. HIRLAM-20 data are posted every 3hours and offers, as the WAM-model, up to +60h forecasts. Even though the model has 40 vertical levels of wind data, the WAM-model is only dependent on the winds of the lowest level, at 10m (Vignes 1998).

Chapter 5

The drag coefficient in the presence of swell

The ocean-atmosphere is a coupled thermodynamic system. That is, if the characteristics of one fluid changes, e.g. temperature, momentum, pressure, gas content etc., the other will respond to obtain balance at the interface. Wind generated surface waves are the result of momentum transference from air to sea. The exchange rate depends on the friction between the two media, represented by the stress, $\vec{\tau}$. In general, the mean horizontal momentum equation of the atmosphere can be expressed by

$$\frac{d\mathbf{u}}{dt} = -\frac{1}{\rho_a}\nabla_h p + f_c\mathbf{u}\times\mathbf{k} + \frac{1}{\rho_a}\frac{\partial\vec{\tau_h}}{\partial z} \tag{5.1}$$

in which $\mathbf{u}$ is the mean horizontal velocity component, ρ_a is the atmospheric density, f_c is the Coriolis parameter, $\vec{\tau_h}$ is the horizontal stress vector and $\mathbf{k}$ is the vertical unit vector. However, the lowest part of the boundary layer, also known as the constant stress layer, is dominated by friction, reducing eq. 5.1 to

$$\frac{\partial\vec{\tau_h}}{\partial z} = 0 \tag{5.2}$$

The thickness of the constant stress layer varies, but is often described as the lowest 10m above the sea surface (Komen et al. 1996). The total stress, $|\vec{\tau_h}| = \tau$, consists of a viscose-term and a turbulence-term

$$\frac{\tau}{\rho_a} = u_*^2 = \nu_a\frac{\partial\mathbf{u}}{\partial z} - \overline{\mathbf{u}'w'} = constant \tag{5.3}$$

where $\mathbf{u}'$ and w' are the horizontal and vertical components of random velocity fluctuations, u_* is the friction velocity and ν_a is the kinematic viscosity of air. The over bar indicates a time averaging, usually set to 20 minutes. Only in a very thin layer close to the ground(∼1mm) the viscose-term is of any significance. Elsewhere, within the constant stress layer, the turbulence-term is far superior, reducing eq. 5.3 to

$$\tau = \rho_a u_*^2 = -\rho_a\overline{\mathbf{u}'w'} \tag{5.4}$$

It has been normal practice to express the stress as a function of wind speed and a drag coefficient, C_d, at a height z, expressed by

$$\tau = u(z)^2 C_D(z) \tag{5.5}$$

Considering a logarithmic wind profile in neutrally stratified conditions

$$u(z) = \frac{u_*}{\kappa} ln \left(\frac{z}{z_0} \right) \tag{5.6}$$

the sea surface drag can equivalently be expressed by a roughness length, z_0

$$C_d = \frac{\kappa^2}{ln^2 \left(\frac{z}{z_0} \right)} \tag{5.7}$$

where $\kappa = 0.4$ is the von Kármaán constant.

In order to improve our knowledge on the growth rate properties of wind waves, it all comes down to finding those mechanisms affecting the drag coefficient. This problem has acquired considerable attention for more than four decades (Drennan et al. 1999). Several studies have tried to parameterize the surface stress using easy measurable quantities, such as mean wind speed and atmospheric stability. However, large scatter in the data have forced the wave community to consider alternative mechanisms affecting the stress.

It was first proposed by Charnock (1955) that the roughness length above the sea surface varies with wind speed. Since then other studies (Smith 1980; Large and Pond 1981; Taylor and Yelland 1996) have concluded the drag coefficient in neutrally stratified conditions to be dependent on wind speed alone. A summary of previous works are presented in Geernaert and Plant (1990). However, in general, only a weak wind speed dependence has been found, with a significant scatter. The drag coefficient varies within the individual experiments and from study to study.

The weak wind speed dependence required scientists to consider other possible mechanisms affecting the drag coefficient. Donelan et al. (1990); Smith et al. (1992); Donelan et al. (1992) found an additional dependence on the development of the wave field, expressed by the wave age, c_p/u_*, where c_p is the phase speed of the waves at the peak of the spectrum. It was concluded that the drag coefficient is reduced for increasing wave ages and vice versa for young seas. This result proved to be of special importance in near-shore areas and in intense storm situations, where conditions often are idealized fetch or duration limited cases. However, there is a drawback with relating the drag coefficient to the wave age. In the open ocean most wind-sea systems are close to being fully developed. In that way, wave age effects are not easily discern.

Swell has been proposed as another possible factor influencing the wind-sea growth rate, or the drag coefficient. So far, most studies have been conducted in laboratories, but with inconclusive and at times contradictory results. A summary of selected earlier works is given in Hanson and Phillips (1999). Also based on laboratory data, Donelan (1987) found gentle swell to significantly affect the development of wind-sea. This was supported by the field work of Donelan et al. (1997); Drennan et al. (1999), which reported an enhancement in the drag coefficient in conditions of swell propagating across or opposite to the direction of the wind. Both works concluded that much of the scatter found in the drag coefficient measurements most likely could be attributed to the presence of swell. However, Dobsen et al. (1994), where conditions of both pure wind-sea and mixed swell/wind-sea were investigated, did not find the drag coefficient to be affected by swell. In the theoretical work of Kudryavtsev and Makin (2004), a model describing the impact of swell on the atmospheric boundary layer was proposed. The model results found the drag coefficient to be significantly enhanced in conditions of wind opposing swell and less pronounced in cross-swell cases. It should be noted that these results were obtained in low wind speed conditions.

While most earlier works have been based on direct stress measurements, (Donelan et al. 1997; Drennan et al. 1999; Dobsen et al. 1994), laboratory testing (resumed in Hanson and Phillips 1999) and theoretical approaches (Kudryavtsev and Makin 2004), there are other ways of testing the 'swell-altering effect on the drag coefficient'-hypothesis. In the work of Ardhuin (Sub), data obtained from the east coast of the U.S. during the SHOWEX-project, described in Ardhuin et al. 2003, was analyzed. From August to December 1999 six buoys, giving the full 2D directional frequency spectrum, were deployed in a line stretching about 80km off the coast. Out of the 5 months time series the 3rd of November came closest of resembling idealized fetch-limited conditions. Fairly uniform winds(U_{10}) blowing offshore at an angel of $20-30°$ to the shore-normal was met by an opposing moderate amplitude swell. The measured wave spectra were averaged over a 5 hour period from 1200 to 1700EST when the wave conditions were fairly steady. Two numerical wave models, Wavewatch3 and Crest, of different advection schemes, were implemented with the source functions of WAM cycle-3 and cycle-4, with minor adjustments. The Wavewatch3 was run with a 1.5-1.8km spacial resolution and integrated over a 60s time step. The wave conditions of the 3rd of November were then simulated using the different model combinations forced by short term forecast winds obtained from the COAMPS atmospheric model run at Fleet Numerical Meteorological and Oceanographic Center. Each model was run twice, with and without the opposing swell as a boundary condition.

Fig. 5.1 illustrates the observed and simulated wave spectra at the position of the center buoy, located on the mid-shelf, and the outer buoy, located furthest away from the coast. The model results obtained with the Wavewatch3 advection scheme and the WAM(cycle-4) source terms, which basically operates in the same way as the WAM(cycle-4) model, are represented by red left-pointing triangles and will be the subject of discussion in the following. Notice how the model, when run without swell, see fig. 5.1a), reproduces the wind-sea very well at the center buoy. Both energy and peak frequency correspond satisfactory between model and observations. When

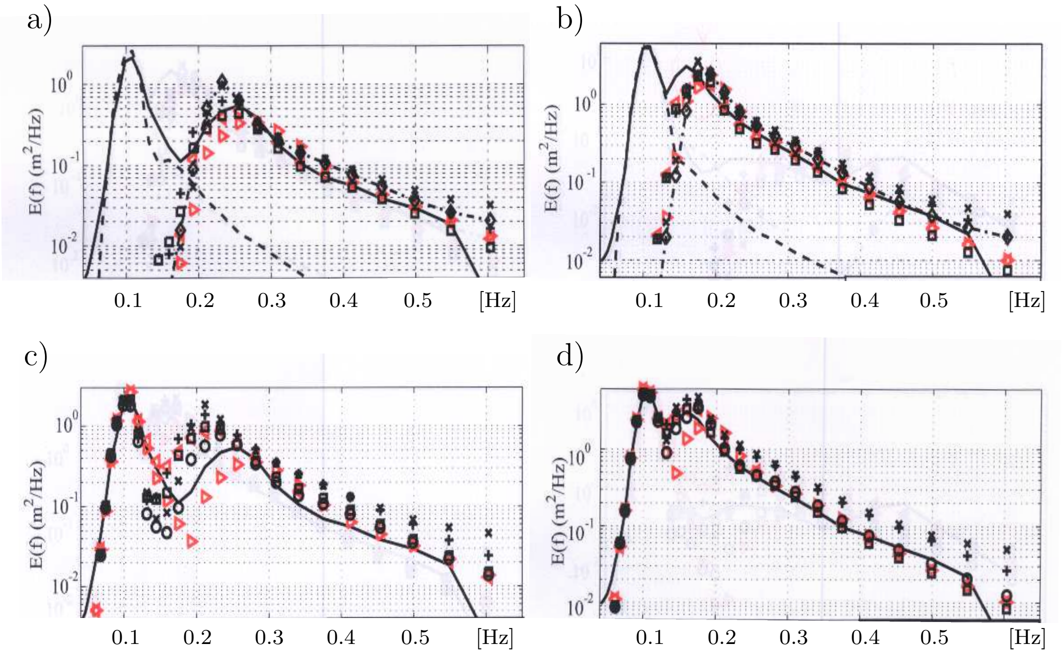

Figure 5.1: *Measured 1D spectra obtained during the SHOWEX-project(solid black line). Wavewatch3 implemented with WAM(cycle-4) source functions(red left-pointing triangles). The spectra represents a 5 hour mean from 12UTC-1700EST the 3rd of November 1999. a) and c) are obtained at the mid-shelf, while b) and d) are taken at the outer-shelf. Simulations are given with and without an opposing swell, relative to the wind, as a boundary condition. Figures are taken from Ardhuin(Sub)*

moving to the outer buoy this situation changes, illustrated by fig. 5.1b). Ardhuin (Sub) proposed that the slight increase in energy and downshifted peak frequency of the measured wind-sea could possibly be explained by the effects imposed by the opposing swell. As the model parametrization does not consider effects of swell, an increase in the drag coefficient will not be accounted for in the simulations. It should be noted that Ardhuin (Sub) also suggested non-stationary winds, as wind gustiness, to be a just as likely cause for the deviation found between model and observations.

Now, when including the opposing swell as a boundary-condition the model overestimates the wind-sea significantly at the mid-shelf, see fig. 5.1c). This effect has no physical interpretation, but clearly indicates deficiencies in the model, which can be explained by a poorly parameterized dissipation-term which is based on the mean wave number $\bar{k}$. In mixed conditions of swell and wind-sea the mean wave number becomes too large, resulting in an intensified wind-sea growth. On the outer-shelf, see fig. 5.1d), the wind-sea is closer to a full development and the deviation is reduced. This behavior of the model is important to the following analysis.

Chapter 6

Data & Method

6.1 Data

The following analysis is based on two severe wave events taking place in the north North Sea -and south Norwegian Sea area. First case is related to the storm "Edda" that hit the coast of Norway the 11th of December 2003. This powerful low pressure system produced significant wave heights exceeding 12m which characterizes a very strong winter storm of this region. Second case of interest, 9-12th of February 2000, did not experience the same wave heights, but peak periods above 22 seconds. Only a combination of steady strong winds working over a long fetch is capable of creating similar conditions. Offshore installations like oil rigs and FPSOs are particularly sensitive to these situations, having maximum response at periods around 25s, making these types of events interesting in an economical and environmental sense. Both cases to be analyzed are documented using WAM-model(cycle-4) simulations obtained from met.no, see section 4.3.3, and MIROS-radar measurements, see chapter 3. In the following, the two events will be referred to as the '2003-case' and '2000-case'.

6.1.1 Positions and radar heading

The radar data were collected at four different locations, which are the positions of the oil rigs, from north to south; Heidrun, Gullfaks C, Troll A and Sleipner A, see fig. 6.1. Corresponding WAM-model data were obtained using the grid point closest to each respective radar. However, as the model only offers simulations at a limited number of grid points, predefined by met.no, the actual nearest grid point does not always contain any output-data. This was solved using the nearest available simulations, see fig. 6.1. Table 6.1 gives the positions of the corresponding measured and modelled data, the deviating distance between the two and the water depth at each oil rig. The deviating distance is calculated using the precise position of the grid point. However, this is modified taking into consideration that the simulated data is a mean measure representing a grid box of 50km and not only a single point. In addition, the shortest

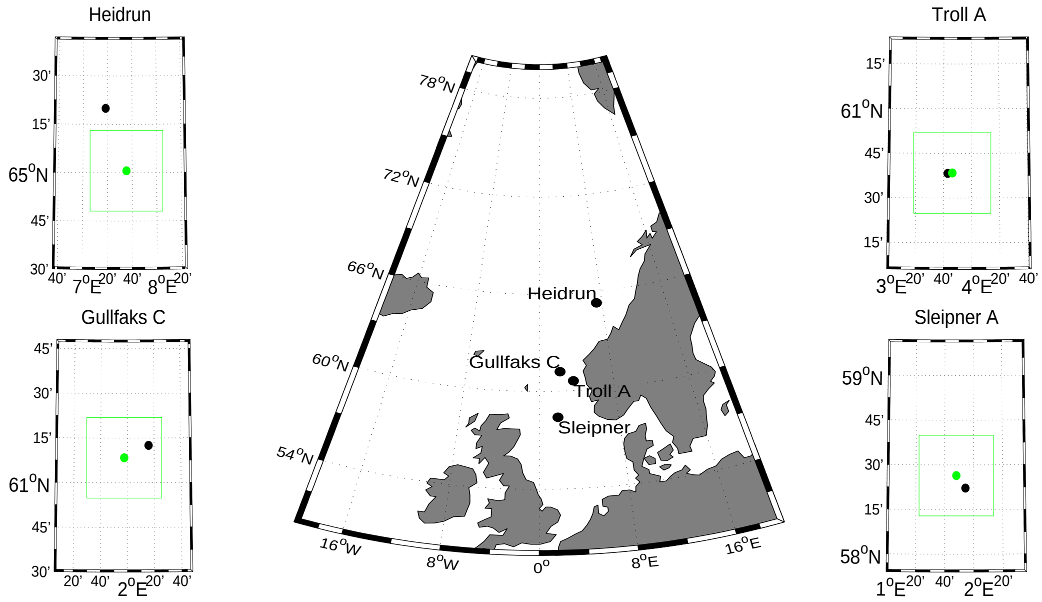

Figure 6.1: *Studied area: MIROS-data are obtained from four different oil rigs in the North - and Norwegian Sea; Heidrun, Gullfaks C, Troll A and Sleipner A, marked in black. In addition, corresponding WAM-model-data are used, seen in green. The model grid box and grid center are illustrated by a square and dot respectively. Grid spacing are 50km. Deviating distance between radar and model grid center are given in table 6.1*

distances separating the oil rigs are given in table 6.2.

Few oil rig constructions are exactly the same, making it unpractical or even impossible to always install a MIROS-radar in the preferred direction. The four radars used in the following analysis have all different headings. Fig. 6.2 illustrates the 180 degrees of free-sight the radar covers at each respective oil rig.

Table 6.1: *Positions of the MIROS-radars and the corresponding WAM-model grid points used in the analysis. In addition, the deviating distance between these two positions and the depth at each site are given.*

Station	Obs. position		Grid position		Dev. dist.	Depth
Heidrun	65°20’12”N	7°18’35”E	65°00’36”N	7°35’24”E	39km	350m
Gullfaks C	61°12’54”N	2°16’26”E	61°08’24”N	1°57’36”E	19km	216m
Troll A	60°38’45”N	3°43’35”E	60°38’24”N	3°46’12”E	2.5km	303m
Sleipner A	58°22’02”N	1°54’31”E	58°26’24”N	1°48’00”E	10km	82m

Table 6.2: *The shortest distance measured between the oil rigs. Numbers are based on the obs. position given in table 6.1 and are given in kilometers.*

Position	Heidrun	Gullfaks C	Troll A	Sleipner A
Heidrun	0	523	552	825
Gullfaks C	523	0	101	318
Troll A	552	101	0	273
Sleipner A	825	318	273	0

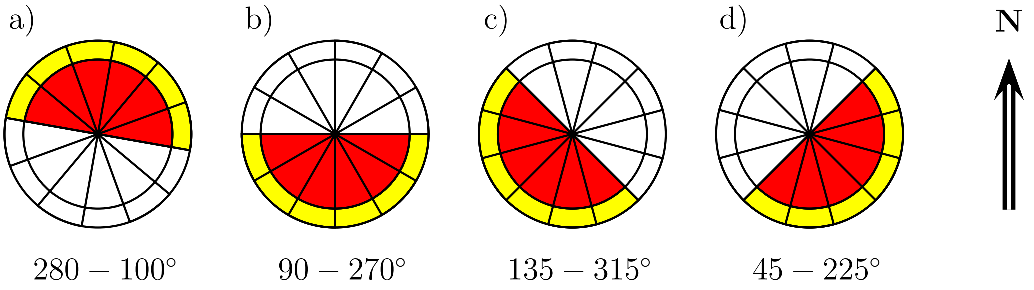

Figure 6.2: *Radar heading: The MIROS-radar scans a 180 degrees sector of open ocean. Red and yellow area represents the free sight sector at a)Heidrun:* 280 – 100°*, b)Gullfaks C:* 90 – 270°*, c)Troll A:* 135 – 315°*, d)Sleipner A:* 45 – 225°

6.1.2 Radar and model documentation

The model and radar results are represented by the 2D wave spectrum. Both cases are documented by almost identical observational MIROS-data, posted every 15 or 20 minutes, depending on the data format(DF005/DF038). The only difference is found in the directional resolution of the spectra obtained at Heidrun, which is 10 degrees for the 2003-case and 30 degrees for the 2000-case. All other positions have a 30 degrees resolution in both cases.

The 2003-case has full WAM-data coverage. That is, both analyzed and prognostic spectra, -12h to +60h, see fig. 4.4, are available every twelve hours, offering all together analyzed spectra every six hours, as each model run calculates spectra for -12h, -6h and 0h. In addition, analyzed and forecasted, +3h to +12h, parametric data(H_s,T_p and TH_p) are available every three hours.

The 2000-case has far poorer model-documentation compared to the 2003-case. Only one model run is available for all four positions and the prognostic data only extend +42h ahead. Opposed to the 2003-case, no parametric data are available.

Neither of the two cases are equally spanned in time by simulations and radar data. The focus of this analysis will be made on the time periods both results are available.

6.1.3 Wind documentation

The MIROS company has its own format covering environmental data, DF022, including wind. Each of the four chosen oil rigs have two or more wind measuring devices located on deck. Most often one is situated at the helideck and the other at the highest point of the oil rig. All measurements are adjusted to 10m above sea level, which is the height of the wind fields used in the WAM-model, and posted every 10 minutes in both cases. It should be noted that the wind conditions at the helideck can be affected by the construction of the oil rig. Some platforms may therefore show significant deviation between the two sensors for certain wind directions.

The winds forcing the wave model, calculated by the HIRLAM-20 atmospheric model, are posted together with the WAM-model results, spectra and parametric data. For the 2003-case, this gives a complete history on the local wind at each grid point. Because the wind is linearly interpolated between every three hours, this offers an exact representation of the wind forcing the model.

Since the 2000-case has model simulations available only every six hours, the wind is known every second time step it forcing the model. The wind can therefore not be linear interpolated in between these points in time, even though this is how the data will be presented. This shortcoming makes it harder to evaluate the quality of the wind driving the model.

In order to get a bigger picture of the wind conditions during each period, synoptic wind fields obtained from NCEP-NCAR reanalysis(http://ingrid.ldeo.columbia.edu/) are presented for each case.

6.2 Method

The focus of this study will be to locate deviations between the radar measurements and model simulations during two severe wave events. Ideally, both approaches had been flawless and no differences would be found. While this is not the case, it is of our interest to address weaknesses in both the model and the radar to ease later improvements.

Because these two approaches of obtaining wave data are based on different assumptions, they may be used to test the importance of processes not jet fully understood. In the following, the effect of swell on the growth rate of wind-sea will be investigated. As the model does not take this mechanism into account, the measurements should show signs of different behavior in these situations if the effect is to be considered significant.

6.2.1 Wind

Emphasis will be made on the measured and simulated local wind. Local wind conditions are not necessarily important for the total wave state, which depends on the larger scale wind fields and wind history, but it can tell something about the quality of the wind forcing the model. Precise wind fields are an absolute crucial condition for optimal model-results.

Now, if the wind fields are wrong the model can not be rejected for predicting false wave conditions. But, if the wind has a satisfactory accuracy and the simulations are off, it might indicate shortcomings in the model. Wether the inaccuracies are due to local considerations, as gust winds, or of a more general physical character, bad parametrization, it needs to be addressed. Luckily the WAM-model has been extensively tested and proven to work well in most conditions. Therefore, if the simulations are based on satisfactory winds, the model may in some contexts be considered a 'true state' and used to test the quality of the MIROS-radar in situations it is thought to be less reliable.

It is not possible to quality check the entire wind field. There are simply not enough observations. And, accurate wind at one grid point does not guarantee accurate winds within the rest of the model area, but it can give an indication. However, in this thesis, the quality of the model results will be based on the quality of the locally simulated wind compared to observations.

As mentioned in the previous section, the measurements can be affected by the platform construction in certain wind directions. This problem is tried solved by always comparing the modelled wind with the sensor, A or B, measuring the highest wind speeds for that particular case. This will vary from platform to platform.

Both wind speed and wind direction time series will be accompanied by scatter plots, corresponding regression lines and correlation coefficients. In addition, a collection of statistical parameters are presented, see appendix A.0.7.

6.2.2 Wave parameters

An obvious foundation for a comparison of the radar and the model should be based on the most frequently used wave parameters. In operational wave forecasting these are H_s, T_p and TH_p, which represent the total wave energy, the dominating wave frequencies and the direction they are coming from. For the majority of users this is often enough information. For the WAM-model and the MIROS's DF005-format these parameters are precalculated. The DF038-format contains only the 2D wave spectrum, demanding the wave parameters to be calculated.

The significant wave height is given by

$$m_0 = \sum_{j=1}^{n=N_\theta} \sum_{i=1}^{n=N_f} E(f,\theta)\Delta f_i \Delta\theta_j \tag{6.1}$$

$$H_s = 4\sqrt{m_0} \tag{6.2}$$

, where N_f and N_θ are the total number of frequency and directional bands respectively.

The peak period is obtained by first finding the 1D frequency spectrum calculated by

$$E(f) = \sum_{j=1}^{n=N_\theta} E(f,\theta)\Delta\theta_j \tag{6.3}$$

The peak frequency is then identified by

$$f_j = arg_{max}(E(f)) \tag{6.4}$$

and weighted over a three point average to avoid any effects of poor resolution in frequency

$$f_p = \frac{f_{j-1}E(f_{j-1}) + f_jE(f_j) + f_{j+1}E(f_{j+1})}{E(f_{j-1}) + E(f_j) + E(f_{j+1})} \tag{6.5}$$

Finally, the peak period is given by the inverse of eq. 6.5.

6.2.3 Integrated spectra

As noted in chapter 3, the 2D wave spectrum of the DF005-format spans the frequency interval 0-0.313Hz. However, wind generated waves are nonexisting on frequencies lower than 0.03Hz. This is why all wave energy in the preceding analysis is calculated using the same frequency interval for the DF005 as the DF038-format, 0.0313-0.3125Hz. This also corresponds to the interval used by the MIROS's signal processing unit when precalculating wave parameters given in the DF005 format.

The MIROS-radar and the WAM-model span a different range of frequencies, 0.0313-0.3125Hz and 0.042-0.4137Hz respectively, see fig. 3.5 and 4.2. However, this will not significantly effect the total amount of energy represented by the two methods. The majority of energy is always going to be well in between both of these frequency intervals.

It is of interest to investigate how the radar and the model differ when comparing defined frequency intervals. In this analysis we separate the energy content below and above 0.094Hz. The limit is set at this frequency to separate the long and short period wave components. The summation is expressed by eq. 6.1, but with limits adjusted to the two intervals. Because the MIROS-radar and the WAM-model do not use the same resolution in frequency, the summation is not taken over the exact same interval. The limit is set at 0.0938Hz for the radar and 0.0942Hz for the model. However, a frequency interval differing 0.0004Hz will barely affect the results and are therefore not taken into consideration.

The physical shape of the radar is constructed to scan 180 degrees of open ocean, see chapter 3 and fig. 6.2. Because the radar has the ability to detect approaching as well as receding waves, this should not affect the accuracy of the 2D spectra. However, one directional-frequency bin can only represent approaching or receding waves by posting positive or negative values, but not both at the same time. There may be situations when two distant wind fields have produced waves propagating in the opposite direction of each other. When both systems are present at the same time, the MIROS-radar is not capable of representing both systems as long as they have energy on the same frequencies. To test the effect of this shortcoming, the directional frequency spectra obtained by the radar will be integrated over two 180 degrees sectors covering approaching and receding waves, see fig. 6.2. The same integration is carried through with the corresponding model spectra for comparison. The emphasis will be made on the shorter time periods where two wave systems with 180 degrees ambiguity are present.

6.2.4 Wave spectra

The best way of getting a clear picture of the overall wave condition at a fix point, is made studying the 2D spectrum. It offers a quick overview of the wave energy content at the sea surface, wether there are swell present or not, what direction the majority of energy is coming from, peak period and so on.

The two different approaches of obtaining wave data make it of importance to search for repeating deviation. However, the radar and model have different resolutions in direction and frequency and the model calculates idealized spectra of the JONSWAP. Seeing past this obvious distinction, the spectra are still a subject for discussion.

MIROS's DF005-format is represented by a wave spectrum covering 180 degrees. Each directional-frequency bin is either represented by a positive or a negative value. The negative values have a 180 degrees ambiguity. Fig. 6.3a) shows the absolute value of the 2D spectrum, while fig. 6.3b) illustrates the adjusted spectrum where the 180 degrees ambiguity has been taken into consideration. All DF005 spectra of the following analysis are presented using this adjustment.

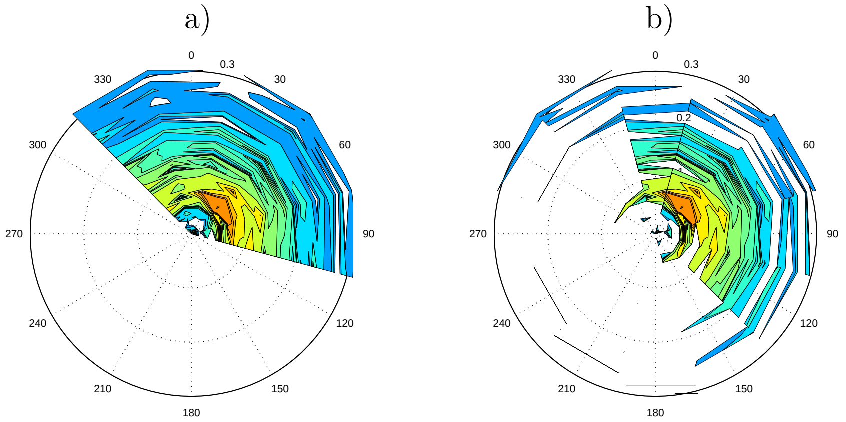

Figure 6.3: *a)The absolute value of the original MIROS's DF-005 spectrum. b)The same spectrum adjusted to the 180 degree ambiguity*

The 2D spectra are represented using the oceanographic convention. Energy is 'going to' the direction indicated. This means that energy plotted in the north are actually coming from the south. However, when discussed, a wave system coming from the south will be referred to as a S wave system.

Here, only a selection of situations will be studied, primarily at times when the spectrum obtained by the model and radar differ the most. All 2D spectra are complemented by measured and modelled wind arrows and their scalar value. In addition, the 1D frequency spectrum is presented.

All time series are marked with letters representing moments in time where the corresponding wave spectrum will be illustrated and discussed. For convenience, these spectra have also been marked with the same letters. If not noted otherwise, the simulated data of the 2003-case are deduced from analyzed wind fields. For the 2000-case, all data are used. Based on the different amounts of available model simulations, the best documented case will be analyzed first.

Chapter 7

Results: Model vs Radar

7.1 10-16th of December 2003

7.1.1 Wind conditions

Synoptic scale

Within a week of December 2003 the mid and northern part of Norway got exposed to severe weather conditions as three subsequent low pressure systems moved east into Norwegian waters. Winds in the *violent storm* range (28.5-32.6m/s) and gust winds reaching *hurricane* force (>32.7m/s) generated *phenomenal* wave conditions($H_s > 11.5m$). The last storm in the sequence, named the "Edda", is evident in fig. 7.1a), 7.2b) and 7.2c). Fig. 7.2a) and 7.2b) illustrate the birth of the low pressure system NE of Iceland and its track across the Norwegian Sea, finally dying out the 12th in the Barents Sea area, see fig. 7.1d).

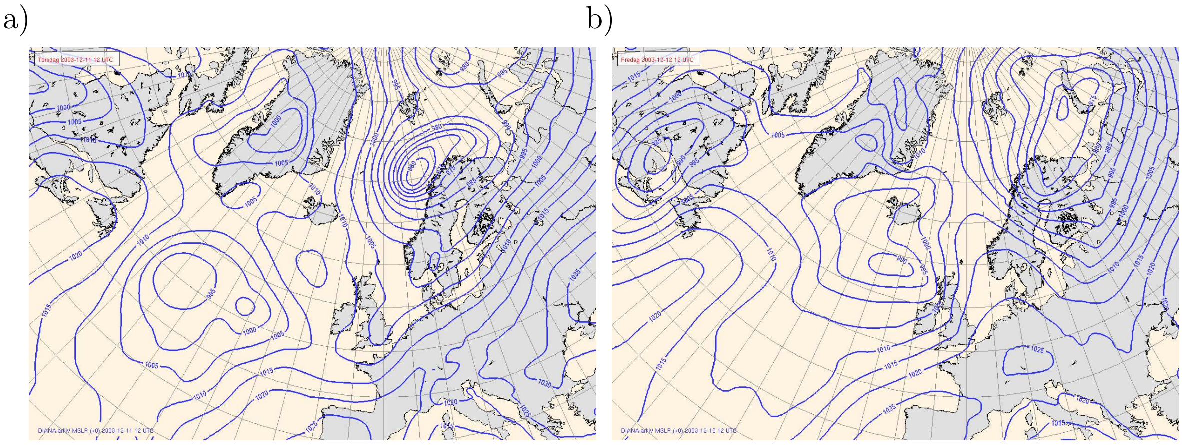

Figure 7.1: *Analyzed sea level pressure for the northern Atlantic at 12UTC the a)11th and b)12th of December 2003. Data are obtained from the atmospheric model HIRLAM-20 (met.no).*

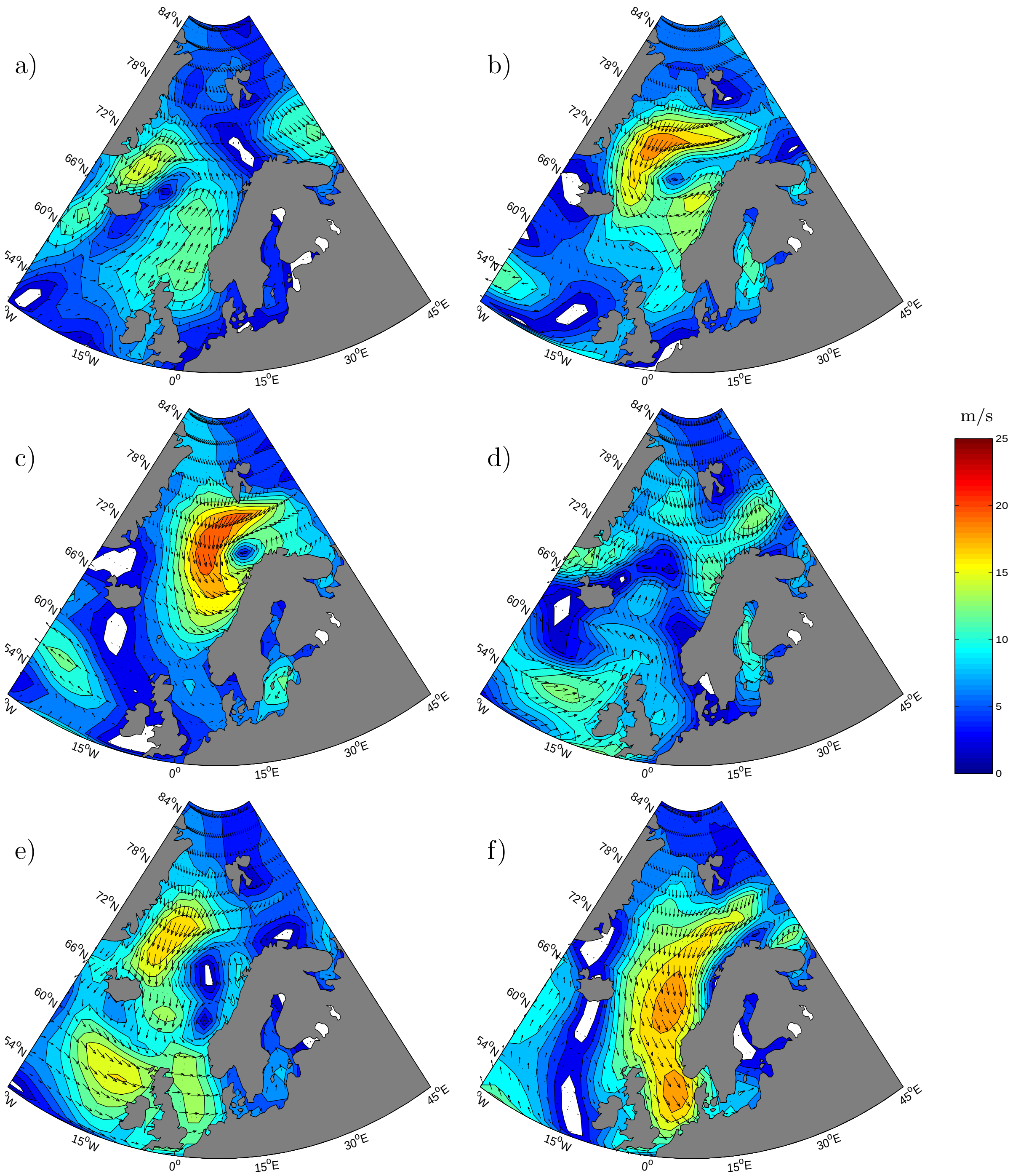

Figure 7.2: *Analyzed sea surface winds(10m) for the northern Atlantic at 12UTC the a)9th - f)14th of December 2003. Data are obtained from NCEP-NCAR(http://ingrid.ldeo.columbia.edu/).*

The "Edda" and the associated wind conditions at the time created an interesting, but not at all unique situation. As the "Edda" was accompanied by strong N winds on the west side of the low pressure center, see fig. 7.1a) and 7.2c), a weaker low pressure system NW of Great Britain produced S winds further south, see fig. 7.1b) and 7.2d). In that way, N swell, propagating south, was met by opposing S winds in the North Sea and the southern Norwegian Sea.

The time series documenting the wind and wave conditions during "Edda" have been extended to the 16th of Dec., as the later period saw a new low pressure system producing strong N winds. However, this time the strongest winds were found further south, closer to the four chosen positions of observation, see fig. 7.2f).

Because of different geographical positioning, the results obtained at the Heidrun platform will be analyzed separately from Gullfaks C, Troll A and Sleipner A. This is done because the wave conditions of the three latter platforms were affected much by the same winds within this period.

Local scale

Heidrun

The two wind speed measurements obtained at Heidrun, indicated by the red and black line in fig. 7.3a), show at times large deviation. The HIRLAM-20 winds, seen in green, are compared to the measurements having the best fit to the model, which is the strongest measured wind. Opposed to the wind speed, the simulated and measured wind direction, see fig. 7.3b), are very well correlated throughout the period.

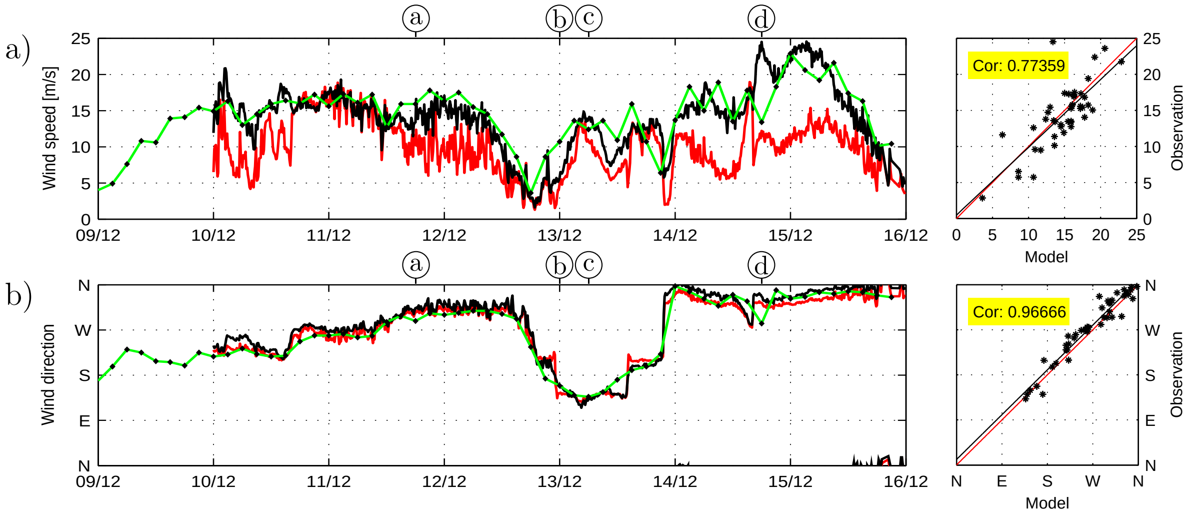

Figure 7.3: *Wind speed and wind direction with corresponding scatter plots for the period 9th - 16th of December 2003. Observations: sensor A(red line) and sensor B(black line). Model: HIRLAM(green line). Scatter plots are based on the data of the sensor with best fit to the model. a),b): Heidrun.*

Because the Heidrun platform was located more south than the "Edda" it did not experience the same wind speeds as found further north. From 00UTC the 10th until noon the 12th average winds were of *near gale* force(13.9-17.1m/s) with shorter periods of *gale* force(17.2-20.7m/s).

The time period from 18UTC the 12th until 18UTC the 13th saw SE-SW winds following a longer period of NW winds, see fig 7.3a). This confirm the large scale synoptic observations mentioned above and correspond to the period of swell/wind-sea interaction. The wind speed of this period is therefore of importance for the later discussion. Notice how the average HIRLAM-20 winds are stronger than the measurements within this period, with an exception found around 6UTC the 13th.

Fig. 7.3a) illustrates the scatter between the measured and modelled wind speed covering the whole time series. Correlation is calculated to a poor 0.77. However, acknowledge the deviation in wind speed at 18UTC the 14th. Because the correlation is calculated using few data, an outlier will affect the coefficient significantly.

Gullfaks C, Troll A and Sleipner A

The measured and simulated winds obtained at the three subsequent oil rigs are presented in fig. 7.4. On average the data show good correlations illustrated by the corresponding scatter plots. Only during smaller time periods, like 12UTC the 11th, significant deviations are more evident.

Like Heidrun, the main focus will be made on the period where the wind had backed approximately 180 degrees and was opposing the N swell. This is seen from 12UTC the 12th and 24 hours ahead on Gullfaks C and Troll A, with Sleipner A having similar conditions from 9UTC the 12th until the 13th. The correlation in wind speed is satisfactory for all three platforms within these time periods, with the exception of a short period around the 13th at Gullfaks C.

7.1.2 Wave parameters: H_s & T_p

Heidrun

The measured and simulated significant wave height, H_s, and peak period, T_p, for Heidrun, are illustrated in fig. 7.5.

Within the time period of SE-SW winds, no abnormal deviations between the simulated and measured H_s are found. The fit is rather better than worse compared to the time periods prior to and after. However, around midday the 13th there are obvious deviations in T_p, illustrated in fig. 7.5b). While the model indicates the peak period to be 11.5s the measurements are closer to 7s. Such a striking difference in T_p most often indicates the presence of two wave systems at the same time. The difference in maximum energy level of each respective wave system may be very small, but enough to distinguish a peak period. Both approaches, model and radar, represent the peak most energetic according to their calculations. Interestingly, the model indicates the swell to be the most energetic system, while the measurements indicate the wind-sea to be more energetic. However, the difference is small, as the measurement also indicates

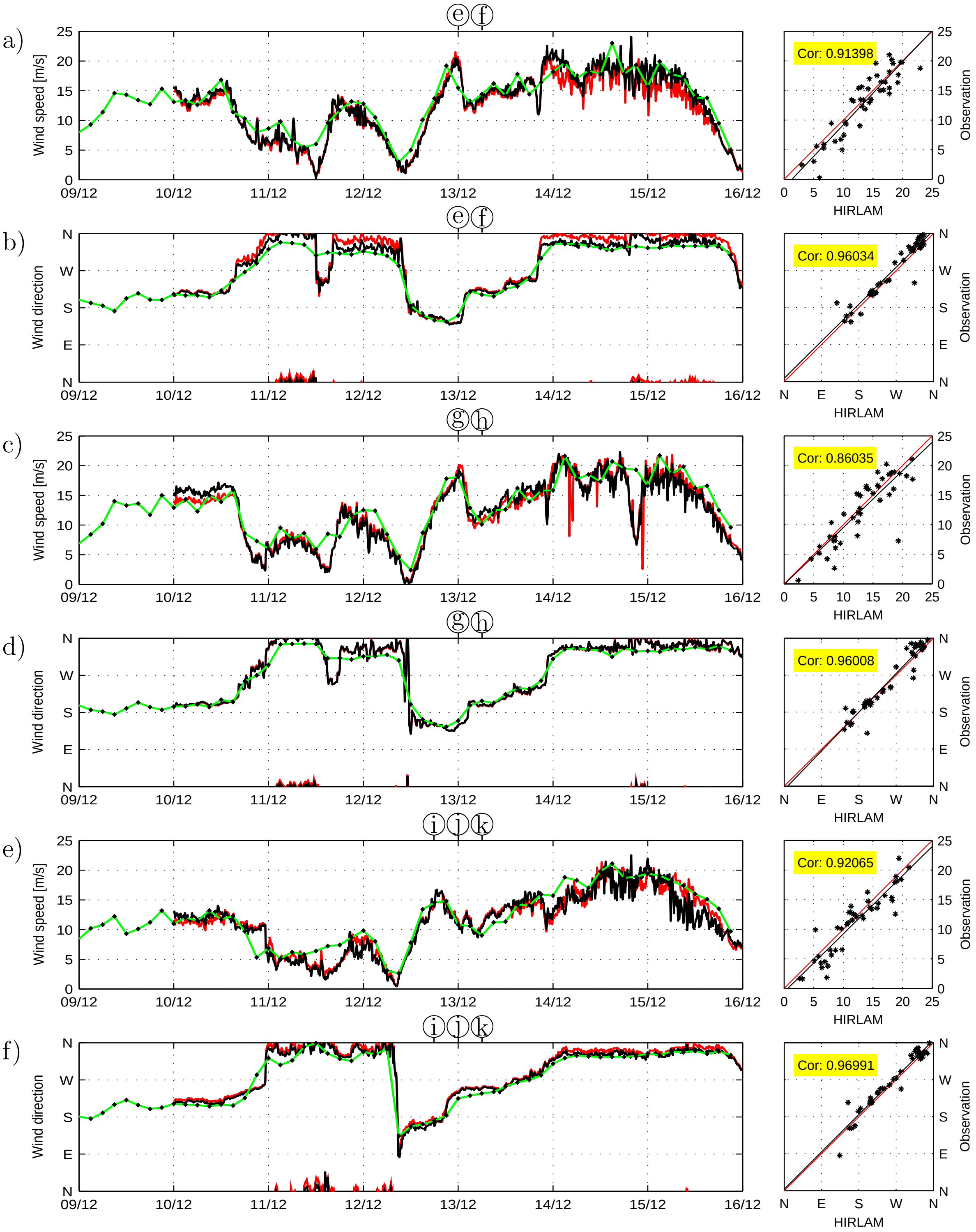

Figure 7.4: *Wind speed and wind direction with corresponding scatter plots for the period 9th - 16th of December 2003. Observations: sensor A(red line) and sensor B(black line). Model: HIRLAM(green line). Scatter plots are based on the data of the sensor with best fit to the model. a),b): Gullfaks C; c),d): Troll A; e),f): Sleipner A.*

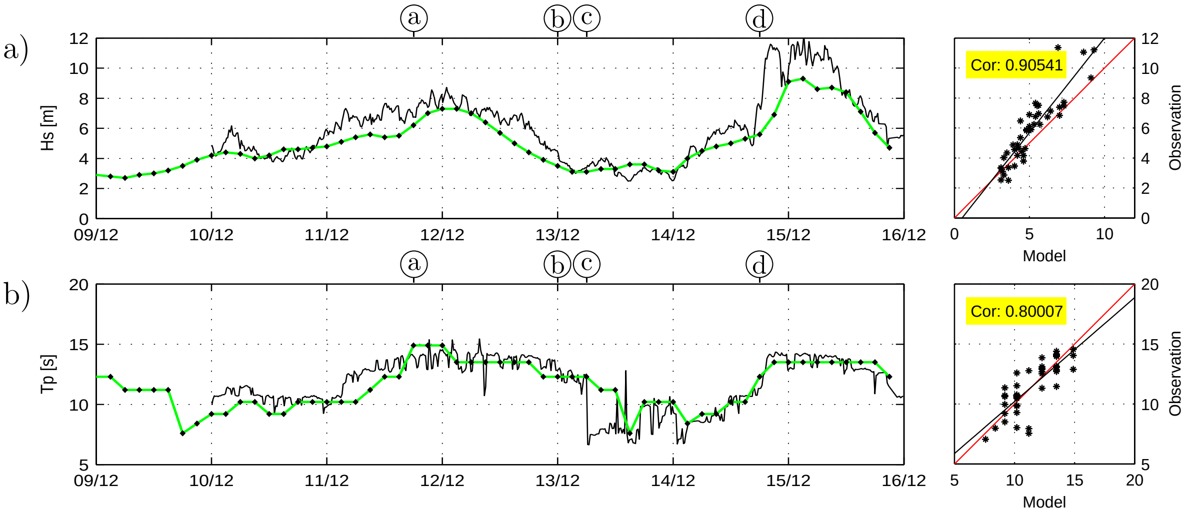

Figure 7.5: *Significant wave height, H_s, and peak period, T_p , with corresponding scatter plots for the period 9th - 16th of December 2003. Observations: MIROS-radar(black line). Model: WAM(green line). a),b): Heidrun.*

the peak period to be controlled by the swell around 12UTC the 13th, represented by the spike in fig. 7.5b).

Last part of the time series is dominated by large deviations in H_s, peaking around 21UTC the 14th, where the model simulates H_s to be 7m and the measurement is closer to 12m. Notice that this period coincides with the rather large misrepresentation in the simulated local wind speed at the time, see fig. 7.3a).

H_s and T_p are summarized by scatter plots in fig. 7.5. H_s has an 0.91 correlation coefficient, however the regression line indicates the model to systematically underestimate the significant wave height. T_p shows a larger scatter and a weaker correlation of 0.80, affected by the presence of two equally energetic wave systems, explained above.

Gullfaks C, Troll A and Sleipner A

The significant wave height and peak period data for Gullfaks C, Troll A and Sleipner A are illustrated in fig. 7.6. The most prominent deviations in H_s are located at Troll A around 09UTC the 12th, see fig. 7.6c), and Sleipner A around 03UTC the 14th, see fig. 7.6e). In both cases the difference between the model and radar is approximately 2m, however, of opposite signs. Otherwise, the comparisons of T_p show the model to be low at all oil rigs the last part of the time series.

Within the period of N swell propagating against the wind, no significant deviations in H_s are detected at any of the three stations. More interesting is the behavior of the measured and simulated T_p. At Gullfaks C both approaches indicate the peak period to be dominated by the wind-sea, seen by the sudden coinciding drop in T_p around the 13th. At Troll A the measured T_p is clearly more fluctuating, representing both swell and wind-sea, while the model indicates T_p to be controlled only by the wind-sea.

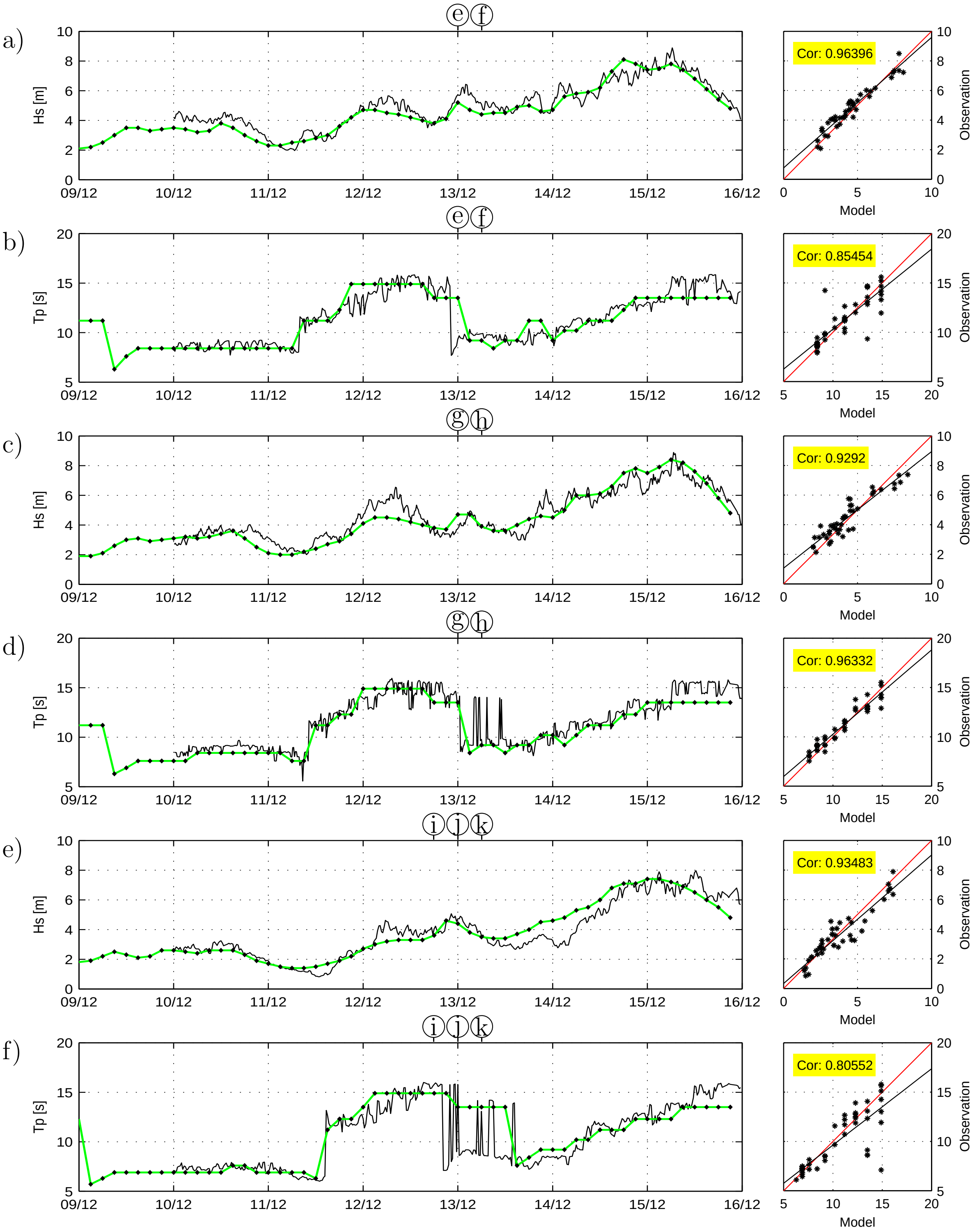

Figure 7.6: *Significant wave height, H_s, and peak period, T_p , with corresponding scatter plots for the period 9th - 16th of December 2003. Observations: MIROS-radar(black line). Model: WAM(green line). a),b): Gullfaks C; c),d): Troll A; e),f): Sleipner A.*

At Sleipner A the measured T_p shows similar behavior found at Troll A, but here the simulated T_p is dominated by the swell.

Summary statistics for the simulated and measured H_s, T_p and U_{10} are presented in table 7.1. The parameters used for the statistical comparison are all defined in appendix A.0.7. The biases are with respect to observations. The model data are, as mentioned, based on analyzed wind fields. However, the same comparison has been carried through using simulations based on prognostic wind fields, +3h to +12h. These results are summarized in tab. 7.2. In both cases individual and total statistics are given.

Table 7.1: *Summary statistics of significant wave height H_s, peak period T_p and wind speed U_{10}, based on analyzed wind fields for the time period 9-16th of December 2003. The bias is with respect to measurements. SI is scatter index, RMS is root-mean-square error and Corr is correlation. Number of entries are given in parentheses.*

	$H_s[m]$				$T_p[s]$				$U_{10}[m/s]$(scalar)			
Position (entries)	Bias	RMS	SI	Corr	Bias	RMS	SI	Corr	Bias	RMS	SI	Corr
Heidrun(43)	-0.71	1.25	0.22	0.91	-0.01	1.26	0.11	0.80	0.42	2.85	0.20	0.77
Gullfaks C(43)	-0.23	0.48	0.10	0.96	-0.09	1.28	0.11	0.85	0.59	2.29	0.18	0.91
Troll A(43)	-0.15	0.65	0.15	0.93	-0.13	0.71	0.06	0.96	0.62	2.80	0.22	0.86
Sleipner A(43)	0.16	0.65	0.18	0.94	0.52	1.92	0.19	0.81	0.83	2.22	0.20	0.92
Total(172)	-0.23	0.81	0.18	0.91	0.07	1.36	0.12	0.85	0.61	2.56	0.20	0.88

It is worth noticing the increased bias in total wind speed comparing the analyzed and prognostic statistics. The stronger local wind forcing found in the prognosis is reflected in the reduced bias of the forecasted H_s. A slight improvement may also be spotted in T_p.

Table 7.2: *Summary statistics of significant wave height H_s, peak period T_p and wind speed U_{10}, based on prognostic wind fields, +3h - +12h, for the time period 9-16th of December 2003. The bias is with respect to measurements. SI is scatter index, RMS is root-mean-square error and Corr is correlation. Number of entries are given in parentheses.*

	$H_s[m]$				$T_p[s]$				$U_{10}[m/s]$(scalar)			
Position (entries)	Bias	RMS	SI	Corr	Bias	RMS	SI	Corr	Bias	RMS	SI	Corr
Heidrun(43)	-0.54	1.16	0.20	0.90	-0.19	1.11	0.10	0.85	1.02	3.11	0.22	0.76
Gullfaks C(43)	-0.05	0.52	0.11	0.96	-0.21	1.10	0.10	0.90	1.42	2.50	0.19	0.93
Troll A(43)	0.09	0.82	0.19	0.91	-0.09	0.66	0.06	0.97	1.77	3.15	0.25	0.88
Sleipner A(43)	0.24	0.69	0.19	0.94	0.30	1.61	0.16	0.86	1.24	2.14	0.19	0.94
Total(172)	-0.07	0.83	0.18	0.90	-0.05	1.17	0.11	0.89	1.36	2.76	0.22	0.89

Fig. 7.7 illustrates the evolution of bias and rms for H_s and U_{10} as a function of forecast hour. Acknowledge that the correspondence between U_{10} and H_s is dispropor-

tional for bias and rms within certain prognostic hours. E.g. from +12 to +30h the bias in U_{10} is decreasing, while the bias in H_s is increasing.

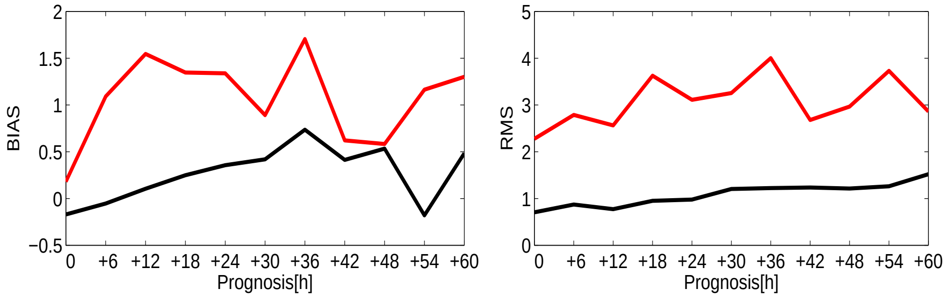

Figure 7.7: *Bias and RMS for wind speed (red line, [m/s]) and for significant wave height (black line, [m]) for different forecast periods. Bias is with respect to measurements. Statistics are based on a five day period, 10-15th of December 2003. Number of comparisons per forecast period, 0 - +60h, are 44, 44, 40, 37, 36, 36, 32, 32, 28, 24 and 20 respectively.*

7.1.3 Integrated spectra: $H_{s,eq}$

High and Low frequencies

Heidrun

Fig. 7.8 illustrates the energy content contained by frequencies below and above 0.094Hz at Heidrun, represented by the equivalent significant wave height, $H_{s,eq}$. Out of the two time series, the most prominent deviations are found in the low frequency part, particulary at the beginning and the end of the time series.

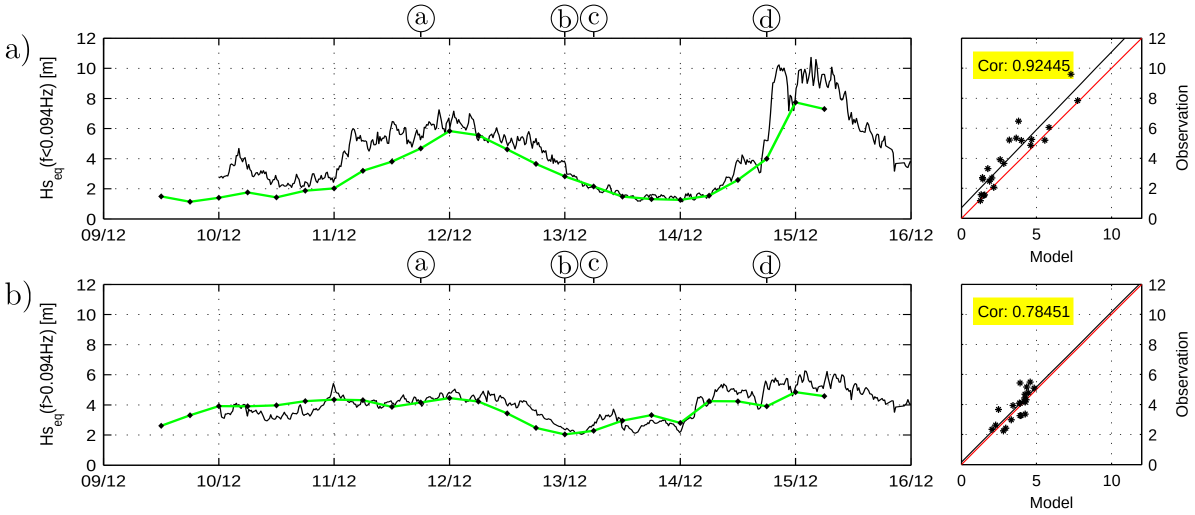

Figure 7.8: *$H_{s,eq}$, deduced from the energy content below and above 0.094Hz, with corresponding scatter plots for the period 9th - 16th of December 2003. Observations: MIROS-radar(black line). Model: WAM(green line). a),b): Heidrun.*

In respect to the 24 hour period SE-SW winds were opposing the N swell, starting 18UTC the 12th, the energy content of both the low and high frequency part show no signs of being affected by the mixed swell/wind-sea condition.

Now, focusing on the scatter plots of fig. 7.8, it is evident that the model underestimates $H_{s,eq}$ on low frequencies compared to the measurements. Even with a weak correlation coefficient for the high frequency part, equal to 0.78 , the regression line supports the idea of higher model performance within this part of the spectrum.

Gullfaks C, Troll A and Sleipner A

For the three southernmost oil rigs, the high and low frequency separation is illustrated in fig. 7.9. In general, the six corresponding scatter plots show that for each oil rig the correlation coefficients are higher for the low frequency part of the spectra compared to the high frequency part.

The most prominent deviations found in H_s, pointed out in section 7.1.2, are naturally reflected in $H_{s,eq}$ as well. While the mismatch in H_s at Troll A around 09UTC the 12th is only visible on low frequencies, see fig. 7.9c), the deviation in H_s at Sleipner A around 03UTC the 14th is mostly evident in the high frequency part, but also on low frequencies, see fig. 7.9e) and f).

Despite the different behavior in H_s comparing Heidrun and the three other oil rigs, there is a high similarity between the low frequency $H_{s,eq}$ of fig. 7.9 and fig. 7.8.

The period of N swell and opposing SE-SW winds does not seem to give any significant effects in any of the two parts of the spectrum. All oil rigs are showing good correlations within these periods.

Directional sectors

Heidrun

Fig. 7.10 illustrates $H_{s,eq}$ deduced from the radar-sectors covering receding, $280° - 100°$, and approaching, $100° - 280°$, wave energy at the Heidrun oil rig. Notice the much improved correlation between the model and radar for the approaching sector compared to the original H_s time series seen in fig. 7.5a). For the receding sector large deviations between the model and measurements are particulary evident around the 12th and 15th. However, it should be acknowledge that the deviation is not caused by the lack of energy in the radar, but an underestimation by the model.

The results are best summarized comparing the scatter plots of fig. 7.11a) and b). With correlation coefficients equal to 0.38 and 0.96 respectively, the model performs better simulating waves coming from the north, i.e. approaching wave energy relative to the radar.

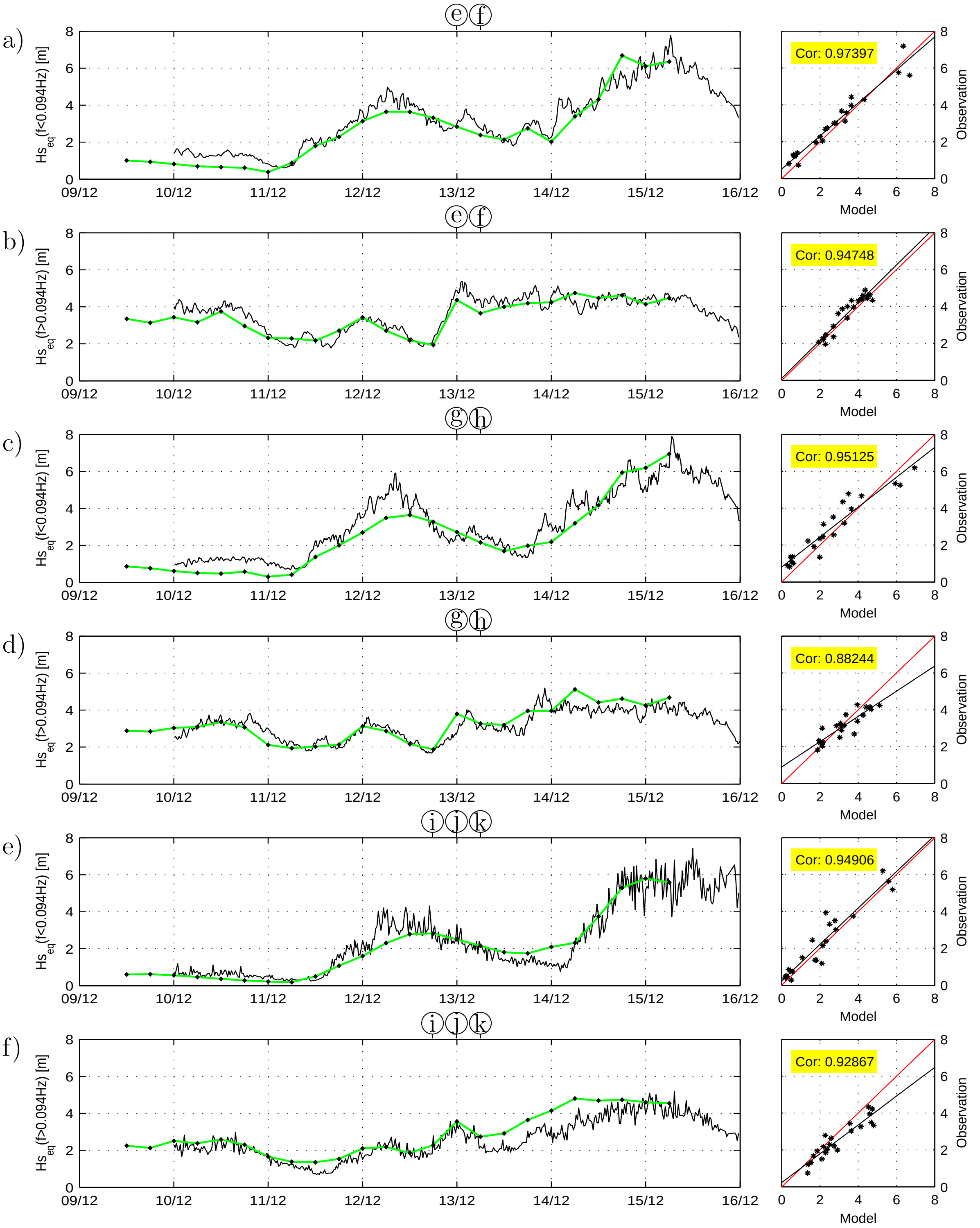

Figure 7.9: *$H_{s,eq}$, deduced from the energy content below and above 0.094Hz, with corresponding scatter plots for the period 9th - 16th of December 2003. Observations: MIROS-radar(black line). Model: WAM(green line). a),b): Gullfaks C; c),d): Troll A; e),f): Sleipner A.*

Gullfaks C, Troll A and Sleipner A

$H_{s,eq}$, deduced from the approaching and receding sectors at the three southernmost platforms, are illustrated in fig. 7.11. Compared to Heidrun the results show the

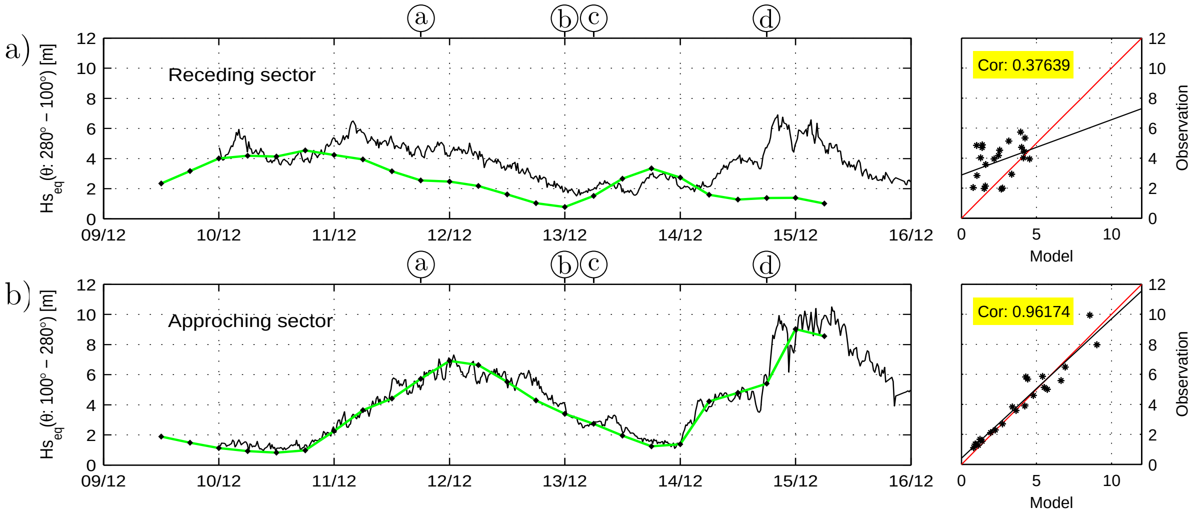

Figure 7.10: *$H_{s,eq}$, deduced from the wave energy receding and approaching the 180 degrees sector the MIROS-radar illuminates at each respective oil rig, with corresponding scatter plots for the period 9th - 16th of December 2003. Observations: MIROS-radar(black line). Model: WAM(green line). a),b): Heidrun*

opposite trend, with correlations improved for the receding sectors.

Notice that all three stations have a mean radar-heading pointing southward, see fig. 6.2. However, in this period a significant amount of energy was coming from the north, generated by the northern situated low pressure systems.

Table 7.11 offers a summary statistics for the comparison between model and measurements based on wave energy on high and low frequencies and two 180° sectors covering approaching and receding energy relative to the radar-heading at each oil rig. The calculations are represented for each respective oil rig and the total number of entries.

Table 7.3: *Summary statistics for $H_{s,eg}$, WAM-model vs MIROS-radar, deduced from wave energy receding/approching the 180 degrees sector of the radar at each respective oil rig and energy above/below 0.094Hz in the time period 9-16th December 2003. The bias is with respect to measurements. SI is scatter index and Corr is correlation. Number of entries are given in parentheses.*

	$H_{s,eq}$ (receding)				$H_{s,eq}$ (approaching)				$H_{s,eq}$ (f<0.094Hz)				$H_{s,eq}$ (f>0.094Hz)			
Pos(entries)	Bias	RMS	SI	Corr	Bias	RMS	SI	Corr	Bias	RMS	SI	Corr	Bias	RMS	SI	Corr
Heidrun(22)	-1.27	1.85	0.48	0.38	-0.13	0.68	0.17	0.96	-0.83	1.17	0.29	0.92	-0.16	0.63	0.16	0.78
Gullfaks C(22)	-0.03	0.48	0.13	0.98	-0.60	0.74	0.27	0.94	-0.24	0.48	0.16	0.97	-0.19	0.36	0.10	0.95
Troll A(22)	-0.17	0.63	0.21	0.97	-0.26	0.58	0.18	0.86	-0.32	0.69	0.24	0.95	0.13	0.48	0.15	0.88
Sleipner A(22)	0.28	0.70	0.23	0.95	-0.63	0.90	0.49	0.72	-0.21	0.59	0.26	0.95	0.41	0.60	0.24	0.93
Total(88)	-0.30	1.06	0.32	0.85	-0.40	0.73	0.25	0.94	-0.40	0.78	0.25	0.94	0.05	0.53	0.16	0.87

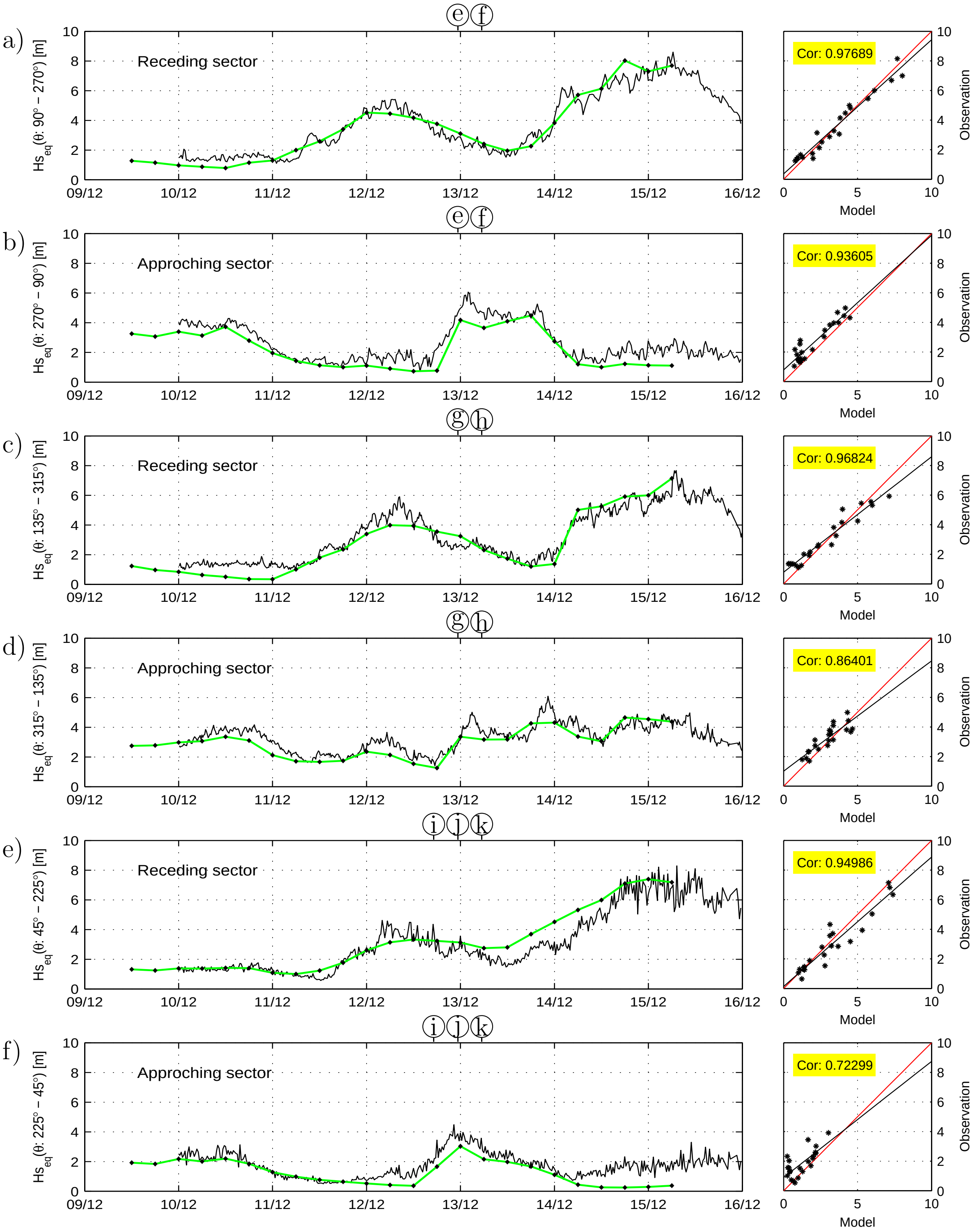

Figure 7.11: *$H_{s,eq}$, deduced from the wave energy receding and approaching the 180 degrees sector the MIROS-radar illuminates at each respective oil rig, with corresponding scatter plots for the period 9th - 16th of December 2003. Observations: MIROS-radar(black line). Model: WAM(green line). a),b): Gullfaks C; c),d): Troll A; e),f): Sleipner A.*

7.1.4 Wave spectra: 1D & 2D

Heidrun

ⓐ: Fig. 7.12, portraying the wave condition at Heidrun at noon the 11th, represents a typical relation between the simulated and measured 1D spectrum in the time period spanned by the 2003-case. On average the measured 1D spectrum has a more enhanced peak compared to the corresponding simulations. Notice how the peak frequency is much the same, but how the measured peak is more than twice as energetic as the simulated peak. In more than 80% of all cases both spectra are available, this is the trend found at Heidrun. However, when focusing on the color coding of the 2D spectra, the simulated peak, going towards the SSE (150°), is seen exceeding the energy level of the measured peak. This seemingly contradiction can be explained by the different spreading characteristics of the two approaches.

ⓐ

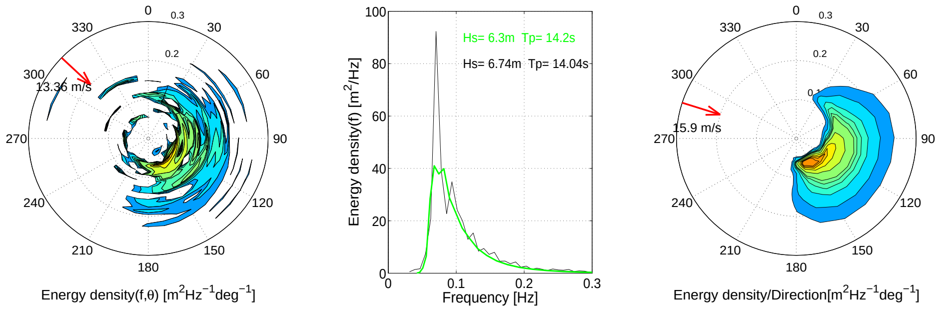

Figure 7.12: *Heidrun: 18UTC 11. Dec. 2003. Left: 2D spectrum(MIROS-radar) and measured wind. Middle: 1D spectra with corresponding* H_s *and* T_p*, MIROS-radar(black) and WAM(green). Right: 2D spectrum(WAM) and modelled wind(HIRLAM).*

ⓑ,ⓒ: At 00UTC the 13th the wind had turned SE and was picking up in strength at Heidrun, see fig. 7.3a) and b). Fig. 7.13a) illustrates the simulated and measured 1D and 2D spectra at the time. At this stage the wind is blowing in the opposite direction of the N swell, but neither the model nor the radar spectrum indicates any wind-sea. Six hours later, at 06UTC the 13th, the measured 1D spectrum has a clear two modal shape, while the simulation barely indicates any wind-sea, see fig. 7.13b). However, the representation of the swell, indicated by the low frequency peak, shows good correspondence between the model and radar. Prior to this point in time the local wind speed is low, but increasing. On average the simulated winds are found stronger than the measurements, see fig. 7.3a). Even though the spectra are substantially different the deviation in total energy is only fractional, separating less than 0.3m in H_s.

ⓓ: At 21UTC the 14th the measured H_s exceeds the corresponding simulation by approximately 5m, see 7.5a). Fig. 7.14 illustrates the wave spectra obtained three

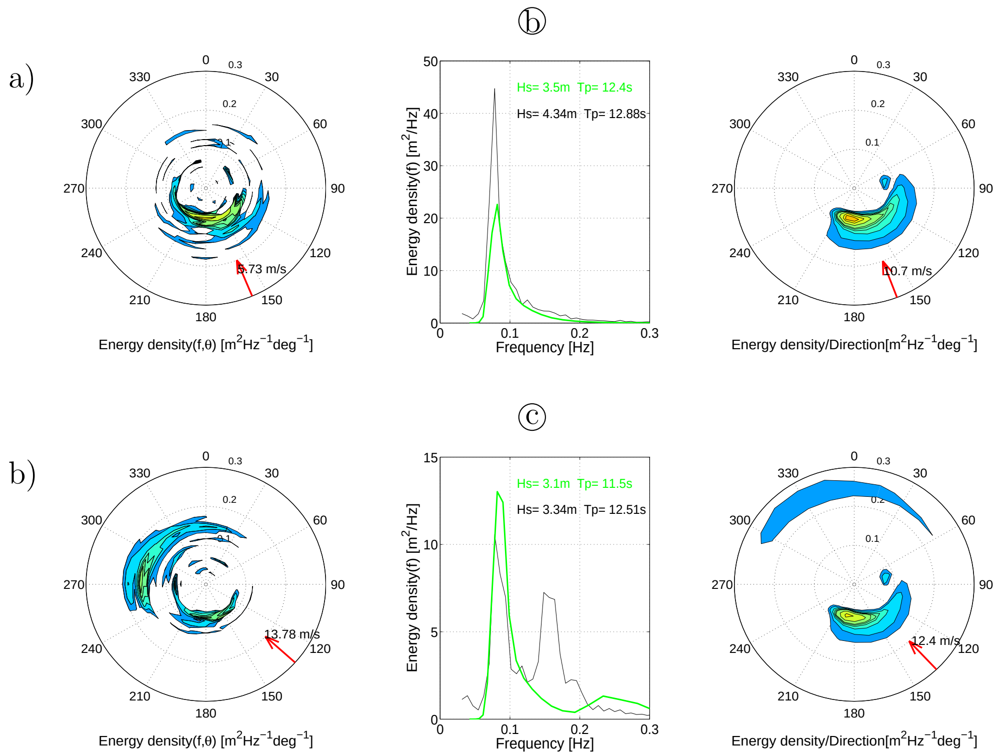

Figure 7.13: *Heidrun: a) 00UTC and b) 06UTC 13. Dec. 2003. Left: 2D spectrum(MIROS-radar) and measured wind. Middle: 1D spectra with corresponding H_s and T_p, MIROS-radar(black) and WAM(green). Right: 2D spectrum(WAM) and modelled wind(HIRLAM).*

hours earlier. Already at this point a clear distinction in energy can be made. Notice the wider 1D spectrum of the measurements. And, once again the radar measurement is having a more enhanced peak compared the model.

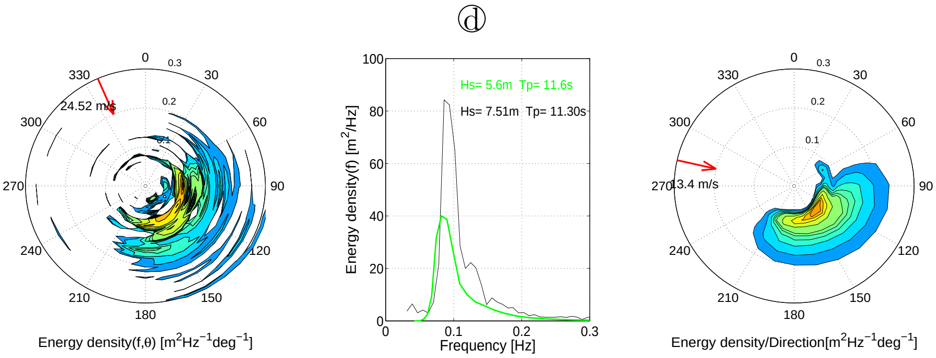

Figure 7.14: *Heidrun: 18UTC 14. Dec. 2003. Left: 2D spectrum(MIROS-radar) and measured wind. Middle: 1D spectra with corresponding H_s and T_p, MIROS-radar(black) and WAM(green). Right: 2D spectrum(WAM) and modelled wind(HIRLAM).*

Gullfaks C, Troll A and Sleipner A

ⓔ,ⓕ: Because the growing wind-sea was generated be S winds, Gullfaks C had conditions of wind-sea opposing the N swell earlier than Heidrun. Fig. 7.15a) and b) show the spectra obtained at 00UTC and 06UTC the 13th. Again the model represents a less evolved wind-sea compared to the radar. This difference is especially pronounced at 06UTC, see fig. 7.15b). However, prior to this point in time, the wind forcing the model is some what weak compared to the measured wind, which may have influenced the results slightly, see fig. 7.4a).

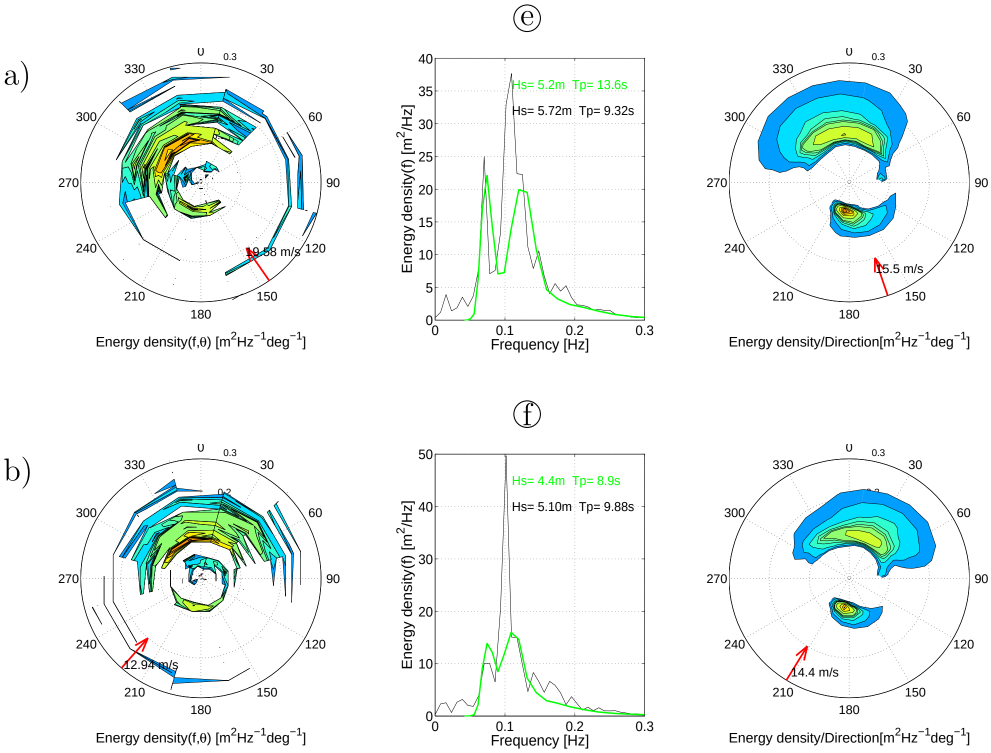

Figure 7.15: *Gullfaks C: a) 00UTC and b) 06UTC 13. Dec. 2003. Left: 2D spectrum(MIROS-radar) and measured wind. Middle: 1D spectra with corresponding H_s and T_p, MIROS-radar(black) and WAM(green). Right: 2D spectrum(WAM) and modelled wind(HIRLAM).*

The Gullfaks C and Troll A oil rigs are closely situated, see fig. 6.1 and table 6.2, and should have close to similar wave conditions at any time. In case of model simulations, this is more or less obvious as all calculations are closely connected, preventing any large differences between any adjacent grid points. The radars are on the other hand operating independently, making them more subjected to some variations.

ⓖ,ⓗ: Fig. 7.16 illustrates the spectra for Troll A corresponding in time to fig. 7.15. Notice the similarity in the model simulations at the two locations. The simulated swell has almost the same amount of energy at Gullfaks C and Troll A for each respective time step. The corresponding radar spectra show the swell to be more powerful at

Gullfaks C than Troll A at 00UTC, while the opposite is found at 06UTC. Considering the heading of the dying swell, propagating south, and the more southerly position of Troll A, this observation seems possible.

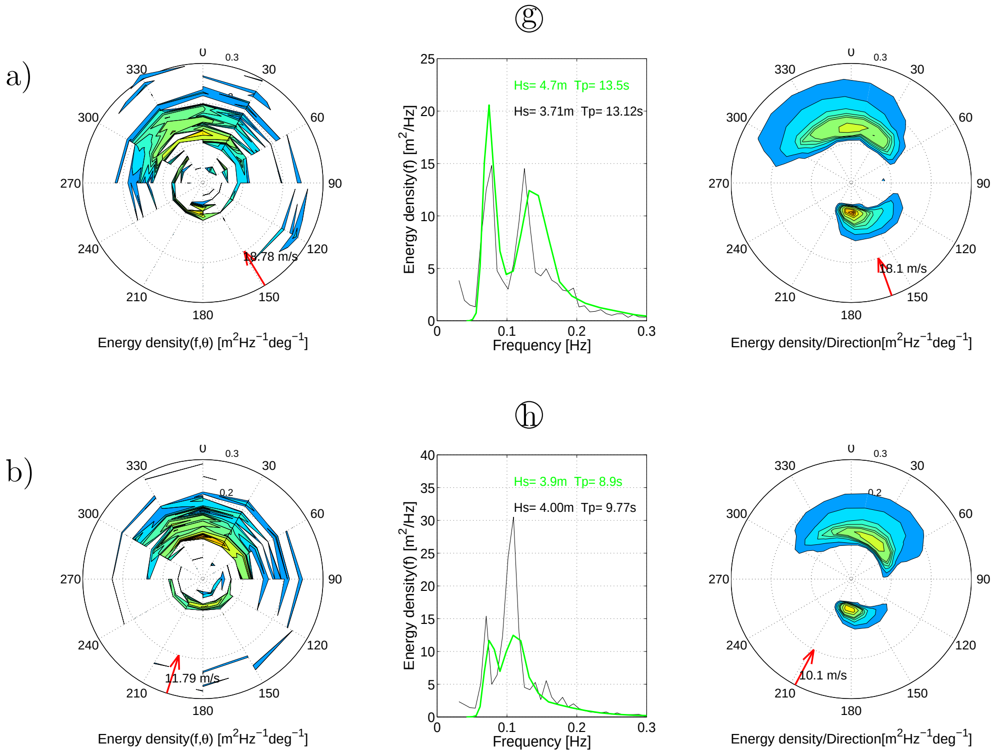

Figure 7.16: *Troll A: a) 00UTC and b) 06UTC 13. Dec. 2003. Left: 2D spectrum(MIROS-radar) and measured wind. Middle: 1D spectra with corresponding H_s and T_p, MIROS-radar(black) and WAM(green). Right: 2D spectrum(WAM) and modelled wind(HIRLAM).*

The biggest difference between the radar spectra obtained at Gullfaks C and Troll A is found in the representation of the wind-sea. At both time steps the wind-sea is more energetic at Gullfaks C, even though the local wind is much the same at the two adjacent locations, see fig. 7.4a)-d). This deviation is also reflected in the reduced H_s of Troll A. However, the position of Gullfaks C is more to the north, giving the wind-sea an increase of fetch compared to Troll A.

ⓘ,ⓙ,ⓚ: Sleipner A was the first position being exposed to the southerly generated wind-sea. Fig. 7.17 illustrates the wave condition from the very early stages of the wind-sea at 18UTC the 12th and 12 hours ahead. At 18UTC the wind-sea is almost nonexisting in the model simulations, even though the colored 2D spectra indicates its presence.

The spectra obtained at Gullfaks C, Troll A and Sleipner A very much confirm the findings made at Heidrun. The peak of the measured 1D spectra are on average more energetic than the corresponding model simulations in conditions of opposing swell. In addition, the downshift of the measured wind-sea peak is somewhat enhanced.

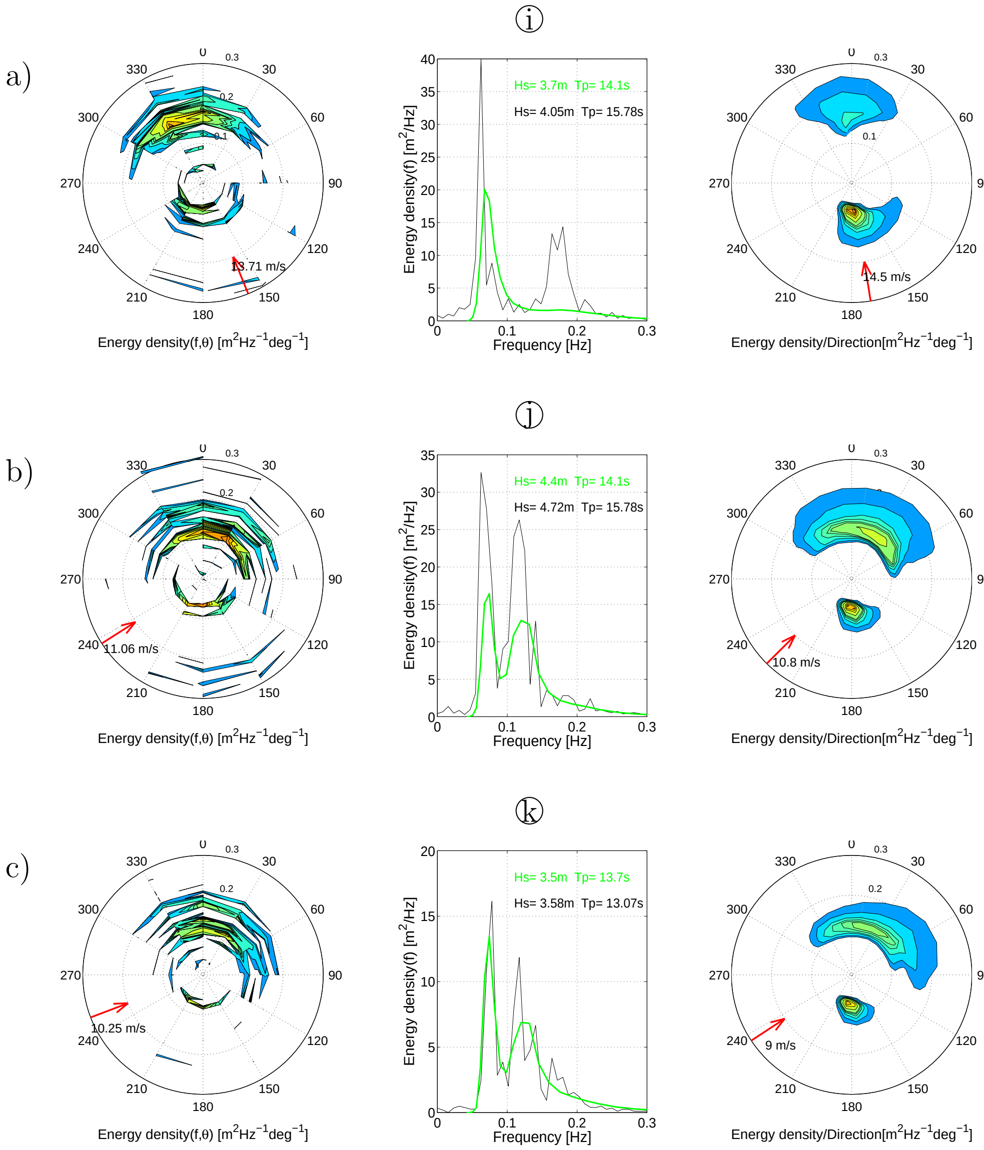

Figure 7.17: *Sleipner A: a) 18UTC 12. Dec., b) 00UTC 13. Dec. and c) 06UTC 13. Dec. 2003. Left: 2D spectrum(MIROS-radar) and measured wind. Middle: 1D spectra with corresponding* H_s *and* T_p*, MIROS-radar(black) and WAM(green). Right: 2D spectrum(WAM) and modelled wind(HIRLAM).*

7.1.5 Saturation range

Fig. 7.18 illustrates the mean simulated and measured 1D spectrum based on all spectra available from the four oil rigs during the 10-16th of December 2003. The simulations are seen in green and the measurements are colored black. Stippled lines represent the mean spectrum ±one standard deviation. In addition, an $0.0021f^{-4}$ relation, seen in red, is complemented as a reference measure.

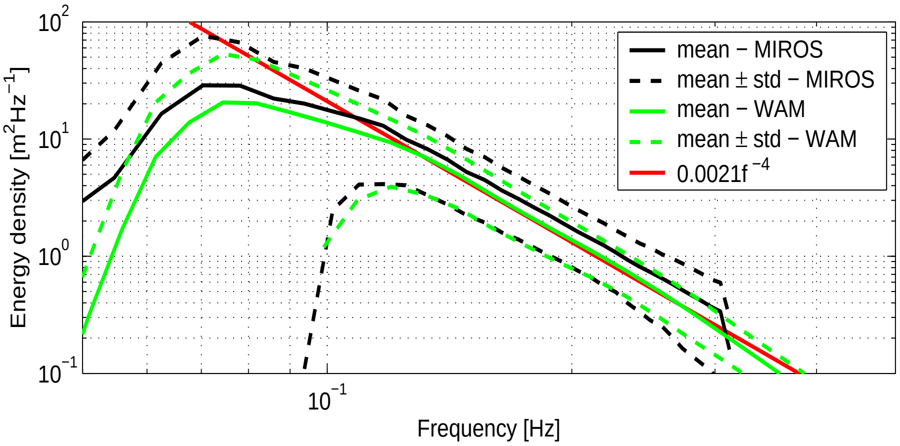

Figure 7.18: *The average simulated(WAM) and measured(MIROS) 1D spectra for Heidrun, Gullfaks C, Troll A and Sleipner A for the period 9th-16th of December 2003. The* $0.0021^{-4}f$*-function is given as a reference measure.*

7.1.6 Discussion

Wind forcing the model

Highly accurate wind fields are an absolute necessity in wave modelling. The simulated wave condition can be no better than the winds forcing the model. On the contrary, the wind input term of the model, represented by eq. 4.14, has an U_{10}^2 relation, squaring any inaccuracies inherent in the wind forcing.

In this study the modelled winds are compared to four point measurements. However, the simulated wave condition at one grid point is affected by a much larger area of the wind field than represented by the local wind. A high correlation between the model and measurements locally does not guarantee similar results elsewhere within the model area. This is well illustrated in fig. 7.7, by the nonproportional relation between the bias and rms for H_s and U_{10}. Notice how improved winds not necessarily are reflected in the significant wave height. With this in mind, the quality of the wind forcing will anyhow be judged based on these four positions, as no other quality-control is feasible with the available data.

Now, at what degree of accuracy can the atmospheric model be expected to simulate the winds forcing the wave model? Janssen et al. (1997) did a statistical study on the performance of the WAM-model(cycle-4) driven by ECMWF winds for the year 1995. The model was compared to buoy measurements, comprising wind and wave data, obtained at various locations in the Atlantic -and Pacific Ocean. Both regional and global statistics were carried out. The wind speed statistics of the northeast Atlantic and the U.S. west coast are summarized in table 7.4. The biases, also here with respect to observations, are positive, indicating that the average simulated winds were too strong. Similar calculations obtained from the 2003-case, based on far less observations, see table 7.1, show a higher positive bias. Unexpectedly, the lowest bias is found at Heidrun, even though this was the area closest situated to the strong gradients of the low pressure systems and shows the highest wind speed variability, see fig. 7.3a). Notice how the bias is growing from north to south, being almost twice the size comparing Heidrun and the southernmost platform, Sleipner A. The SI-indexes are slightly higher compared to Janssen et al. (1997), which is expected because of the fewer available observations, making the results more vulnerable to outliers. Because the 2003-case was a period of highly unstable air masses and fluctuating winds, the atmospheric model can be said to have simulated satisfactory wind speeds within this period.

The wind direction measurements of the 2003-case, see fig. 7.3 and 7.4, show a very good fit with the corresponding simulations, illustrated by the scatter plots of fig. 7.4. Notice that the area spanned by the four oil rigs has close to stationary wind directions during certain time periods, e.g. the last part of the time series where the wind direction is steady NNW on all stations. The same stationarity is not found in the wind speed. However, the three southernmost oil rigs, especially Gullfaks C and Troll A, have highly correlated winds throughout the period.

One should bare in mind that the modelled and measured data used in this study represent two different quantities. While the measurements are valid for only one particular position, the simulated data are mean values representing a whole grid box, illustrated by fig. 6.1. In certain situations of strong wind speed gradients, e.g. related to deep low pressure systems, the WAM-model with a 50km grid spacing may not properly resolve the wind field. This will affect the quality of the simulated wave condition.

Wave parameters: analysis/prognosis

The primary mission of an operationally driven wave model is to calculate the main wave parameters like the significant wave height, H_s, and the peak period, T_p. These quantities are most frequently used simply because they comprehend the most basic information describing the overall wave condition. The ability of the model to simulate these parameters as precise as possible is highly desirable and an ongoing study.

The wave parameter statistics deduced from the 2003-case are given in table. 7.1. As mentioned above, the average simulated winds were too strong. Consequently, one would expect the significant wave height to be overestimated. However, with the exception of Sleipner A, the simulated H_s is low on all stations. Notice how the bias in H_s is proportional to the bias in wind. As the mean simulated wind forcing gets stronger compared to the measurements going south, the simulated H_s behaves in the same way. First assumption is to interpret this as an overall underestimation by the model, indicating e.g. too strong dissipation, a too weak wind input term or an inaccurate saturation range.

In Janssen et al. (1997) the results for the northeast Atlantic were rejected for giving a too large underestimation of the modelled H_s, possibly caused by a malfunction in the buoys. The WAM-model performance for the northeast Atlantic and the U.S west coast are presented in tab. 7.4. Notice how the bias in H_s differ by a factor of two comparing the two geographical areas. However, later buoy improvements offered similar results for the northeast Atlantic as the U.S west coast.

Table 7.4: *Statistics for the WAM-model(cycle-4) performance compared to buoy measurement for January 1995 - December 1995, from Janssen(1997).*

	H_s		T_p		U_{10}(scalar)	
Area (Number obs)	Bias	SI	Bias	SI	Bias	SI
Northeast Atlantic(8812)	-0.53	0.14	-	-	0.29	0.19
U.S west coast(7234)	-0.27	0.15	-0.68	0.17	0.30	0.18

Comparing the total H_s statistics of the 2003-case to Janssen et al. (1997), see table 7.1 and 7.4, the WAM-model can be said to perform within satisfactory limits. Overall, the underestimation in H_s found in Janssen et al. (1997), is confirmed by the 2003-case taking into consideration the higher positive bias of the wind speed statistics. The poorer results at Heidrun may have several explanations. First of all, one should bare in mind the limited number of entries this statistics is based on. Shorter time periods are more vulnerable to outliers and poor simulations, which always will be present to some degree. For Heidrun the underestimation in the simulated H_s is much influenced by the last part of the period, see fig. 7.5a), caused by the inaccurate wind forcing at the time, see fig. 7.3a). Notice the strong gradients in the wind field at 12UTC the 14th in the area around Heidrun, illustrated by fig. 7.2f). The 50km grid spaced model, may have had difficulties simulating the wind field of this period and further affected the wave model performance. This shortcoming is likely fortified by the fact that the location of observation and grid point do not coincide very well at Heidrun.

Statistics based on the peak period, especially shorter time periods, will be highly influenced by the fluctuating behavior of T_p found in situations when two equally energetic wave systems are present. This is particulary evident in T_p during the first part of the 13th at Sleipner A, see fig. 7.6f). Notice how the model represents the long period swell around 13.5s, and how the radar switches between representing the swell and the much shorter peak period of the wind-sea. In reality the difference between the measurements and model are fractional, however the nature of the peak period may cause for significant statistical deviation. Anyhow, comparing the T_p statistics for the 2003-case with that of Janssen et al. (1997), prove the simulated T_p to perform very well in this period.

Of the less accurate $T_p$simulations, the biggest deviations are found at the three southernmost located oil rigs around noon the 15th, see fig. 7.6b),d) and f). The model is about 2s short compared to the measurements and consistent on all three stations. This misrepresentation in T_p may have been related to the poorly simulated U_{10} and H_s evident only hours earlier at Heidrun, see fig. 7.3a) and 7.6a). However, the local wind speeds show good correlation on all three stations, see fig. 7.4. Most likely the deviation in T_p was caused by too weak simulated winds further northwest, giving a reduced downshift of the peak compared to the measurements. It should also be mentioned that the peak period represented by the parametric format(type 2) of the WAM-model, see section 4.3.3, does not carry through a three point weighting of the peak, see eq. 6.5, which may have influenced the results by a poor frequency resolution.

The H_s and T_p statistics based on prognostic wind fields, +3h to +12h, do not indicate a reduction in quality, see tab. 7.2. On the contrary, H_s has an improved bias on all stations with the exception of Sleipner A. SI-indexes and correlation coefficients are more or less the same for H_s. T_p biases are slightly weakened on Heidrun and Gullfaks C, but improved on Troll A and Sleipner A. In addition, the SI-indexes for T_p are improved on all stations. Knowing the statistics are based on a small amount of data, one could expect these results to be a simple coincidence. However, similar findings have been made in the past. Komen et al. (1996) explained it by the fact that analyzed wind fields are a mixture of first-guess and measured data. Early prognostic wind fields generally shape better when the atmospheric model is integrated in time. Because the first few integrations only make minor adjustments to the analyzed winds, the error is kept small. Focusing on table 7.1 and 7.2, this may seem as a contradiction as the biases found in the forecasted winds are larger than those found in the analyzed winds. However, these statistics are only based on local winds, which only proves the wave condition to be influenced by a larger area of the wind field than represented by the local wind.

High/low frequency separation

As a wave system evolves the nonlinear interaction continuously redistributes energy to lower frequency components, evident by the downshift of the peak frequency, see fig. 4.1. In the initial stages of a wind-sea the majority of wind energy is absorbed by the shorter wave components, subsequently lower and lower frequencies are gradually affected. This implies that high and low frequency components have slightly different characteristics. The energy propagating with the shorter wave components are subjected to higher variability, as these waves respond faster to changes in the wind field. Because the low frequency components require a higher degree of enduring wind forcing to get 'activated', they can be said to be more stable and to represent the more developed part of the spectrum.

By separating the wave spectra into a high and low frequency part, deviations found in the total energy content, H_s, discussed above, may be more effectively isolated. It can also be an attempt to make a coarse separation of swell and wind-sea in those periods two or more wave systems are present. However, the wave field is dynamic and no constant frequency can distinguish swell from wind-sea in all situations. In this case the spectra was parted at f=0.094Hz. This choice of frequency is based on the spectra of fig. 7.15-7.17, which seems to fit more or less in between the peak of the wind-sea and the swell.

The calculated $H_{s,eq}$ based on total energy below and above 0.094Hz is illustrated in fig. 7.8 and 7.9. Originally the H_s time series obtained at Heidrun, fig. 7.5a) differs from the three other oil rigs, fig 7.6a), c) and e). However, when a low-pass filter is applied, removing the high frequency components, $H_{s,eq}$ for f<0.094Hz shows a similar trend on all stations. There are two clearly defined maxima in the time series, with a slight delay in the signal going south. Each maxima corresponds to the low pressure activity at the time, see fig. 7.2. The strength and endurance of the winds related to these two systems generated a significant amount of low frequency energy, while their northerly positioning made sure the wave energy arrived at different points in time at each oil rig, especially during the "Edda". The low frequency energy can be said to make up the basis of the wave field in this period. Accordingly, all remaining wave energy on higher frequencies are more locally dependent. This is illustrated by the different variability seen in the $H_{s,eq}$ deduced from the two parts of the spectrum. Notice how the low frequency $H_{s,eq}$ has a somewhat clearly defined shape, while the high frequency counterpart is more irregular. If studying the wind speed at all stations, fig. 7.3a) and 7.4a), c) and e), compared to the high frequency energy content, fig. 7.8a) and 7.9b), d) and f), there are obvious similarities.

As the high frequency components are subjected to higher variability, one could expect the model simulations to be less accurate in this part of the spectrum. This assumption is based on the fact that the model is forced by new wind fields every three hours. In highly unstable conditions this might be too scarce to resolve rapid changes in the wind field. However, focusing on the summary statistics given in table 7.3, there are no indications of a reduced model performance in the high frequency part of the spectrum. On the contrary, compared to the low frequency part, the biases are improved on all stations with the exception of Sleipner A. And, all SI-indexes are found lower.

Approaching/receding waves relative to radar heading

The MIROS-radar is based on the assumption that opposite propagating wave systems can not contain energy on the same frequencies (Grønlie 1999), i.e. the radar is unable to represent similar frequency-direction bins with 180 degrees ambiguity. This limitation is found in the construction of the radar, which only illuminates a 180 degrees sector, see chapter 3. However, in the open ocean opposing wave systems are a frequent phenomenon. In these situations it can be expected that there will be a loss of wave energy represented by the radar. Question arises whether the radar is more likely to represent approaching than receding waves or viceversa? In other words, is the radar sensitive to its heading or does it always sense the most energetic wave system independent of its direction of propagation relative to the radar? And, how significant is the energy loss?

Based on the performance of the model compared to the radar, discussed above, the radar's ability to measure approaching and receding waves may be analyzed. The calculated $H_{s,eq}$ for approaching and receding waves relative to the radar heading is illustrated in fig. 7.10 and 7.11. The summarizing statistics are given in table 7.3. Out of the four positions only the data obtained at Heidrun indicate the radar to perform better measuring approaching waves. In return, the difference is profound, with a bias close to -1.3m in the receding sector. Even when taking into account the underestimation found in the simulated H_s at Heidrun, see table 7.1, the radar measurements contain more energy in the receding sector compared to the model. Now, if the radar was to be less reliable measuring receding waves an energy loss would be expected rather than an energy gain relative to the model. It is therefore more likely that the negative bias of the receding sector of Heidrun lay within the model results and not the radar measurements.

The same calculations obtained at the remaining oil rigs offer opposite results compared to Heidrun. Here, all statistics show better correspondence between the model and the radar for the receding sector. However, the difference between the two sectors are not as profound as seen at Heidrun. All in all, the deviating results of Heidrun compared to the other oil rigs do not support the idea that the radar generally performs better measuring either approaching or receding waves relative to its heading.

So far statistics based on the entire time period of the 2003-case have been discussed. However, only smaller periods saw the presence of two opposing wave systems, which probably reflects the condition the radar is most likely to perform dissatisfactory. Some of the wave spectra given in section 7.1.4 lie within these time intervals. According to the simulated 2D spectra of fig. 7.15, the two opposing wave systems are overlapping at around 0.1Hz. Notice how the corresponding 2D spectra obtained by the radar are unable to represent the tail of the N swell as indicated by the simulations. The measured N swell is only represented in a very small frequency-interval. Because the frequencies covering the tail of the swell are less energetic than that of the corresponding frequencies of the wind-sea, the radar automatically represents the wind-sea. This means the energy contained by the tail of the swell is not accounted for in the radar measurements. The same scenario is illustrated in fig. 7.16 and 7.17 for Troll A and Sleipner A. Notice how the measured N swell becomes narrow and more indistinct as the peak of the wind-sea moves closer to the peak of the swell. However, the corresponding 1D spectra of fig. 7.15-7.17 do not seem to be highly affected.

Now, how much does this shortcoming in the radar affects the total energy, or H_s, of the measurements. Because the majority of energy is found near the peak of the spectrum, a significant energy loss may only be present when two wave systems of 180 degrees ambiguity have approximately coinciding peak frequencies. This is not the case in the 2003-case and therefore not easily tested.

Saturation range

The growth of wind waves are not infinite. At one point balance between the three source terms, wind-input, dissipation and nonlinear interaction, is obtained. This is evident in the tail of the spectrum, $1.5f_p < f < 3f_p$, where the energy level is more or less constant for a wind-sea. An universal relation expressing the slope of the tail was first proposed by Phillips (1958) using a f^{-5} power law. Since then several studies (Phillips 1985; Kitaigorodski 1983; Toba 1973; Forristall 1981) have shown a better fit using an f^{-4} relation. However, this law will not apply to swell because swell often are unsaturated wave systems, caused by the dispersion characteristic of ocean waves.

The 2003-case was dominated by high winds and well developed seas combined with swell. Fig. 7.18 illustrates the average modelled and measured 1D spectrum for all four positions for the entire period. As expected the model shows a good fit with the f^{-4} power law, represented by the red line. The measurements indicate a weaker decline, fitting better a -3.8 exponent, giving it a more energetic tail compared to the model. This difference in saturation range may explain some of the underestimation seen in the simulated H_s. Liu (1989) examined more than 2200 well-developed wave spectra during storm conditions in the Great Lakes and found the exponent to vary from -3.5 to -5.5, which clearly underlines the uncertainty of a f^{-4} power law.

Wind-sea growth in the presence of an opposing swell

During the 2003-case all four oil rigs experienced a period where the wave condition was dominated by the presence of a swell and an opposing wind-sea. The N swell was the last trace of the low pressure system "Edda". As the wind turned from N-NW to SE-SW a new wind-sea evolved. Depending on location, this wind/counter-swell situation took place around the 13th. A selection of measured and simulated wave spectra at the time are presented in fig. 7.13b), 7.15, 7.16 and 7.17. Focusing on the 1D spectra, a weak deviating trend between the simulated and measured high frequency wind-sea system can be seen. The measured wind-sea is slightly more energetic and has a more downshifted peak. Both effects indicate a higher degree of energy transference from air to sea in the measurements compared to the simulations. This could possibly be the result of an increased drag coefficient influenced by the opposing swell. As this effect is not accounted for in the model, the simulated wind-sea system evolves accordingly. However, there are several uncertainties connected to this finding.

First, lets compare the developing wind-sea of the 2003-case with the work of Ardhuin (Sub) shown in fig. 5.1c) and d). The wave conditions of these two cases are comparable, however, obvious differences are found in the 1D spectra. Unlike the 2003-case the simulated wind-sea of Ardhuin (Sub) showed to be more evolved compared to the corresponding measurements, see fig. 5.1c). This effect was explained by the poorly parameterized dissipation-term of the WAM(cycle-4)-model, giving a too strong wind-sea growth in mixed swell/wind-sea conditions, see chapter 5. Knowing the models used in both cases are based on the same dissipation-term, the simulated wind-sea of the 2003-case should behave in the same way relative to the measurements. The fact that it shows the opposite trend, only fortifies this difference. However, there are a few possible explanations for this behavior.

Besides having swell opposed by wind, the two cases are different in several ways. First of all, the swell reported in Ardhuin (Sub) had a $H_s \approx 1m$ and $T_p \approx 10s$. Correspondingly, the low frequency $H_{s,eq}$ of fig. 7.8 and 7.9, approximately representing the wave height of the swell, is about 3m. In addition, the peak period of the swell is 12-15s, depending on position, see fig. 7.5 and 7.6. The possible effect swell may have on the drag coefficient is likely to vary with different types of swell. The more energetic swell of the 2003-case may have had an increased effect on the drag coefficient.

Probably the most important difference between the two cases is found in the wind conditions, and at what degree these are possible to survey. While the work of Ardhuin (Sub) was based on data obtained in nearly idealized fetch-limited conditions, the 2003-case was not chosen with the same carefulness. The SE-SW wind-sea illustrated in fig. 7.13b), 7.15, 7.16 and 7.17 has no clearly defined fetch caused by the irregular coastline found in the south, see fig. 6.1, and the wind field is no near stationary in the actual time period, see fig. 7.3 and 7.4. The advantage of working with an idealized fetch-limited case is found in the steady wave field this type of condition produces, that is, assuming any distant generated swells are close to being stationary within the studied area. A steady wave field allows for time averaging, offering more stable measurements, as well as simulations. Besides, not only is a stationary wind field less subjected to gustiness, effects of gust winds are more likely to be attenuated when the measured wave field is averaged over some period of time. Because this random characteristic of the wind field is uneasily simulated, its effect on the wave field is not accounted for in the WAM-model. Therefore, in non-stationary wind conditions, when no time averaging of the wave field may be carried through, a comparison of measured and simulated wave spectra are more likely to show higher deviation caused by gust winds. Komen et al. (1996) reported extra energy transference to waves in conditions of high wind fluctuations. This effect may have influenced the results of the 2003-case.

An other source of error lays within the spacial and temporal resolution of the two models. The model used in Ardhuin (Sub) had about a 1000 times higher resolution in space and 15 times smaller integration time step, which obviously offer increased accuracy in the wind forcing and wave simulations. Now, if the 2003-case had been obtained in stationary wind conditions, this factor would not have been of significant importance. Since this was not the case, there are more uncertainties connected to the accuracy of the wind forcing. For the 2003-case one can only rely on the local wind comparisons between the model and simulations. However, as seen in fig. 7.4, the wind does not indicate any larger gradients in space between the three southernmost oil rigs, changing more or less uniformly with time. Especially the winds found at Gullfaks C and Troll A tend to be highly correlated. Therefore, the poorer spacial resolution of the WAM-model used in the 2003-case may not have reduced the accuracy of the simulations significantly.

The difference between the simulated and measured wind-sea seen in the 1D spectra of fig. 7.13b) and 7.17a) are striking. However, both measured spectra have a peak frequency above 0.15Hz. When applying a JONSWAP-spectrum, it can be found that with 20m/s wind speed, less than a 80km fetch is needed to generate a similar wave system, see fig. 2.4. 80km does not even cover two grid boxes in the model, which only proves that a small misrepresentation at one grid point is enough to influence the results found in the 2003-case.

Despite all uncertainties attached to these data, the trend is the same for all positions, which somewhat strengthen the findings. Focusing on the H_s results given in fig. 7.5 and 7.6, there are no indications of the integrated parameters being significantly affected by the interaction of swell and wind-sea. This result corresponds to the findings made in Ardhuin (Sub).

7.2 8-12th of February 2000

7.2.1 Wind conditions

Synoptic scale

During the 2003-case the wave conditions were primarily dominated by ”local” atmospheric low pressure systems. The majority of wave energy affecting the four oil rigs was generated in the North -and Norwegian Sea, see fig. 7.2. In the following case, the 8-12th of February 2000, the wave conditions are to a higher degree also influenced by more distant wind fields.

Norway finds itself some what in the corner of the Atlantic Ocean. In wintertime the stretch of open ocean is limited by ice in the north, Greenland in the west and Great Britain and mainland Europe in the south and southwest. WSW is the only direction directly exposing the four oil rigs to vast stretches of open ocean, with maybe the exception of Sleipner A. Heidrun has also increased exposure from the SW.

February the 9th 2000 all four radars measured peak periods exceeding 20 seconds, an event not to often experienced in this area. Wavelengths of such magnitude demand special wind conditions to be generated. Fig. 7.19 illustrates the wind fields of the North Atlantic at 12UTC from the 5th to the 10th of Feb. 2000. Notice how the majority of strong winds are coming from the SW. The color coding indicates that the strongest winds nearly follow a thought developing SW wave system day by day, continuously keeping it energetic or growing.

In the following analysis all data obtained at the four oil rigs are analyzed simultaneously, as the wave conditions of each position were influenced much by the same wave systems.

Local scale

The measured and simulated winds at the four oil rigs are illustrated in fig. 7.20. As seen in the 2003-case, the two wind sensors, indicated by the black and red line, disagree at times in their wind speed representation. Once again the sensors measuring the strongest winds are prioritized and make up the basis for the following discussion and the corresponding scatter plots of fig. 7.20.

The main focus of the 2000-case will be made on the period where the powerful WSW swell had moved into the area spanned by the four radars and a new wind-sea was building. Depending on position the arrival of the swell varies slightly. Here, the circled letters of fig. 7.20 mark the hours where measured and simulated 2D spectra are presented in section 7.2.4, which correspond to the hours expected to have increased swell/wind-sea interaction. Notice that these periods are mainly dominated by S-SW winds, with the exception of Sleipner A where the wind direction is NW-SW. On average the quality of the simulated winds prior to and within these periods are fairly

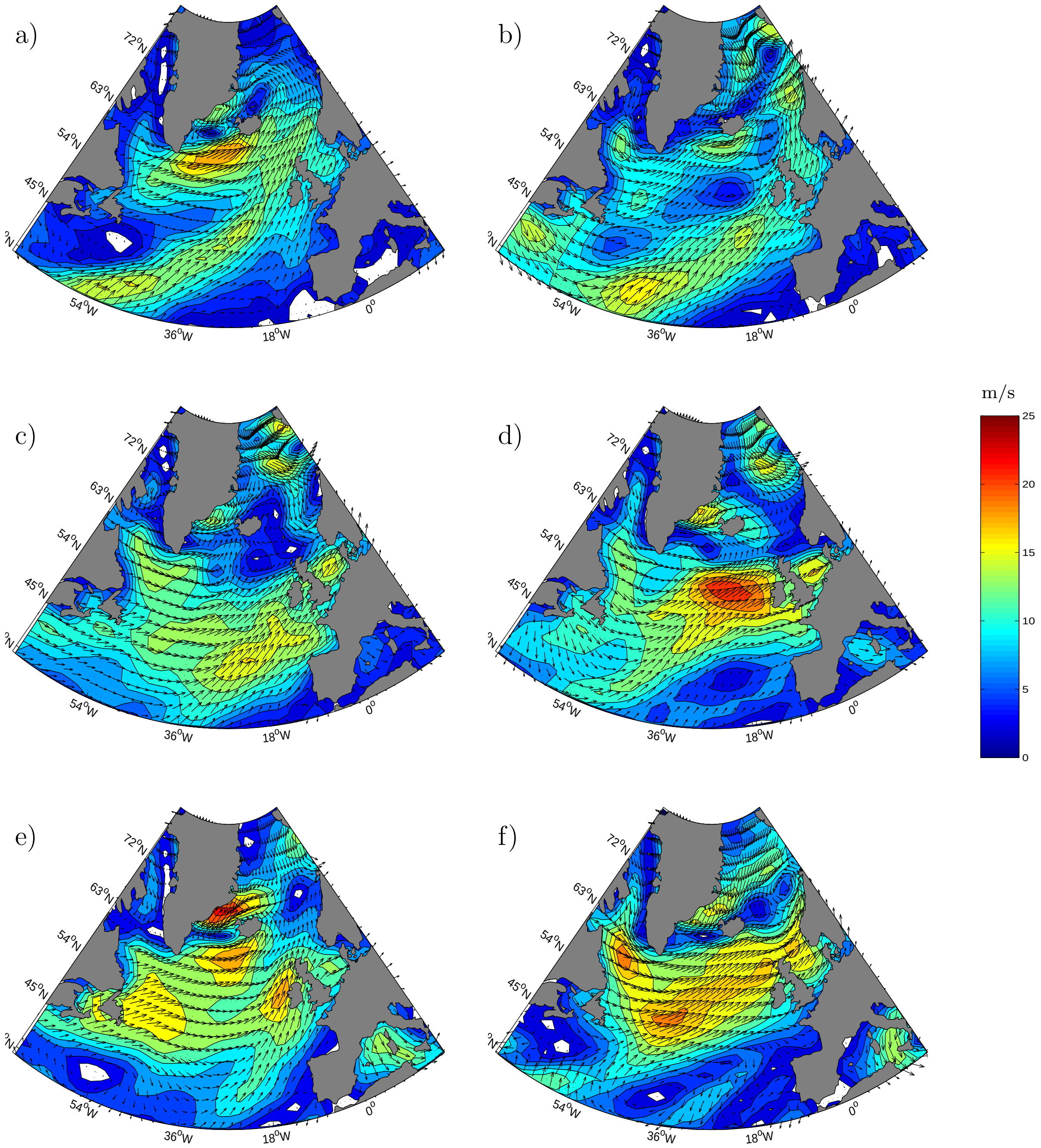

Figure 7.19: *Analyzed sea surface winds(10m) for the northern Atlantic at 12UTC the a)5th - f)10th of February 2000. Data are obtained from NCEP-NCAR(http://ingrid.ldeo.columbia.edu/).*

good. Of the four positions, the biggest deviation is found at Sleipner A around the 9th where the simulated winds are too weak. At Heidrun, the 30 hour time period starting at 18UTC the 9th, is dominated by high wind speed variability, where the simulated

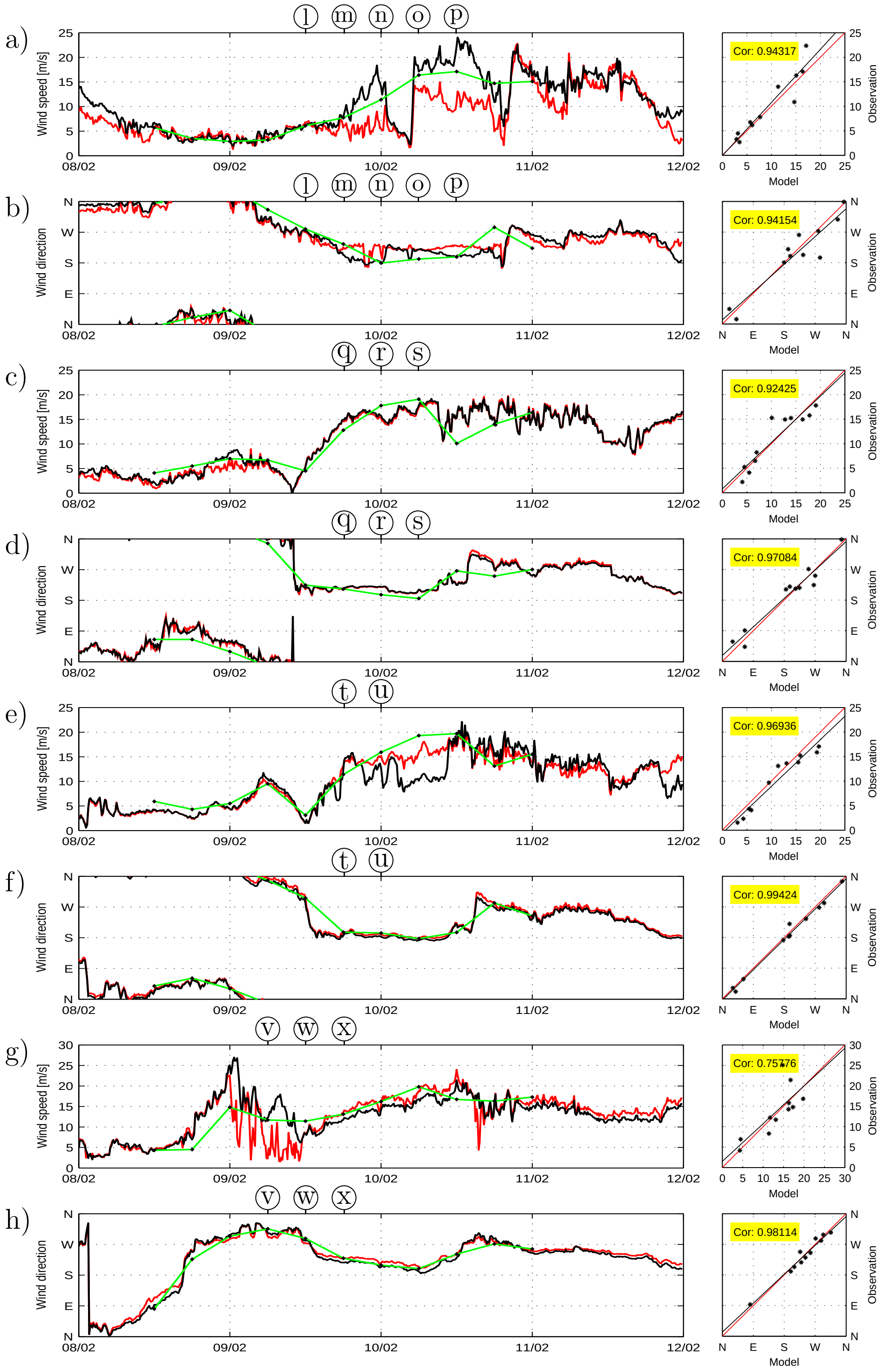

Figure 7.20: *Wind speed and wind direction with corresponding scatter plots for the period 8th - 12th of February 2000. Observations: sensor A(red line) and sensor B(black line). Model: HIRLAM(green line). Scatter plots are based on the data of the sensor with best fit to the model. a),b): Heidrun; c),d): Gullfaks C; e),f): Troll A; g),h): Sleipner A.*

wind speed is either too weak or too strong compared to the measurements.

The wind direction time series of the four oil rigs are illustrated in fig. 7.20b), d), f) and h). Model and measurements are highly correlated on all stations, see the corresponding scatter plots, with the poorest results found at Heidrun the around 18UTC the 10th(+42h forecast).

7.2.2 Wave parameters: H_s & T_p

Fig. 7.21 illustrates the simulated and measured H_s and T_p. Notice that the most considerable deviation found in the simulated wind speed at Heidrun and Sleipner A, noted above, are also reflected in the increased deviation of H_s at the time.

For Heidrun, see fig. 7.21, the measured H_s is increasing around 03UTC the 10th despite weak local wind at the time, see 7.20a). This can only be explained by advected wave energy in the form of swell. The corresponding simulated H_s is also growing, but not at the same rate. Unfortunately, the simulated wind speed is not known at this hour. However, if the simulated wind was to be as indicated by fig. 7.20a) one should expect the simulated H_s to be at least the height of the measured H_s.

At the beginning of the time series representing Troll A, the H_s measurements , see fig 7.21e), bare proof of being influenced by some sort of malfunction in the radar. Compared to the measurements made at the closely situated Gullfaks C, the significant wave height seems unrealistically low. The deviation to the simulated H_s is obvious. Several spikes in the signal underline the suspicion of something being wrong. At Gullfaks C at 10UTC the 9th a similar spike is found in the measured H_s, coinciding perfectly with a moment of calm wind, see fig. 7.20c). Besides obvious shortcomings in the measured H_s, the quality of the T_p measurements do not seem affected at neither of the two oil rigs.

Around midday the 9th, depending on oil rig, all radars indicate T_p to be above 20 sec, see fig. 7.21. As Gullfaks C and Troll are only 101km apart, they are subjected to the same wave systems more or less at the same time. This is eveident in fig. 7.21d) and f) where both radars show a coinciding jump in the T_p measurements around 09UTC. Heidrun, situated further north, shows the same signal only six hours later. Knowing the swell is coming from the WSW, illustrated in the 2D spectra of section 7.2.4, Sleipner A is somewhat in the shadow of Great Britain and therefore not dominated by the long period swell in the same way as the other three oil rigs. Most importantly, the reader should acknowledge the difference in simulated and measured T_p at the time the swell is present. The data deviate in the 3-4s range depending on position.

All in all table 7.5 summarizes the model performance compared to the radar for the 2000-case. As the quality of the H_s-measurements obtained at Troll A seem corrupt, the total H_s-statistics are presented with and without theses data.

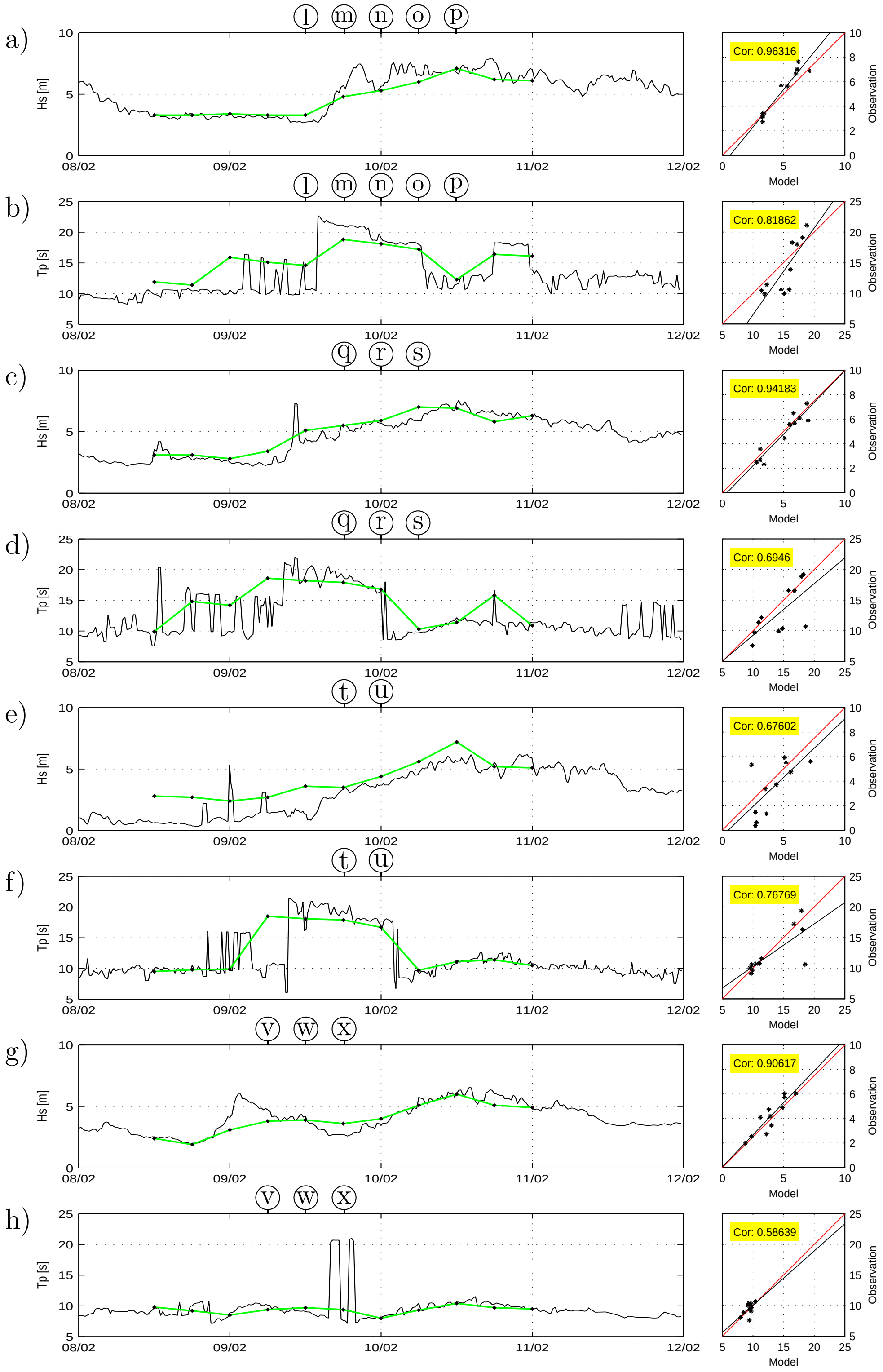

Figure 7.21: *Significant wave height, H_s, and peak period, T_p , with corresponding scatter plots for the period 8th - 12th of February 2000. Observations: MIROS-radar(black line). Model: WAM(green line). a),b): Heidrun; c),d): Gullfaks C; e),f): Troll A; g),h): Sleipner A*

Table 7.5: *Summary statistics of significant wave height H_s, peak period T_p and wind speed U_{10} in the time period 8-10th February 2000 , based on analyzed and prognostic wind fields. The bias is with respect to measurements. SI is scatter index, RMS is root-mean-square error and Corr is correlation. Number of entries are given in parentheses. The total H_s statistics are given with and without the results obtained at Troll A.*

	$H_s[m]$				$T_p[s]$				$U_{10}[m/s]$(scalar)			
Position (entries)	Bias	RMS	SI	Corr	Bias	RMS	SI	Corr	Bias	RMS	SI	Corr
Heidrun(11)	-0.30	0.65	0.13	0.96	1.31	2.87	0.21	0.82	-0.71	2.22	0.22	0.94
Gullfaks C(11)	0.22	0.61	0.13	0.94	1.45	3.16	0.24	0.69	-0.19	2.10	0.19	0.92
Troll A(11)	0.66	1.65	0.48	0.68	0.65	2.50	0.20	0.77	1.15	1.82	0.18	0.97
Sleipner A(11)	-0.24	0.62	0.15	0.91	-0.12	0.77	0.08	0.59	-0.48	3.87	0.28	0.76
Total(44)	0.09	1.00	0.23	0.85	0.82	2.51	0.21	0.79	-0.06	2.63	0.23	0.90
Total(33)	-0.11	0.63	0.13	0.93								

7.2.3 Integrated spectra: $H_{s,eq}$

Table 7.6 summarizes the comparison between the simulated and measured $H_{s,eq}$ based on energy above and below 0.094Hz and energy approaching and receding the radar. Once again the total statistics are given with and without the data obtained at Troll A.

Table 7.6: *Summary statistics for $H_{s,eg}$, WAM-model vs MIROS-radar, deduced from wave energy receding/approching the 180 degrees grazing sector of the radar at each respective oil rig and energy above/below 0.094Hz in the time period 8-10th February 2000. The bias is with respect to measurements. SI is scatter index, RMS is root-mean-square error and Corr is correlation. Number of entries are given in parentheses. Total are given with and without the results obtained at Troll A.*

	$H_{s,eq}$ (receding)				$H_{s,eq}$ (approaching)				$H_{s,eq}$ (f<0.094Hz)				$H_{s,eq}$ (f>0.094Hz)			
Pos(entries)	Bias	RMS	SI	Corr	Bias	RMS	SI	Corr	Bias	RMS	SI	Corr	Bias	RMS	SI	Corr
Heidrun(11)	0.07	0.72	0.17	0.97	-0.57	0.79	0.32	0.22	-0.23	0.81	0.20	0.95	-0.16	0.40	0.13	0.93
Gullfaks C(11)	-0.52	0.80	0.27	0.75	0.59	0.91	0.25	0.90	0.37	0.63	0.18	0.93	-0.09	0.34	0.11	0.97
Troll A(11)	-0.21	1.13	0.72	-0.30	0.76	1.43	0.47	0.78	0.57	1.04	0.49	0.75	0.55	1.48	0.59	0.55
Sleipner A(11)	-0.07	0.56	0.17	0.84	-0.38	0.49	0.20	0.97	-0.30	0.58	0.28	0.80	0.17	0.54	0.16	0.86
Total(44)	-0.18	0.83	0.28	0.88	0.10	0.96	0.33	0.82	0.09	0.79	0.27	0.88	0.12	0.83	0.27	0.77
Total(33)	-0.17	0.70	0.20	0.91	-0.12	0.75	0.26	0.88	-0.07	0.68	0.22	0.91	-0.03	0.43	0.14	0.92

7.2.4 Wave spectra: 1D & 2D

Heidrun

ⓛ: The wave condition of the 2000-case is of special interest first and foremost for being dominated by a very long period swell. Fig. 7.22a) illustrates the simulated and measured wave spectra for Heidrun at 12UTC the 9th. This is the last time both spectra are available before the high energy swell propagates into the area with full force. As seen in fig. 7.21b), the peak period is not yet dominated by the swell. However, already at this point the simulated spectra indicate the arrival of the swell, without being evident in the measurements. In addition to the WSW swell, a weaker NNW swell with peak frequency around 0.1Hz can be recognized in both data.

The wave spectra illustrated in fig. 7.22a) are very much representative for the wave condition found at Heidrun the preceding 24 hours, a period dominated by moderate wave heights and the absence of any wind-sea systems.

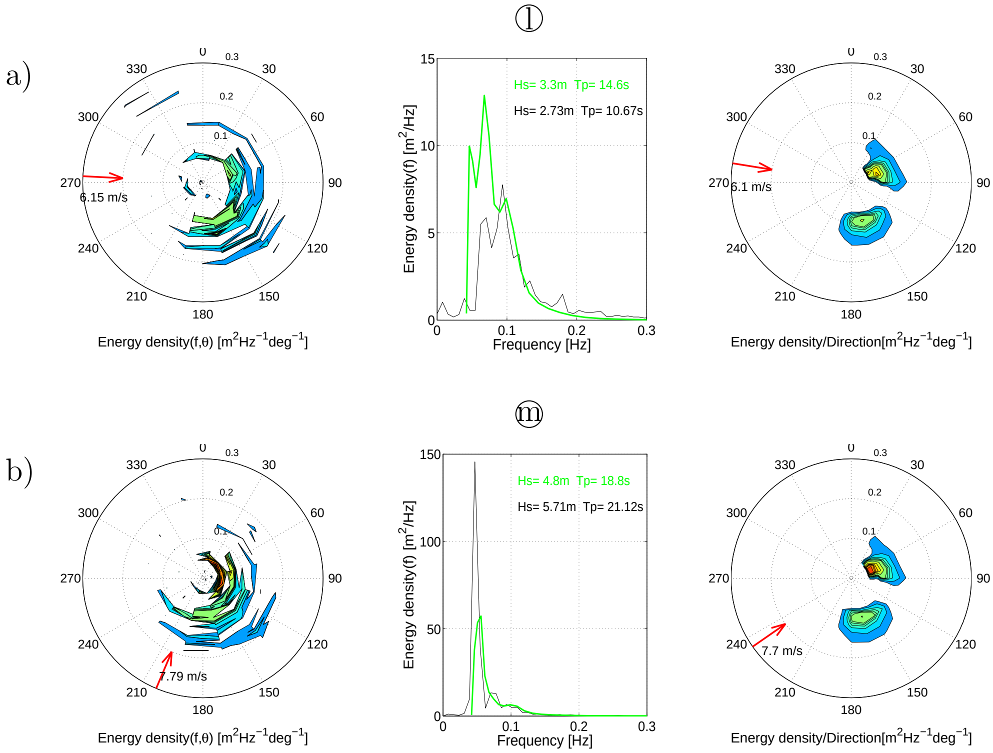

Figure 7.22: *Heidrun: a) 12UTC and b) 18UTC 9. Feb. 2000. Left: 2D spectrum(MIROS-radar) and measured wind. Middle: 1D spectra with corresponding H_s and T_p, MIROS-radar(black) and WAM(green). Right: 2D spectrum(WAM) and modelled wind(HIRLAM).*

ⓜ: At 18UTC the 9th, the situation does not seem significantly altered focusing on the simulated 2D spectra of fig. 7.22b). However, the change in coloration of the WSW swell represents an increase of energy. This becomes more evident in the corresponding simulated 1D spectrum.

In fig. 7.22a) the WSW swell is absent in the measurements. At this stage, the swell is clearly defined by an abrupt energy shoot-up in the 1D spectrum, see fig. 7.22b). Also notice the altered appearance of the measured 2D spectrum compared to that obtained 6 hours earlier.

The measured 1D spectrum portraits a distant generated wave system. A probable long passage made sure the swell 'cleaned up' before reaching the area of observation, creating the narrow shape of the spectrum. This is caused by the dispersive characteristic of ocean waves, expressed by eq. 2.7. The width of the spectra can in that way reflect the distance covered by the wave system and say something about its origin.

ⓝ, ⓞ, ⓟ: At 00UTC the 10th, fig. 7.23a), the modelled and measured WSW swell are almost coinciding, with the model being slightly more energetic. A new wind-sea is appearing in the radar measurements centered around 0.13HZ, but is nonexisting in the model. Six hours later, see fig. 7.23b), the swell is dropping while the wind-sea seen previously in the measurements start to appear in the simulations. However, comparing the two representations the measured wind-sea is clearly more evolved. Another six hours later, see fig. 7.23c), the swell is still dropping and the wind-sea has reached, and slightly exceeded, its energy level. The swell is barely visible on the low frequency side of the 1D spectra. At this stage, the simulated wind-sea has finally caught up with the measurements and fit very well.

Generally the wind, illustrated by the red arrows of the 2D spectra, is going with/across the direction of the swell in the period spanned by fig. 7.23. In addition, it should also be noted that the measured 2D spectra do not indicate the presence of the N swell, seen in the corresponding simulations.

Gullfaks C

ⓠ, ⓡ, ⓢ: The modelled and measured wave spectra representing the wave condition at Gullfaks C at 18UTC the 9th show high similarity, see fig. 7.24a). Notice that the heading of the swell is more straight W compared to Heidrun. The building SSW wind-sea is not obvious in the 1D spectra, but is well illustrated in both 2D spectra. Unlike the 2D spectra obtained at Heidrun, the N swell is better represented at Gullfaks C. And, the simulated long period swell is now more energetic than the measured swell.

At 00UTC the 10th, the 1D spectra fit very well, see fig. 7.24b). Both peaks, swell and wind-sea, are coinciding and do not differ significantly in energy. Six hours later, illustrated in fig. 7.24c), the energy level is somewhat deviating, caused by a broader wind-sea representation by the model. However, the peaks are still coinciding in frequency.

As observed at Heidrun, the wind direction of this period is going with/across the heading of the swell.

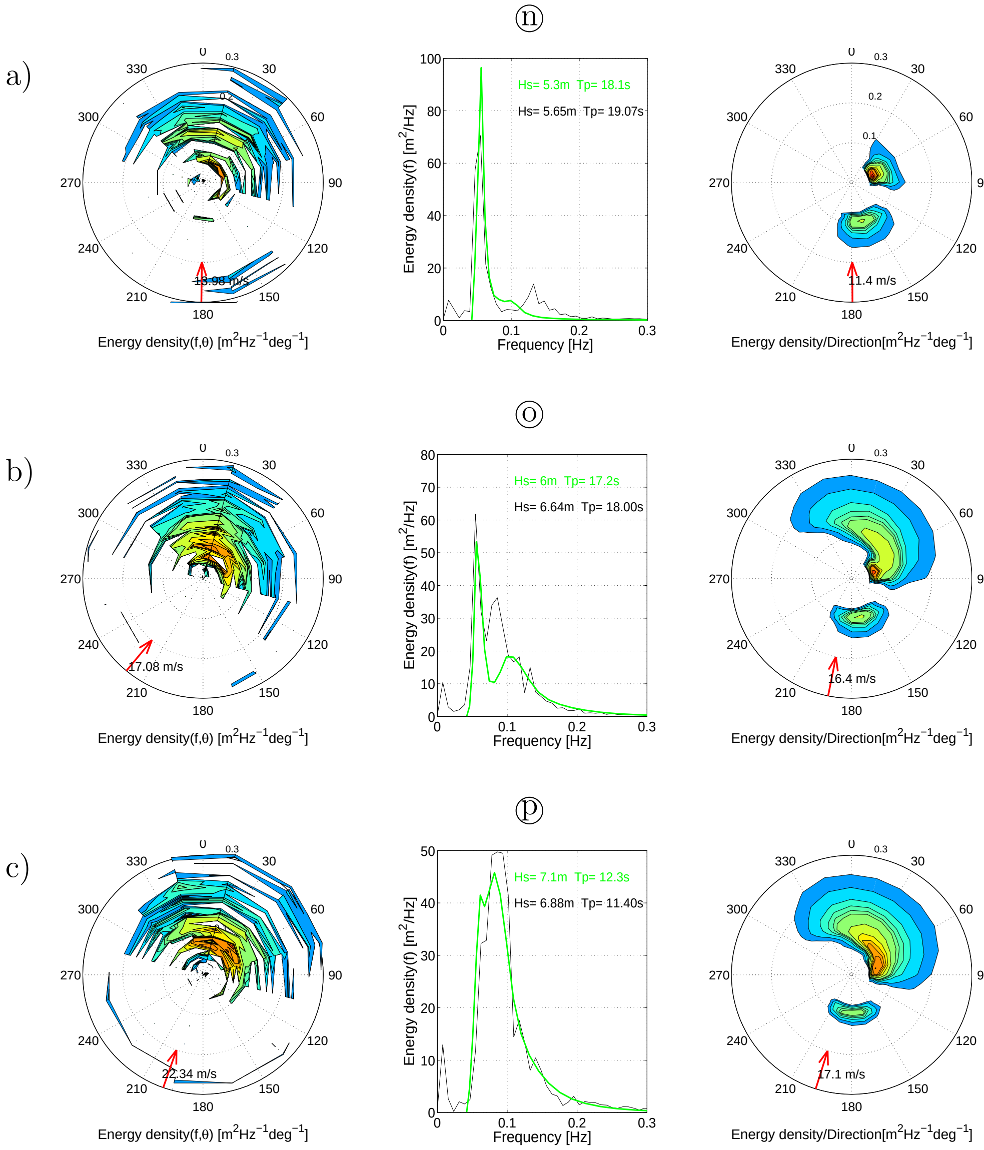

Figure 7.23: *Heidrun: a) 00UTC, b) 06UTC and c) 12UTC 10. Feb. 2000. Left: 2D spectrum(MIROS-radar) and measured wind. Middle: 1D spectra with corresponding H_s and T_p, MIROS-radar(black) and WAM(green). Right: 2D spectrum(WAM) and modelled wind(HIRLAM).*

Troll A

ⓣ, ⓤ: Fig. 7.25 illustrates the wave spectra obtained at Troll A at 18UTC the 9th and 00UTC the 10th. Notice the significant difference between the measured and modelled wind-sea in the latter 1D spectra. In this period the wind is almost perpendicular to the W swell.

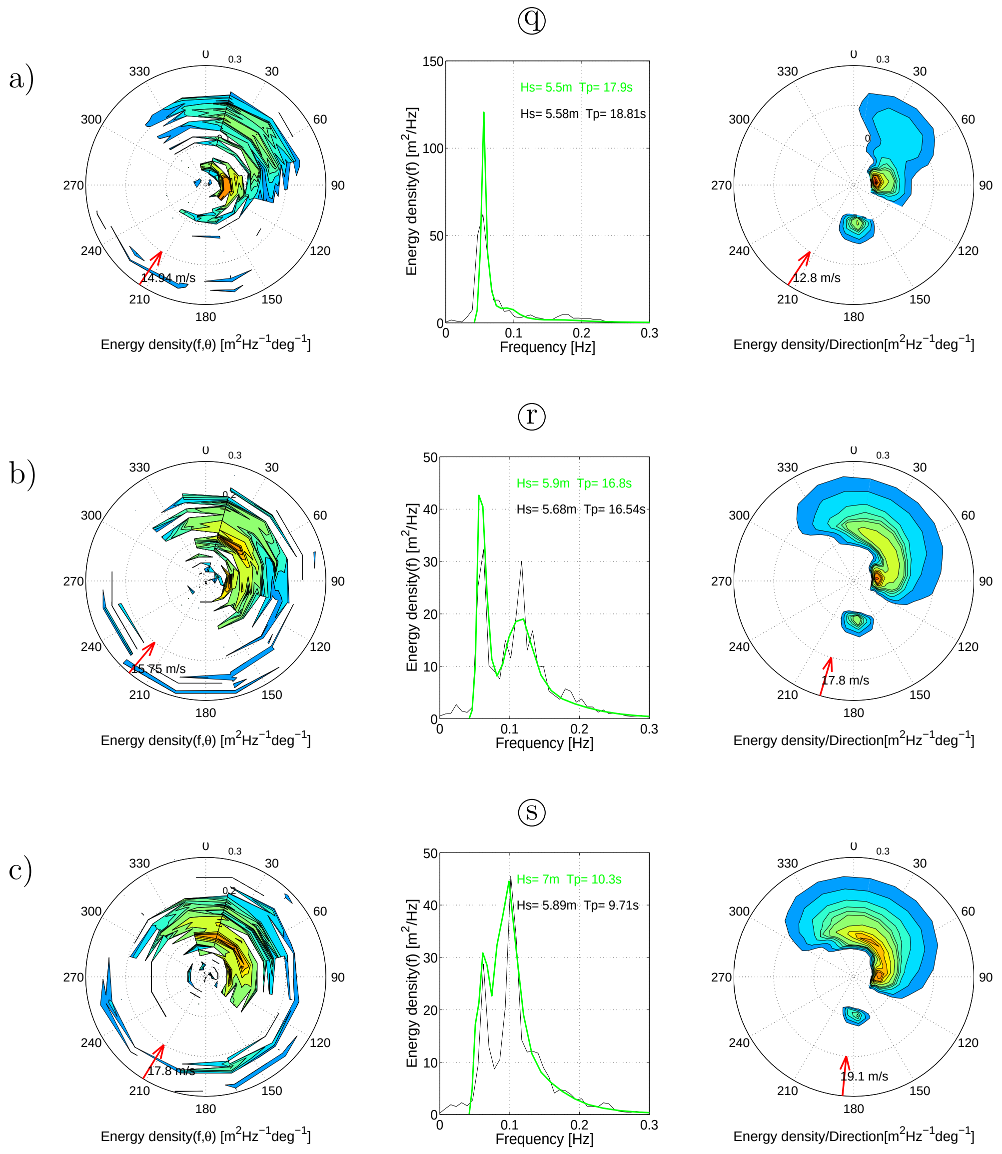

Figure 7.24: *Gullfaks C: a) 18UTC 9. Feb, b) 00UTC 10. Feb and c) 06UTC 10. Feb. 2000. Left: 2D spectrum(MIROS-radar) and measured wind. Middle: 1D spectra with corresponding H_s and T_p, MIROS-radar(black) and WAM(green). Right: 2D spectrum(WAM) and modelled wind(HIRLAM).*

Sleipner A

The wave spectra illustrating the wave condition at Heidrun, see fig. 7.22 and 7.23, indicate the origin of the long period swell to be WSW. This puts Sleipner A in the shadow of Great Britain, see fig. 6.1, not directly exposing the oil rig to the wave system. However, some of the energy is refracted and affects the waters surrounding Sleipner A.

ⓥ: Fig. 7.26a) illustrates the wave condition at Sleipner A at 12UTC the 9th, which is just prior to the arrival of the long period swell. At this stage the wave condition is

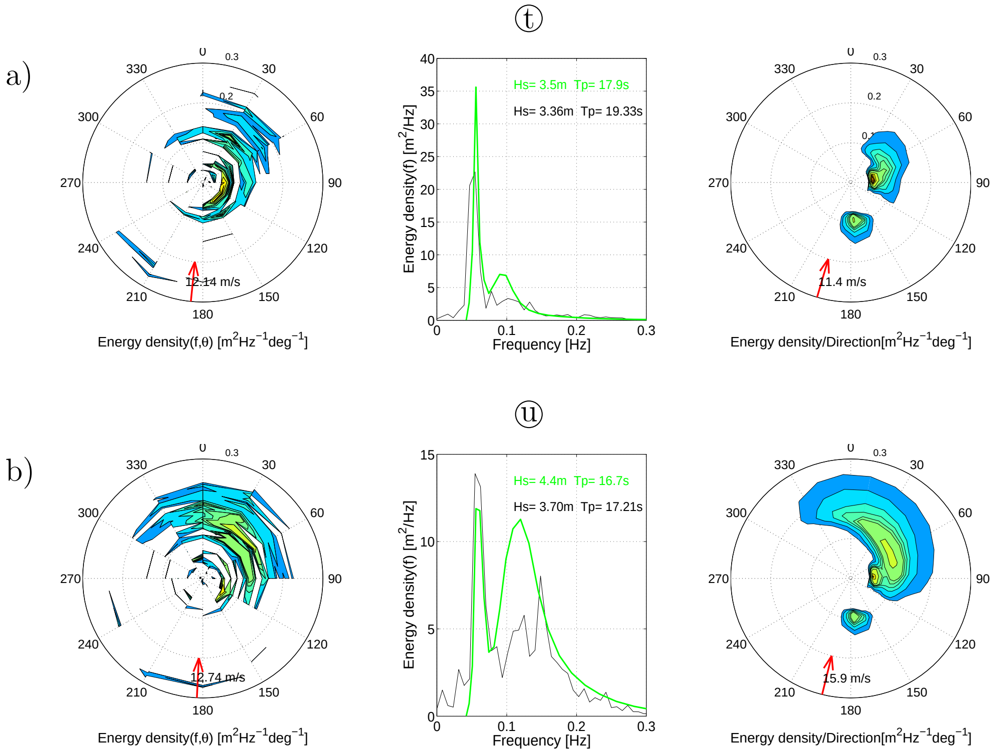

Figure 7.25: *Troll A: a) 18UTC 9. Feb. and b) 00UTC 10. Feb. 2000. Left: 2D spectrum(MIROS-radar) and measured wind. Middle: 1D spectra with corresponding H_s and T_p, MIROS-radar(black) and WAM(green). Right: 2D spectrum(WAM) and modelled wind(HIRLAM).*

highly mixed, best illustrated by the modelled 2D spectra. There is the N swell and a wind-sea turning from the SW to NW, see fig. 7.20h). And, looking closely one can see the first sign of the long period swell indicated by the small blue-colored dot coming from the WNW. However, the wind-sea is dominating and clearly more energetic in the measurements, focusing on the 1D spectrum.

ⓦ: At 12UTC the 9th, fig. 7.26b), the measured wind-sea is decreasing, while the corresponding simulated wind-sea is more or less the same as 6 hours earlier. The long period swell has propagated into the area, indicated by a much reduced peak around 0.05Hz in the 1D spectrum. Compared to the data obtained at the more northerly located oil rigs the energy travelling with the swell is now only fractional. Observe how the wind is going in the same directions as the swell. The simulated wind-sea is slightly more downshifted compared to the measurements, however less energetic.

ⓧ: 6 hours later, see fig. 7.26c), the measured 1D spectrum clearly separates three wave systems, also evident in the simulated 2D spectrum. There are still two swells and a turning wind-sea present. Recognize the fact that the most energetic peak of the simulated 1D spectrum is the sum of two wave systems, the N swell and the wind-sea.

Worth noticing is the behavior of the wind-sea observed in the time period spanned by fig. 7.26. While the model maintains a fairly steady peak and moderate decrease

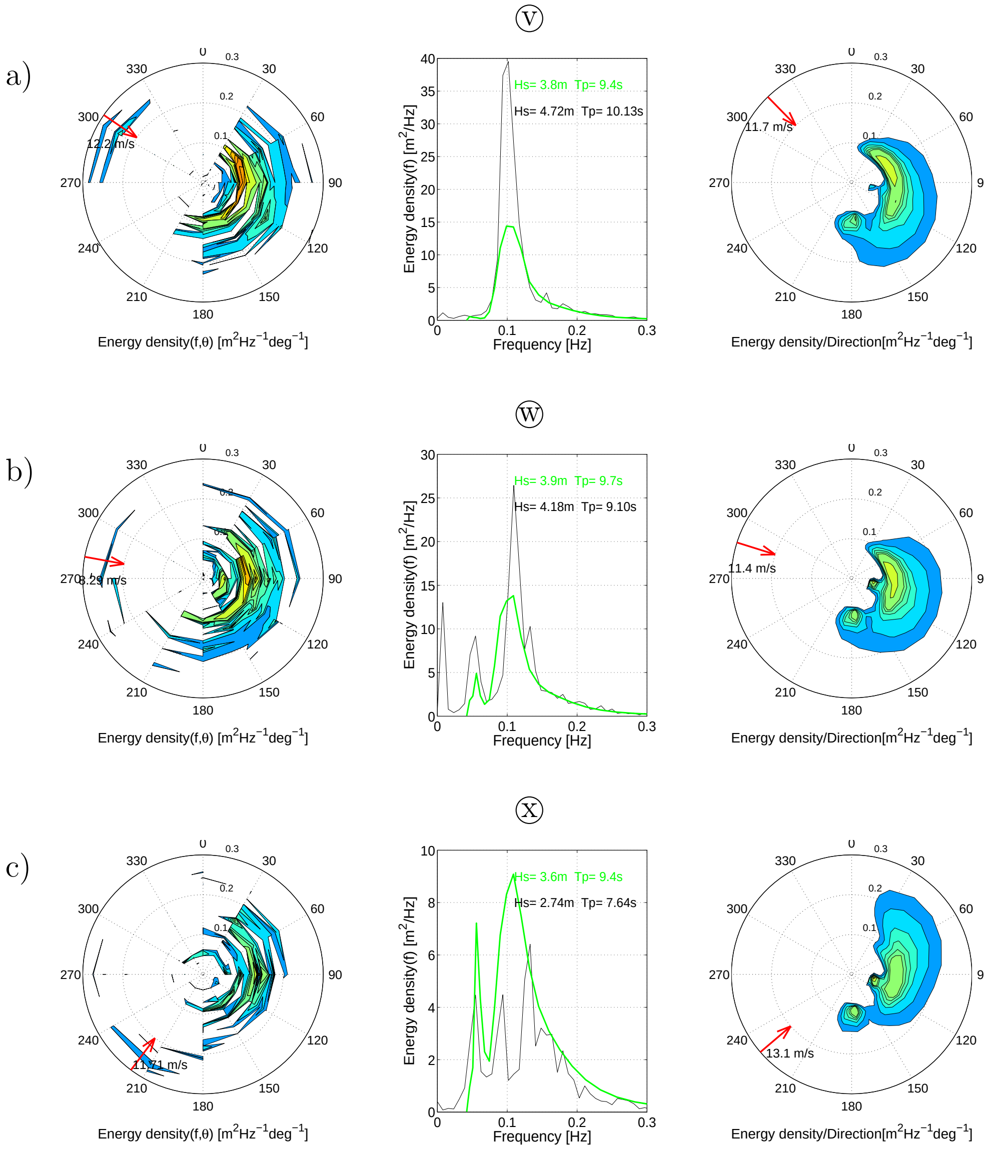

Figure 7.26: *Sleipner A: a) 06UTC, b) 12UTC and c) 18UTC 9. Feb. 2000. Left: 2D spectrum(MIROS-radar) and measured wind. Middle: 1D spectra with corresponding H_s and T_p, MIROS-radar(black) and WAM(green). Right: 2D spectrum(WAM) and modelled wind(HIRLAM).*

of energy, the measurements show a much more rapid reduction in energy and a peak going towards higher frequencies with time.

7.2.5 Saturation range

Fig. 7.18 are based on the same calculations made in the 2003-case, see section 7.1.5. However, the Troll A data are excluded.

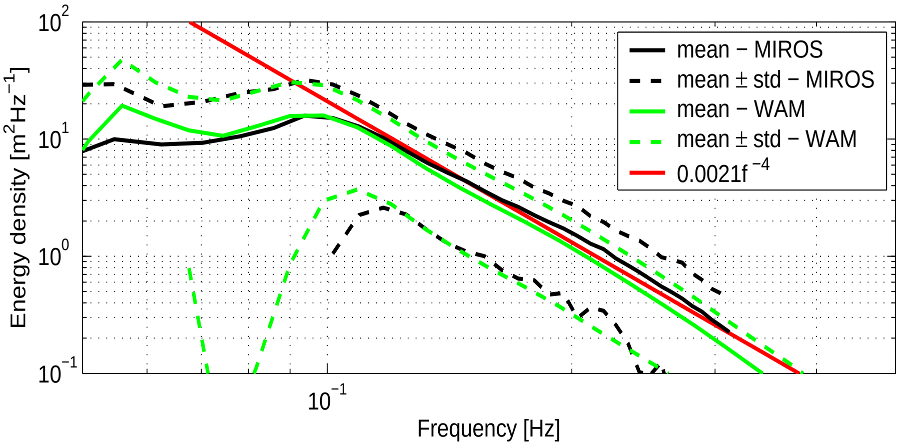

Figure 7.27: *The average simulated(WAM) and measured(MIROS) 1D spectra for Heidrun, Gullfaks C and Sleipner A for the period 8th-12th of February 2000. The* $0.0021^{-4}f$*-function is given as a reference measure.*

7.2.6 Discussion

Wind forcing the model

The 2000-case is poorly documented in regard to model simulations. All available time series are based on increasing prognostic wind fields. Statistically the quality of these winds will deteriorate with time and reduce the accuracy of the simulated wave data. However, as the prognostic performance of the HIRLAM-model will vary from time to time, sometimes being better than others, it is necessary to analyze each case independently. Like the 2003-case, the locally simulated U_{10}-winds are compared to corresponding measurements obtained at the four oil rigs, illustrated in fig. 7.20.

For the 2000-case, the wind evaluation is more complicated by the fact that the model results are only available every second time step, i.e. every sixth hour. In that way it is impossible to obtain a complete picture of the wind forcing the model locally. This shortcoming becomes apparent when studying the wind speed e.g. at Heidrun at 03UTC the 10th, see fig 7.20a). At this stage the simulated wind is not represented by the actual wind forcing the model, but by a linear interpolation deduced from the wind three hours prior and latter. The deviation between the simulated and measured wind speed is significant, however most likely not representative. Therefore, when studying the wave spectra -and parameters around this hour they can not be properly tested for wind inaccuracies caused by this deficiency in the data. One way of dealing with the problem is to evaluate the wind solely based on the scatter plots of fig. 7.20 and the statistics of table 7.5, which are deduced only from the hours the simulated winds are available.

In fact all wind speed correlations representing the 2000-case are improved compared to the 2003-case, with the exception of Sleipner A, see fig. 7.3, 7.4 and 7.20. The summary statistics of the two cases, see table 7.1 and 7.5, show that the quality of the simulated local winds are much the same in both cases. However, one point should be made. Focusing on the total wind speed statistics for the two cases, it is evident that the simulated winds of the 2003-case are stronger compared to the measurements than the 2000-case, with a total bias of 0.61 and -0.06 respectively.

As noted before, accurate wind at one grid point does not necessarily reflect the situation elsewhere within the model area. And, when the majority of wind fields forcing the wave model are based on prognosis, this uncertainty increases. Therefore, besides local comparisons, earlier statistical verifications of prognostic HIRLAM-model simulations should be taken into consideration. Komen et al. (1996) stated that simulations reaching 12-24 hour forecasts are often of the same quality or even better than the analysis, explained in section 7.1.6. Here, the +24h forecasts, corresponding to the 10th at 00UTC, cover most of the interesting part of the 2000-case. Besides, a long period swell of the dimension seen in the 2000-case, is depending on long lasting wind duration much prior to its actual arrival. This means slightly inaccurate local winds most likely will not change the simulated swell significantly. On the other hand, any wind-seas are more vulnerable to poorly simulated local winds. However, as stated above, the simulated winds seem satisfactory.

Wave parameters

The wave condition of the 2000-case is first and foremost unique for the presence of a long period swell propagating in from the WSW. Of the four independent radars, all indicate the peak period to be in the 21-23s range, depending on the position of observation, see fig. 7.21. This consistency in the radar measurements underlines their accuracy, that is, assuming MIROS's signal analysis is precise. However, compared to the measurements the simulated peaks are off by 3-4 seconds at Heidrun, Gullfaks C and Troll A, see fig 7.21b),d) and f). What may be the reason for this significant mismatch?

According to the dispersion relation, see eq. 2.8, the phase speed corresponding to a 22s wave period equals 34.3m/s in deep water and has a wavelength exceeding 750m. Only persevering strong winds are able to activate wave components of this magnitude. To put this into perspective, the PM-spectrum (Pierson and Moskowitz 1964), representing a fully developed wind-sea, see eq. 2.27, requires a 30m/s wind speed to generate a wave system of $T_p = 22s$. When applying a 30m/s wind speed and a 22s peak period to the JONSWAP-spectrum (Hasselmann et al. 1973) it is found that a 1600km fetch is needed. However, according to the manual wave forecasting diagram developed by Gröen and Dorrestein (1976) a fetch twice this distance is required, with a 72 hour duration. It should be noted that the PM-spectrum, JONSWAP-spectrum and the wave diagram are assuming stationary wind conditions. Even though these numbers are slightly speculative it leaves little doubt that a wave system with a 22s peak period demands winds of high speed and long durability working over a long stretch of water(fetch).

The above mentioned numbers are based on a wind-sea. Once the wave system no longer is forced by the wind and becomes, by definition, swell, the different wavelengths disperse according to eq. 2.8. The longer the wave system propagates without external forcing, the more spread out the wave components become, changing the appearance of the wave spectrum. Different parts of the spectrum will arrive at different times, giving the spectra a more narrow shape, illustrated in the 1D spectrum of fig. 7.22b). The longest and fastest wave components will arrive first, followed by the shorter ones. This is evident by the decreasing T_p seen in fig. 7.21 around 12UTC the 9th. This dispersive characteristic waves inherent implies that the peak period of a swell not necessarily correspond to that of the original wind-sea system. It might be slightly longer. However, the difference will be small. Consequently, the peak of the original wind-sea system of the 2000-case might have been smaller than indicated by the swell, but still long enough to demand more or less the same conditions as discussed above.

Focusing on fig. 7.19, there is no evidence of the wind reaching 30m/s. When taking the required duration into account, discussed above, the wind fields prior to the arrival of the long period swell seem weak. Since fig. 7.19 only illustrates the condition at 12UTC, the winds must have been stronger in between these hours. Most likely the wave system was absorbing energy irregularly over a much longer distance than required in stationary conditions. Fig. 7.19 shows how the North Atlantic was dominated by SW winds throughout the period. A distant generated wave system may have been kept energetic and growing over a vast stretch of open ocean.

The WAM-model run at met.no is limited to a geographical area, illustrated by fig. 7.28, and all boundaries are set to zero. A closed basin with no energy exchanges across the boundaries will suffer from misrepresentations in the model simulations. Any distant generated swells propagating into the area of operation are going to be absent in the simulations, while a wind-sea generated across the boundaries will be treated as a fetch-limited case, restricted by the boundary, giving a reduction in energy and a reduced downshift of the wave spectrum. In most cases only the area adjacent to the boundaries suffer from this kind of model implementation. However, in conditions of steady wind directions, any misrepresentations made at the boundaries may be kept significant and advected, in this case, all the way to the coast of Norway. Therefore, there may be reason to believe this was the cause for the 3-4s offset found in the simulated T_p during the 2000-case. A possible swell track is illustrated in fig. 7.28, which equals a distance of about 5000km. Then again, inaccurate simulated winds may have played an equally important part in the deviating results.

Of the four oil rigs, Sleipner A is less dominated by the WSW swell than the three other oil rigs. Only during two shorter periods, around 18UTC the 10th, the swell is evident in the T_p-measurements, see fig. 7.21. The remainder of the swell reaching Sleipner A is affected by the position of the oil rig. By being in the shadow of Great

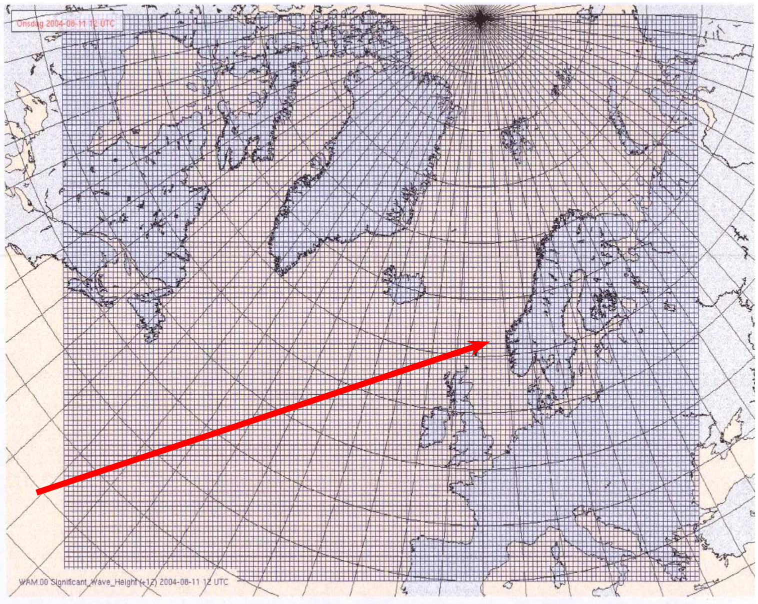

Figure 7.28: *The possible propagation track of the long period swell observed the 9th of Feb. 2000. The original wave system may have been generated outside the geographical area of the WAM-model boundaries as indicated by the red arrow.*

Britain, energy is lost as the swell refracts around land. In addition, Sleipner A finds itself in more shallow water, see table 6.1. In that way the extremely long wavelengths will interact with the bottom, also loosing energy be friction.

The H_s-measurements obtained at Troll A, see fig. 7.21e), are in the first part of the time series clearly affected by some sort of malfunction. Such behavior is often related to periods of weak winds. This is seen at Gullfaks C at 10UTC the 9th where the spike in the H_s-measurement coincides with the calm wind at the time, see fig. 7.6c) and fig. 7.4c). Because the radar relies on the presence of capillary waves at the surface to obtain a sufficient reflected signal, a minimum of wind is required, often said to be around 3m/s. However, the data of Troll A show sufficient wind to generate capillary waves within the period of inaccurate H_s measurements, meaning the malfunction must lie elsewhere. This is confirmed by the seemingly unaffected T_p at Troll A, see fig. 7.21f). A possible explanation may be found in the signal processing unit of the radar. However, this will only be speculations. Here, it is only acknowledged that the Troll A H_s measurements are inaccurate and therefore not taken into consideration in the total statistics of table 7.5 and 7.6.

Approaching/receding waves relative to radar heading

For the 2000-case there are few signs of the radar performance being affected by the direction of waves relative to the 180 degrees sector of the radar. This is based on the very much similar results found in $H_{s,eq}$ for the two sectors given in table 7.6.

The difference in the radar's ability to measure receding and approaching waves is marginal and does not indicate a significant loss of energy when representing integrated parameters such as H_s.

However, the 2D spectra offer some vague proof that the radar is vulnerable in situations of opposing wave systems. This becomes evident at Heidrun, illustrated in fig. 7.23, where the N swell is not represented in the measurements. Interestingly, around the same time the 2D spectrum obtained at Gullfaks C, see fig. 7.24a), indicates the N swell to be present. This again affects the representation of the SW wind-sea, showing a gap in the 2D spectrum at those frequencies corresponding to the N swell, see fig. 7.24a). However, the energy content of both the N swell and SW wind-sea are so small compared to the WSW swell, that the total energy will not be significantly affected.

The different 2D-representations of the N swell at Heidrun and Gullfaks C may be explained by the fact that the opposing wind-sea is stronger relative to swell at Heidrun and viceversa at Gullfaks C. This offers some proof that the radar always represents that of the two directional-frequency bin of 180 degrees ambiguity having the most energy.

Saturation range

The 2000-case is more dominated by periods of pure swell conditions than the 2003-case. This affects the average simulated and measured spectrum illustrated in fig. 7.27. Because of the dispersive characteristic of ocean waves, a distant swell is not considered fully developed. Compared to the 2003-case, the average spectra have a slightly less energetic tail, which is to be expected. This is evident by the different amount of energy found in the simulated and measured tail relative to the f^{-4} power law(red line) given in each case.

The increased irregularity and standard deviation of the mean spectra obtained from the 2000-case are caused by the reduced numbers of available spectra. However, with some goodwill the measurements can be said to have a tail slope closer to the f^{-4} power law in this case compared to the 2003-case.

Once again the average simulated tail is found less energetic compared to the measured tail, which may indicate the need for an improved and more flexible parametrization of the saturation range of the simulated spectrum.

Wind-sea growth in the presence of swell going in/across the direction of the wind

During the 9th and 10th of Feb. 2000 the wave conditions at the four oil rigs were dominated by energetic swell activity and a building wind-sea. The combined wave systems are illustrated in the spectra of fig. 7.23-7.26. Unlike the 2003-case, this time the wind shifted between going in and across the direction of the dominating long period swell. According to the works of Donelan et al. (1993),Drennan et al. (1999) and Kudryavtsev and Makin (2004) the drag coefficient is reduced in these types of conditions compared to conditions of wind opposing swell. Therefore, it may be expected that the measured wind-sea is less evolved relative to the simulated wind-sea in the 2000-case compared to the 2003-case.

Non of the two analyzed cases of this thesis may be considered idealized. Winds are not stationary and the developing wind-seas are not fetch-limited. To further complicate the matter, an additional swell is present during the 2000-case. This N swell propagates on average in the opposite direction of the wind. As debated above, this may have the effect of increasing the wind-sea growth. However, the energy content of the N swell is significantly smaller than the WSW swell and only well defined in the simulated 2D spectra, illustrated in fig. 7.23-7.26. The measured 2D spectra are inconclusive and do not give a clear representation of the N swell. Therefore, it is assumed that the effect of the N swell on the growth of the wind-sea is minor compared to the effect imposed by the WSW swell.

Out of the four oil rigs, the results obtained at Heidrun are the least encouraging, see fig. 7.23a) and b). Here, the measured and simulated wind-sea highly resemble the findings made in the 2003-case. Again the measured wind-sea clearly exceeds the development of the simulated wind-sea, which does not correspond well with the expected result. However, this behavior may have been influenced by poorly simulated winds. Large fluctuations in the wind field at Heidrun prior to this event may have been improperly resolved by the HIRLAM-20, see fig. 7.4. In addition, the northern displacement of the radar compared to the corresponding grid point, see fig. 6.1, will enable any S wind-sea to evolve over a longer distance compared to the simulations, assuming an uniform wind within this area.

In contrast, the spectra obtained at the three southernmost oil rigs, see fig. 7.24-7.26, indicate a change in the measured and simulated wind-sea relation compared to the 2003-case. Focusing on Gullfaks C, see fig. 7.24, the peak of the simulated and measured wind-sea almost coincide. At Troll A and Sleipner A, see fig. 7.25b), 7.26b) and c), the energy carried by the measured wind-sea is reduced compared to the simulation, also affecting the deviation in H_s. In addition, the peak of the measured wind-sea is less downshifted. Both effects indicate a reduction in the measured wind-sea growth compared to conditions of wind-sea opposing swell, seen in the 2003-case. However, as mentioned above, statistically the simulated wind speeds of the 2000-case are weaker compared to the 2003-case, which may have contributed to fortify this behavior of the wind-sea.

All in all, the different behavior of the measured spectra relative to the corresponding simulations of the 2000-case and 2003-case may be the result of a swell-dependent drag coefficient, as this effect is not accounted for in the S_{in} source-function of the WAM-model. However, as debated in section 7.1.6, there are considerable uncertainties connected to these data, where the quality of the wind forcing the model always will be a big questionmark.

Chapter 8

Conclusions and Future thoughts

In this study data obtained by the MIROS microwave wave-radar have been compared to the third generation wave model WAM(cycle-4), driven by HIRLAM-20 10m winds, run operationally at met.no. Four radars, installed on the Statoil rigs; Heidrun, Gullfaks C, Troll A and Sleipner A, located in the North -and Norwegian Sea were chosen for the study. The analyzed data were collected during two severe swell events; 10-16th of December 2003 and 8-12th of February 2000. First case was related to two adjacent deep low pressure systems producing significant wave heights above 12m, while the second case was dominated by a WSW swell with a peak period reaching 23s.

The focus of the thesis have been made on the performance of both model and radar in situations of swell. Possible shortcomings are addressed and discussed. In addition, the growth properties of wind-sea are examined in the presence of swell. It should be noted that the amount of data analyzed are sparse and do not offer a statistical valid evaluation. Therefore, the findings of this work will primarily apply to the particular case itself, but may also offer a support to developing theories. The following results and future thoughts were made;

Model performance: Wave parameters

Previous studies have shown the WAM-model to underestimate key parameters such as H_s and T_p (Janssen et al. 1997). The overall statistics based on the 2003-case shows similar results for H_s. In spite of having on average too strong winds forcing the model locally, the simulated H_s was on three out of four positions too small. All in all the model had a bias equal to -0.23cm. A possible explanation may be found in the saturation range of the simulated spectrum. On average the energy content of the simulated tail was found low in both cases, which may indicate an improvement potential for the saturation range of the model. The T_p-statistics was generally of high quality.

The WAM-model at met.no is implemented as a 'closed basin'. In general, the simulations near the boundaries are mostly affected by this kind of model set-up. However, when powerful wave systems are generated outside and across the boundaries and kept energetic by stable winds within the geographical area of the model, inaccurate simulations at the boundaries may be advected, in this case, all the way to the Norwegian coast. When these misrepresentations concern powerful swells with peak periods above 20 seconds, this becomes of special importance to e.g. offshore constructions. Large oil rigs have maximum response around these periods, making accurate forecasting important to obtain a safe operation. There are two simple ways of improving the simulations. First, by expanding the modelled area, the model is able to 'see' more of the wind field influencing the wave conditions in Norwegian waters. However, this will only partially solve the problem. Distant swells may still propagate unnoticed across the boundaries. A more permanent solution will be to nest the model into a global model, in that way improving the boundaries.

Approaching/receding waves relative to radar-heading

The MIROS-radar is constructed to scan 180 degrees of open ocean. Its ability to detect approaching as well as receding waves offers an indirect scan covering 360 degrees. However, the signal analysis is restricted to represent only one out of two directional-frequency-bins of 180 degrees ambiguity at the same time.

First, statistically there were found no indications in these data of the MIROS-radar measuring approaching or receding waves more precise than the other. In that way, the radar is thought to be insensitive to its heading and may be placed in an arbitrary direction without the possibility of reducing the quality of integrated parameters, such as H_s.

Second, it should be noted that none of the two cases discussed here had exactly opposing wave systems with coinciding peak frequencies, a situation where the MIROS-radar seems most likely to perform at its worst. In this context, it may be argued that the position of the radar, which in this case was close to the Norwegian coast, rarely make them exposed to these conditions, as powerful wave systems seldom are coming from the coast. However, the radars installed on Gullfaks C, Troll A and Sleipner A can be thought to be vulnerable in an N-S direction, where a polar low producing a N swell may be accompanied by a S swell generated by a more southern situated low pressure system. Therefore, in ocean areas more exposed to swell activity from all directions, the radar may perform less satisfactory.

Even though the 1D spectrum or H_s did not show signs of being significantly affected in theses data, the appearance of the 2D spectra were somewhat deteriorated compared to the model. All in all, it may be concluded that the radar is insensitive to its heading, but may be vulnerable to its positioning.

Wind-sea growth in the presence of swell

A number of studies have had the purpose of finding those factors affecting the drag coefficient at the ocean surface. So far, the dependence of C_D on wave age, c_p/u_*, have been established in conditions of pure wind sea(Donelan et al. (1990); Smith et al. (1992); Donelan et al. (1992)). However, in the open ocean, where most wave systems are close to being fully developed, the variation in wave age is small and becomes of less importance. Thus, swell has been proposed as a possible contributing factor to altering the growth rate of wind-sea in mixed wave conditions. In this context, the relative direction between wind and swell is crucial (Donelan et al. 1993; Drennan et al. 1999; Kudryavtsev and Makin 2004).

Of the two cases analyzed in this study, the 2003-case had wind opposing swell, while the 2000-case had wind going with and across the direction of the dominating swell. As the model parametrization does not account for possible effects of swell, the evolution of wind-sea is unchanged whether a swell is approaching or receding the wind. Therefore, the relative behavior between the measured and simulated spectra may be used to search for effects of swell.

The results of this study were somewhat inconclusive, but intriguing nevertheless. In conditions of wind opposing swell the peak of the measured wind-sea was slightly more shifted towards lower frequencies compared to conditions of wind going with or across the direction of swell. This behavior corresponds to the results obtained by Donelan et al. (1993); Drennan et al. (1999) and Kudryavtsev and Makin (2004), which concluded the drag coefficient to increase in conditions of opposing swells. However, integrated parameters, like H_s, showed no signs of being significantly affected. Therefore, based on these data, it may be concluded that the effect of swell on wind-sea growth primarily affects the appearance of the wave spectrum.

A critical question should be raised concerning the method used in this study. There are considerable uncertainty connected to these type of simulations when searching for effects of this small magnitude. First and foremost, accurate wind fields forcing the model are crucial, but never easy to monitor. This is why similar work in the future should follow the example of Ardhuin (Sub), where only special cases with close to stationary wind conditions, clean single swell and clearly defined fetches are chosen. And, a 50km resolution model is probably going to be too coarse. Still, this type of approach will most likely not be accurate enough to calculate the magnitude of the effect.

These days several experiments are carried through in well supervised laboratories, where conditions can be made idealized. However, question arises whether small-scale experiments are representative for the large-scale open ocean or not. Probably the best way of answering this problem is obtained through extensive stress measurements accompanied by the 2D wave spectrum. Only then the effect may be fully understood.

Appendix A

Appendix

A.0.7 Statistics

Correlation, corr

$$corr(X,Y) = \frac{\sum_{i=1}^{n}(X_i - \bar{X})(Y_i - \bar{Y})}{\sqrt{\left[\sum_{i=1}^{n}(X_i - \bar{X})^2\right]\left[\sum_{i=1}^{n}(Y_i - \bar{Y})^2\right]}} \tag{A.1}$$

Bias

$$bias(meanerror) = \frac{\sum_{i=1}^{N}(X_i - Y_i)}{N} \tag{A.2}$$

Root mean square error, rms

$$rms = \sqrt{\frac{\sum_{i=1}^{N}(X_i - Y_i)^2}{N}} \tag{A.3}$$

Scatter Index, SI

$$SI = \frac{rms}{\bar{X}} \tag{A.4}$$

rms error normalized by the mean observed value of the reference quantity.

References

Ardhuin, F. (Sub.). Swell and slanting fetch effects on wind wave growth.

Ardhuin, F., W. O'Reilly, T. Herbes, and P. Jessen (2003). Swell transformation across the continental shelf. part 1: Attenuation and directional broadening. *J. Phys. Oceanogr. 33*, 1940–1953.

Charnock, H. (1955). Wind stress over water surface. *Quart. J. Roy. Meteorl. Soc. 81*, 639–640.

Dobsen, M., S. Smith, and R. Anderson (1994). Measuring the relationship between wind stress and sea state in the open ocean in the presence of swell. *Atmos.-Ocean 32*, 237–256.

Donelan, M., F. Dobsen, S. Smith, and R. Anderson (1993). On the dependence of sea surface roughness on wave development. *J. Phys. Oceanogr. 23*, 2143–2149.

Donelan, M., W. Drennan, and K. Katsaros (1997). The air-sea momentum flux in conditions of wind sea and swell. *J. Phys. Oceanogr. 27*, 2087–2099.

Donelan, M. A. (1987). The effect of swell on the growth of wind waves. *Johns Hopkins APL Tech. Digest 8*, 18–23.

Donelan, M. A., B. LeMéhauté, and D. Hanes (1990). *Air-sea interaction . The sea, Vol. 9. Ocean engeneering science.* John Wiley and Sons. ISBN-0471528560.

Donelan, M. A., M. Skafel, H. Graber, P. Liu, D. Schwab, and s. Venkatesh (1992). On the growth rate of wind-generated waves. *Atmos.-Ocean 30*, 457–478.

Drennan, W., H. Graber, and M. Donelan (1999). Evicence for the effects of swell and unsteady winds on marine wind stress. *J. Phys. Oceanogr. 29*, 1853–1864.

Forristall, G. (1981). Measurements of saturated range in ocean wave spectra. *J. Geophys. Res 86*, 8075–8089.

Geernaert, G. and W. Plant (1990). *Surface waves and fluxes.* Kluwer. ISBN-0792308093.

Gelci, R., H. Cazalé, and J. Vassal (1957). Prévison de la houle. La méthode des densités spectroangulaires (Prediction of waves. The method of frequency-directional spactral densities). *Bull. Infor. Comité Central Oceanogr. d'Etude Côtes 9*, 416–435.

Gröen, P. and R. Dorrestein (1976). Zeegolven. *Opstellen op Oceanografische en Maritiem Meteorologisch Gebied 11*, 124 pp.

Grønlie, Ø. (1996). *Miros Wave radar Mk2 - Principles of operation.* Miros A/S.

Grønlie, Ø. (1999). *Miros wave radar - Theory of wave spectrum measurements.* Miros A/S.

Hanson, J. and O. Phillips (1999). Wind sea growth and dissipation in the open ocean. *J. Phys. Oceanogr. 29*, 1633–1648.

Hasselmann, K. (1962). On the nonlinear energy transfer in a gravity wave spectrum. part 1. general theory. *J. Fluid Mech. 12*, 481–500.

Hasselmann, K., T. Barnett, E. Bouws, H. Carlson, D. Cartwright, K. Enke, J. Ewing, H. Gienapp, D. Hasselmann, P. Kruseman, P. Meerburg, A. Muller, D. Olbers, K. Richter, W. Sell, and H. Walden (1973). Measurements of wind-wave growth and swell decay during the joint north sea wave project (JONSWAP). *Dtsch. Hydrogr. Suppl. A 8(10)*, 95p.

Hasselmann, K., D. Ross, P. Muller, and W. Sell (1976). A parametric wave prediction model. *J. Phys. Oceanogr. 6*, 200–228.

Hasselmann, S. and K. Hasselmann (1985). Computations and parameterization of the nonlinear energy transfer in a gravity-wave spectrum. part 1: A new method for efficient computation of the exact nonlinear transfer integral. *J. Phys. Oceanogr. 15*, 1369–1377.

Hasselmann, S., K. Hasselmann, J. Allender, and T. Barnett (1985). Computations and parameterization of the nonlinear energy transfer in a gravity-wave spectrum. part 2: Parameterization of the nonlinear energy transfer for application in wave models. *J. Phys. Oceanogr. 15*, 1378–1391.

Janssen, P. (1991). Quasi-linear theory of wind wave generation applied to wave forecasting. *J. Phys. Oceanogr. 21*, 1631–1642.

Janssen, P., B. Hansen, and J. Bidlot (1997). Verification of the ecmwf wave forcasting system against bouy and altimeter data. *Weather and Forcasting 12*, 763–784.

Kitaigorodski, S. (1983). On the theory of the equillibrium range in the spectrum of wind-generated gravity waves. *J. Phys. Oceanogr. 13*, 816–827.

Komen, G., L. Cavaleri, M. Donelan, K. Hasselmann, S. Hasselmann, and P. Janssen (1996). *Dynamics and Modelling of Ocean Waves.* Cambridge, University press. ISBN-0-521-57781-0.

Kudryavtsev, V. and V. Makin (2004). Impact of swell on the marine atmospheric boundary layer. *J. Phys. Oceanogr. 34*, 934–949.

Large, W. and S. Pond (1981). Open ocean momentum flux measurements in moderat to strong winds. *J. Phys. Oceanogr. 11*, 324–336.

Liu, P. (1989). On the slope of the equillibrium range in the frequency spectrum of wind waves. *J. Geoph. Res. 94*, 5017–5023.

Massel, S. (1996). *Ocean surface waves: Their physics and prediction.* Worl scientific. ISBN 9810221096.

Miles, J. W. (1957). On the generation of surface waves by shear flow. *J. Fluid Mech. 3*, 185–204.

Phillips, O. (1957). On the generation of waves by turbulent wind. *J. Fluid Mech. 2*, 417–445.

Phillips, O. (1958). The equillibrium range in the spectrum of wind-generated water waves. *J. Fluid Mech. 4*, 426–434.

Phillips, O. (1985). Spectral and statistical properties of the equillibrium range in wind-generated gravity waves. *J. Fluid Mech. 156*, 505–531.

Pierson, W. and L. Moskowitz (1964). A proposed spectral form for fully developed wind-seas based on the similarity theory of s.a. kitaigorodskii. *J. Geophys. Res. 64(24)*, 5181–5190.

Shearman, E. (1983). Radio science and oceanography. *Radio science 18(3)*, 299–320.

Smith, S. (1980). Wind stress and heat flux over the ocean in gale force winds. *J. Phys. Oceanogr. 10*, 709–726.

Smith, S., R. Anderson, W. Oost, C. Kraan, and N. M. and (1992). Sea surface wind stress and drag coefficient: The hexos results. *Bound.-Layer Meteor. 60*, 109–142.

Snyder, R., F. Dobsen, J. Elliot, and R. Long (1981). Array measurements of atmospheric pressure fluctuations above surface gravity waves. *J. Fluid Mech. 102*, 1–59.

Snyder, R., W. Thacker, K. Hasselmann, S. Hasselmann, and G. Barzel (1993). Implementation of an efficient scheme for calculating nonlinear transfer from wave-wave interactions. *J. Geophys. Res. 98*, 14507–14525.

Taylor, P. and M. Yelland (1996). Wind stress measurements from the open ocean. *J. Phys. Oceanogr. 26*, 541–558.

The SWAMP-group (1985). *Ocean wave modeling.* Plenum Press, New York. 256pp.

Toba, Y. (1973). Local balance in the air-sea boundary process,3. on the spectrum of wind waves. *J. Oceanogr. Soc., Japan 29*, 209–220.

Vignes, O. (1998). Operational hirlam at met.no. http://hirlam.knmi.nl/open/publications/NewsLetters/43/opernewsl.pdf.

WMO (1998). *Guide to Wave Analysis and Forcasting.* WMO. ISBN 0-12-283520-4.